# DENSITY FUNCTIONAL THEORY STUDY OF CUPRATE AND TRANSITIONAL METAL COMPOUNDS, AND EXACT CONSTRAINTS AND APPROPRIATE NORMS IN MACHINE LEARNED EXCHANGE-CORRELATION FUNCTIONALS

AN ABSTRACT

SUBMITTED ON THE 29th OF APRIL 2022

TO THE DEPARTMENT OF PHYSICS
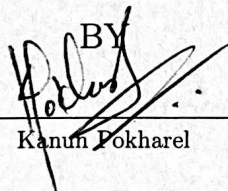
IN PARTIAL FULFILLMENT OF THE REQUIREMENTS

OF THE SCHOOL OF SCIENCE AND ENGINEERING

OF TULANE UNIVERSITY

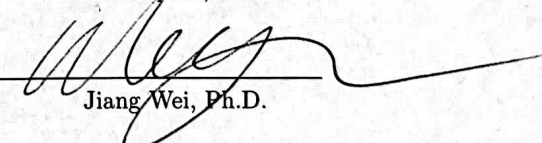FOR THE DEGREE

OF

DOCTOR OF PHILOSOPHY

BY

_____
Kanun Pokharel

APPROVED: _____
Jianwei Sun, Ph.D.(Advisor)

_____
Lev Kaplan, Ph.D.

_____
Jiang Wei, Ph.D.

## Abstract

Density functional theory (DFT) has become the most widely used computational approach for solving problems in chemistry, materials science, and condensed matter physics because of its balanced accuracy and efficiency. In principle, DFT is exact for the ground state energy and electron density, while its exchange-correlation (XC) component must be approximated. There has been extensive research on improving approximations to the XC energy and the resulting approximations are roughly categorized into a hierarchy of increasing complexity and accuracy. Most of these approximations are based on mathematical constraints satisfaction philosophy while others follow empirical pathway of fitting functionals to certain data set of interest. More recently, machine learning (ML) has emerged out as an active areas of research for functional design. This PhD dissertation focuses on two aspects of DFT. One is to test recently developed density functionals for systems that are traditionally difficult for DFT, while the other is to develop density functionals using machine learning (ML) techniques in combination with the exact constraint considerations.

For the first two projects, the properties of two difficult systems from DFT's perspective, are studied. Until recently, DFT had been failing to capture the properties of these systems correctly. With Strongly constrained and appropriately normed SCAN functional's success on them, accessing the performances of other density functional approximations was essential to observe how different functionals behaved on these systems. In this regard, for the first project, we study the crystal, electronic, and magnetic structures of high temperature superconductor, lanthanum copper oxide $La_{2-x}Sr_xCuO_4$ (LSCO) for $x = 0.0$ and $x = 0.25$ , employing 13 density functional approximations, representing the local, semi-local, and hybrid exchange-correlation approximations within the Perdew–Schmidt hierarchy. We see that the meta-generalized gradient approximation (meta-GGA) class of functionals is found to perform well in capturing the key properties of LSCO, a prototypical high-temperature cuprate superconductor. In contrast, the local-spin-density approximation, GGA, and the hybrid density functional fail to capture the metal-insulator transition under doping.

The second project is an extension to the first work where we study the electronic properties of $3d$ transition-metal monoxides (MnO, FeO, CoO, and NiO) employing 11 density functional approximations. Similar to cuprate, we observe that the meta-GGA class of functionals again perform better than other semilocal density functionals (including LSDA and GGA) by opening a band gap without an on-site inter-electronic interaction U.

For the final project, ML techniques are used to design new density functional. Since SCAN is found to exhibit greater accuracy for a variety of systems, the new ML functional is built upon SCAN. In addition,

the philosophy of exact constraints and appropriate norms compatibility with ML for functional design are explored. ML techniques have received growing attention as an alternative strategy for developing general-purpose density functional approximations, augmenting the historically successful approach of human designed functionals derived to obey mathematical constraints known for the exact exchange-correlation functional. More recently efforts have been made to reconcile the two techniques, integrating machine learning and exact-constraint satisfaction. We continue this integrated approach, designing a deep neural network that exploits the exact constraint and appropriate norm philosophy to deorbitalize the strongly constrained and appropriately normed SCAN functional. The deep neural network is trained to replicate the SCAN functional from only electron density and local derivative information, avoiding use of the orbital dependent kinetic energy density. The performance and transferability of the machine learned functional are shown for molecular and periodic systems.

# DENSITY FUNCTIONAL THEORY STUDY OF CUPRATE AND TRANSITIONAL METAL COMPOUNDS, AND EXACT CONSTRAINTS AND APPROPRIATE NORMS IN MACHINE LEARNED EXCHANGE-CORRELATION FUNCTIONALS

A DISSERTATION

SUBMITTED ON THE 29th OF APRIL 2022

TO THE DEPARTMENT OF PHYSICS

IN PARTIAL FULFILLMENT OF THE REQUIREMENTS

OF THE SCHOOL OF SCIENCE AND ENGINEERING

OF TULANE UNIVERSITY

FOR THE DEGREE

OF

DOCTOR OF PHILOSOPHY

BY

_____
Kamal Pokharel

APPROVED: _____
Jianwei Sun, Ph.D.(Advisor)

_____
Lev Kaplan, Ph.D.

_____
Jiang Wei, Ph.D.

# Acknowledgement

I would like to take time to thank everyone that helped me in my graduate study journey. To begin with, I have my deepest gratitude for my family for their continuous support. To my dad and mom, back home in Nepal, my brother in-law and sister here in the US, I am thankful for all your support. In the end, most importantly, my wife, Kopila Dhakal, for her patience and continuous motivation to keep me calm at tough times, I cannot thank you enough.

I would like to extend my gratitude to my dissertation committee Prof. Lev Kaplan and Prof. Jiang Wei for their valuable comments and suggestions. I would also like to thank my MatComp group members Dr. James W. Furness, Dr. Jinliang Ning, Dr. Ruiqi Zhang, Manish Kothakonda, Jamin Kidd, Lin Hou and Henry Fitzhugh for your direct or indirect support. You have always been there for help whenever I was in need of it.

Finally, I would also like to express my deepest gratitude to my advisor Prof. Jianwei Sun for his invaluable advice, continuous support, and guidance. His continuous encouragement to be better my work, constructive and insightful suggestions to the concepts, and more importantly the freedom he provided to work independently, is what I cherished the most during my graduate life. You are a very supportive advisor. Your super-friendly nature always allowed me to reach out to you easily and express my concerns without hesitations.

# Contents

# List of Figures

# List of Tables

# Introduction

Scientific work in today's world has predominantly been dominated by computers especially when it comes to analytically unsolved problems. The field of quantum chemistry is one of such fields where calculations are heavily dependent on computer simulations where energies, charge distribution, dipole, multipoles, and many other instances are calculated. Early works on dealing with the complex and analytically not accessible many-body Schrödinger equation were performed by Hartree and Fock, who derived a set of self-consistent, wave-function based equations that allowed an iterative calculation of energy- and other desired parameters[19, 20]. It was a good attempt but was flawed in terms of high computation time and cost when large systems were investigated because many body wave-functions had 3N degrees of freedom. Foundation to lowering the computation cost was laid by Hohenberg and Kohn in 1964 when they showed that the electron density, a variable only dependent on 3 spatial variables rather than 3N, in principle, contained all the information about the ground state properties of a system[21]. Kohn and Sham in 1965[22], came up with a set of self-consistent, iteratively solvable equations which was finally able to solve the complex many-body systems. It is based on the fact that electron density is much less complex quantity than wave-function and computation time for DFT calculations are drastically reduced. At present, DFT is widely used in variety of quantum mechanical problems from quantum chemistry, to material science, and to condensed matter physics. One of the most important quantities of DFT is the exchange correlation density functional that arises from the Kohn-Sham approach and needs to be approximated.

The thesis begins by establishing necessary theoretical background of DFT in Chapter 1 which is extended to Chapter 2 where construction, performance and limitations of various meta-GGAs are reported.

Chapter 3 focuses on analyzing the performance of various density functional approximations on high temperature superconductors (cuprate). Here the crystal, electronic, and magnetic properties of cuprate are studied. Chapter 4 is an extension to Chapter 3 where where we study the electronic properties of $3d$ transition-metal monoxides (MnO, FeO, CoO, and NiO) employing 11 density functional approximations.

Finally, Chapter 5 focuses on exploring the compatibility of philosophy of exact constraints and appropriate norms with Machine learning (ML) for functional design. Necessary theoretical background about ML is established before diving into constructing ML density functionals.

# Chapter 1

# Theoretical foundation

## 1.1 The Schrӧdinger equation

The behavior of atoms and electrons is completely described by non-relativistic Schrӧdinger equation:[23]

$$\hat{H}\Psi(\mathbf{r}_1, \mathbf{r}_2, ...., \mathbf{r}_N) = E\Psi(\mathbf{r}_1, \mathbf{r}_2, ......\mathbf{r}_N) \tag{1.1}$$

If we consider the interactions within a system of atoms then the Hamiltonian takes the following form:

$$\hat{H} = -\frac{1}{2}\sum_i^N \nabla_i^2 - \frac{1}{2m_A}\sum_A^M \nabla_A^2 - \sum_i^N\sum_A^M \frac{Z_A}{r_{iA}} + \sum_i^N\sum_{j>i}^N \frac{1}{r_{ij}} + \sum_i^M\sum_{B>A}^M \frac{Z_A Z_B}{R_{AB}} \tag{1.2}$$

where A,B represent the nuclei and i,j the electrons. This equation is complicated and can be simplified using the Born-Oppenheimer approximation[24]. The nuclei are assumed to move very slowly compared to electrons as they are relatively heavier. Thus this approximation allows the nuclear kinetic energy to be neglected and the Hamiltonian will only have dependence on the position of the nuclei. The wave-function in time independent schrodinger equation (TISE) can now to be separated into the electronic and nuclear components.

$$\Psi(\{r_i\}; \{R_A\})\Phi(\{R_A\}) \tag{1.3}$$

The Hamiltonian now will only be solved for a set of electrons around a set of nuclei and has following form

$$\hat{H}_{elec} = -\frac{1}{2}\sum_i^N \nabla_i^2 - \sum_i^N\sum_A^M \frac{Z_A}{r_{iA}} + \sum_i^N\sum_{j>i}^N \frac{1}{r_{ij}} \tag{1.4}$$

We are concerned in solving this TISE with the Hamiltonian expressed above but the solution is difficult and is only possible in simpler system like hydrogen atom. Solving larger system requires approximate computation methods, such as DFT.

## 1.2 Hartree-Fock approximation

One of the ways of approximately solving the TISE is using variational principle which best approximates the ground state wave-function that produces the lowest energy when acted upon the above Hamiltonian. Mathematically,

$$E_{ground} = \langle \psi_0 | \hat{H} | \psi_0 \rangle \leq \langle \psi | \hat{H} | \psi \rangle \tag{1.5}$$

In equation 1.4, the first two terms correspond to sum of single-particle operators while the electron-electron interaction term is a pair interaction. It is a many-body problem but it uses an approach of single-particle picture, i.e. we assume that the electrons occupy different orbitals and they make up the wave-function. Electron is assumed to feel the presence of other electron indirectly situated at other orbitals. One way of building the wave-function is to form a direct product of the orbitals as follows

$$\Phi(\mathbf{x}_1, \mathbf{x}_2.....\mathbf{x}_N) = \phi_1(\mathbf{x}_1)\phi_2(\mathbf{x}_2)...\phi_N(\mathbf{x}_N) \tag{1.6}$$

This is called Hartree-product. This approach however has a shortcomings as it fails to satisfy antisymmetry, which is very essential while dealing with fermions. One way of tackling this issue was to use the concept of Slater Determinant wave-function[25]. So instead of searching over all wave-function, the variational principle can only be used in the Slater-Determinant wave-function. Generalizing this concept for N electron where orbitals satisfy orthonormality condition, we obtain[26]

$$\Phi = \frac{1}{\sqrt{N!}} \begin{vmatrix} \phi_1(\mathbf{x}_1) & \phi_2(\mathbf{x}_1) & ... & \phi_N(\mathbf{x}_1) \\ \phi_1(\mathbf{x}_2) & \phi_2(\mathbf{x}_2) & ... & \phi_N(\mathbf{x}_2) \\ : & : & : & \\ : & : & : & \\ \phi_1(\mathbf{x}_N) & \phi_2(\mathbf{x}_N) & ... & \phi_N(\mathbf{x}_N) \end{vmatrix} \tag{1.7}$$

Using a Slater determinant is similar to saying that an electron independently moves of all the others, except that it feels the Coulomb repulsion due to the mean-field position of all the other electrons, and experiences an exchange interaction due the necessary asymmetry of the wave-function.

## 1.3   Hohenberg-Kohn DFT

One way of solving the time independent schrödinger equation (TISE) using Slater determinant is explained in the section above. The other approach of solving TISE is based on the concept given by Hohenberg and Kohn. The idea is to replace the complicated many body wave-function with much simpler density. There are two Hohenberg-Kohn(HK) theorems.

**Theorem 1**: For a system of interacting electrons in an external potential, the ground state electron density uniquely determines the external potential.

The theorem is proven by the *reductio ad absurdum* method. Consider two Hamiltonians $\hat{H}$ and $\hat{H}'$ differ in their external potentials by more than a trivial additive constant but correspond to the same electronic ground state $n(\mathbf{r})$ . Also consider their respective ground state wavefunctions are $\Psi$ and $\Psi'$ with the ground state energies are $E_0$ and $E_0'$ . Applying the Rayleigh-Ritz variational principle for H with wavefunction $\Psi'$, we obtain

$$E_0 < \langle \Psi'|\hat{H}|\Psi'\rangle = \langle \Psi'|\hat{H}'|\Psi'\rangle + \langle \Psi'|\hat{H} - \hat{H}'|\Psi'\rangle \tag{1.8}$$

$$E_0 < E_0' + \int d^3 r n(\mathbf{r})(v(\mathbf{r}) - v'(\mathbf{r})) \tag{1.9}$$

Similarly for $\Psi$, we get

$$E_0 < E_0' - \int d^3 r n(\mathbf{r})(v(\mathbf{r}) - v'(\mathbf{r})) \tag{1.10}$$

Adding 1.9 and 1.10, we obtain

$$E_0 + E_0' < E_0' + E_0, \tag{1.11}$$

which contradicts the assumption made proving that the external potentials that correspond to the same ground state density can not differ by more than an additive constant. Thus the ground state density uniquely determines the external potential. Hence we can now write energy as a functional of density as,

$$E[n] = T[n] + V_{ee}[n] + \int d^3 r n(\mathbf{r})v(\mathbf{r}) \tag{1.12}$$

**Theorem 2**: For a non-negative trial density $n'(\mathbf{r})$ with $\int d^3 r n(\mathbf{r}) = N$, $E[n'] \geq E_0$, $E_0$ is the ground state energy.

From theorem 1, we know that $n(\mathbf{r})$ determine its Hamiltonian $\hat{H}$ and hence the wavefunction $\Psi'$. Using $\Psi'$ as a trial wavefunction for Hamiltonian $\hat{H}'$ the energy functional is defined as,

$$\langle \Psi'|\hat{H}|\Psi'\rangle = E[n'] = T[n] + V_{ee}[n] + \int d^3 r n(\mathbf{r})v(\mathbf{r}) \tag{1.13}$$

4

But from Rayleigh-Ritz variational principle, we get,

$$\langle \Psi^{'}|\hat{H}|\Psi^{'}\rangle \geq E_0 \tag{1.14}$$

Hence

$$E[n'] \geq E_0 \tag{1.15}$$

These two theorems form the basis of modern density functional theory however, theorem 1 does not hold if the ground state wavefunction is degenerate. Also, the proof of theorem 2 is only true for V-representable density. A V-representable density is the one that comes from the wavefunction of the Schr$\ddot{o}$dinger with external potential $\upsilon(\mathbf{r})$ which are not V-representable. This limitation was lifted by using Levy-Lieb constrained search method.

## 1.4 Levy-Lieb constrained search method

Levy[27] and Lieb [28] introduced the constrained search method that eliminates the issues of HK theorems, in which the density is N-representable. A density is said to be N-representable if following conditions hold [29]

$$n(\mathbf{r}) \geq 0 \tag{1.16}$$

$$\int d^3\mathbf{r}n(\mathbf{r}) = N \tag{1.17}$$

Assume $\Psi_n$ is any normalized antisymmetric wavefunction that gives the N-representable; it may not necessarily be the ground state wavefunction of Hamiltonian $\hat{H}$. If $\Psi_g$ is the ground state wavefunction, from Rayleigh-Ritz principle,

$$\langle \Psi_n|\hat{H}|\Psi_n\rangle \geq \langle \Psi_g|\hat{H}|\Psi_g\rangle, \tag{1.18}$$

The right hand side expression is the Hohenberg-Kohn universal function.

$$Q_{HK}[n] = \langle \Psi_g|\hat{T} + \hat{V}_{ee}|\Psi_g\rangle \tag{1.19}$$

Thus it is the ground state wave function that minimizes the expectation value of $\hat{T} + \hat{V}_{ee}$. We can define a functional for any N -representable density $n\mathbf{r}$.

$$Q_{HK}[n] = \Psi \xrightarrow{min} n\langle \Psi_g|\hat{T} + \hat{V}_{ee}|\Psi_g\rangle \tag{1.20}$$

Here the minimization is over all the normalized antisymmetric wavefunctions that give the density $n(\mathbf{r})$ and we choose one that minimizes $\langle \hat{T} + \hat{V}_{ee} \rangle$. This definition does not require the knowledge of external potential $v(\mathbf{r})$ , also, the degeneracy of the ground state is not an issue as the wavefunction is constrained to yield the given density. Hence,

$$Q[n] + \int d^3 r n(\mathbf{r}) v(\mathbf{r}) \geq E_0 \tag{1.21}$$

The ground state energy can be obtained by minimizing the left-hand side of Eq. 1.21 over all N-representable densities $n(\mathbf{r})$

$$E_0 = \overset{min}{n} [Q[n] + \int d^3 r n(\mathbf{r}) v(\mathbf{r})] \tag{1.22}$$

Here the minimization is over 3-dimensional density, which is computationally much easier to do than the minimization over 3N-dimensional wavefunction.

## 1.5 Kohn-Sham DFT

The energy corresponding to the Hamiltonian due to electronic and set of nuclei is

$$E_{el} = \int \Psi^* (\sum_{i=1}^{N_{el}} -\frac{1}{2} \nabla_i^2) \Psi d\mathbf{r} + \int \Psi^* (\sum_{i=1}^{N_{el}} \sum_{j=i+1}^{N_{el}} \frac{1}{|\mathbf{r_j} - \mathbf{r_i}|}) \Psi d\mathbf{r} + \int \Psi^* (\sum_{i=1}^{N_{el}} \mathbf{V}_{ext}(\mathbf{r_i}) \Psi d\mathbf{r} \tag{1.23}$$

As seen earlier, HK theorem states that the energy of the system can be obtained entirely by system's density. In the above expression, the last two terms can be expressed in terms of energy density but not the kinetic energy term. The kinetic energy has complicated many body nature and hence cannot be written in terms of density for the interacting system. This problem was made simpler by Kohn and Sham when they introduced the concept of auxiliary system of N non-interacting system of electrons which was described by a single determinant wave-function in N "orbitals" $\phi_i$[22]. In this case, the kinetic energy and the electron density are obtained from the orbitals as

$$T_S[n] = -\frac{1}{2} \sum_{i=1}^{N_{el}} \langle \phi_i | \nabla^2 | \phi_i \rangle \tag{1.24}$$

$$n(\mathbf{r}) = \sum_{i=1}^{N_{el}} |\phi_i|^2 \tag{1.25}$$

Now, with auxiliary non-interacting electrons that has the same ground state density $n(\mathbf{r})$ , the energy functional is given as

$$E[n] = T_S[n] + V_{ext}[n] + V_H[n] + E_{xc}[n] \tag{1.26}$$

6

where

$$V_{\text{ext}}[n] = \int \hat{V}_{\text{ext}} n(\mathbf{r}) d\mathbf{r} \tag{1.27}$$

$$V_{\text{H}}[n] = \frac{1}{2} \int \frac{n(\mathbf{r}_1) n(\mathbf{r}_2)}{|\mathbf{r}_1 - \mathbf{r}_2|} d\mathbf{r}_1 d\mathbf{r}_2 \tag{1.28}$$

represent corresponding external potential and classical Coulomb interaction or Hartree energy respectively. So the Hamiltonian of this fictitious system can be decoupled into one-electron Hamiltonian as

$$\hat{H} = \sum_i^{N_{el}} \frac{1}{2} \nabla_i^2 + v^s(\mathbf{r}) \tag{1.29}$$

where $v^s(\mathbf{r})$ is some reference potential and the wavefunction is represented by the single Slater determinant of spin-orbitals

$$\Phi = \frac{1}{N!} \det[\phi_1, \phi_2 .. \phi_N] \tag{1.30}$$

where the spin-orbitals are the solution of one-electron Schrödinger equation (or KS equation)

$$(-\frac{1}{2} \nabla^2 + v^s(\mathbf{r})) \phi_i = \epsilon_i \phi_i \tag{1.31}$$

$\phi_i$ is called Kohn-Sham orbital and the eigenvalue $\epsilon_i$ the Kohn-Sham orbital energy. The beauty of KS approach is that it explicitly separates the non-interacting kinetic energy and the long-range Hartree energy, which describes the classical electrostatic repulsion between electrons, from the remaining exchange-correlation energy that must be approximated, by the unknown functional $E_{\text{xc}}$. Because the exchange-correlation (XC) energy is usually only a small fraction of the ground-state total energy, impressive accuracy can be obtained with relatively simple approximate functionals and without the large computational costs associated with the many-electron wave function.

## 1.6 Exchange Correlation Functionals

### 1.6.1 Local Density Approximation(LDA)

The exchange-correlation energy term $E_{XC}$ is entirely quantum effect which is not included in Coulomb repulsion and single particle kinetic energy. Its exact form is unknown. The simplest approach used is called Local Density Approximation (LDA).

$$E_{\text{xc}}^{\text{LDA}}[n] = \int d\mathbf{r} n(\mathbf{r}) \epsilon_{\text{xc}}^{\text{hom}}(n(\mathbf{r})) \tag{1.32}$$

In this approximation, the $\epsilon_{xc}(n)$ is the function of local value of density and can be broken into the exchange and correlation part as

$$\epsilon_{xc}(n) = \epsilon_x(n) + \epsilon_c(n) \tag{1.33}$$

The exchange part can be calculated exactly for the uniform electron gas but the exact value of functional form of correlation term is unknown and it has been simulated using quantum Monte Carlo calculations[30]. LDA has proven to be useful approximation in many occasions such as studying properties as structure, phase stability, vibrational frequency. On the other hand, it failed miserably while predicting binding energy (overestimating by 20-30%), and in many other cases. Hence there was a need for better functionals.

### 1.6.2   The Generalised Gradient Approximation(GGA)

The extension to local density approximation was done by including non-locality via gradient of density. So the functional was now dependent not only on the density but also the gradient of it.

$$E_{xc}^{GGA} = \int d\mathbf{r} \epsilon_{xc}(n, |\nabla n|) \tag{1.34}$$

It was found that having just local uniform density was not the ideal situation while dealing with electron densities of many materials, and gradient term was added. This inclusion was gradient expansion approximation(GEA) which resulted into a number of unphysical properties as it does not normalise to $-1$, it is not negative definite and it contains oscillations at large $|\mathbf{r}_2 - \mathbf{r}_1|$[31]. The GGA approximation satisfies all these properties and hence was found to significantly improve description of binding energy of molecules. These are often called "semi-local" functionals because of the presence of the $\nabla n(\mathbf{r})$ term. Some of the widely used semi-local functionals are PBE[32], PW91[33].

### 1.6.3   meta-Generalised Gradient Approximation (meta-GGA)

meta-GGAs are recently constructed functionals that depend explicitly on the semi-local information in the Laplacian of the spin density or of the local kinetic energy density. They are expressed as

$$E_{xc} = \int n(\mathbf{r}) \epsilon_{xc}(n, |\nabla n|, \nabla^2 n, \tau) d\mathbf{r} \tag{1.35}$$

where the kinetic energy density $\tau$ is obtained as

$$\tau = \frac{1}{2} \sum_i |\nabla \phi_i|^2 \tag{1.36}$$

With $\tau$ inclusion, the meta-GGA functional becomes more flexible by allowing the adherence of a greater

8

number of exact constraints compared to the GGA. Furthermore, by defining a dimensionless variable $\alpha = \frac{\tau - \tau^{\mathrm{w}}}{\tau^{\mathrm{unif}}}$, where $\tau^{\mathrm{unif}} = (3/10)(3\pi^2)^{2/3} n^{5/3}$ is the kinetic energy density of the uniform electron gas and $\tau^{\mathrm{w}} = |\nabla n|^2 / 8n$ is the von Weizsäcker kinetic energy density, meta-GGA functionals can recognize slowly varying densities, single-orbital systems, and non-covalent bonds between two closed shells [12, 34].

The empirical approach, is an alternate route to non-empirical way of constructing XC functional. This approach skips any mathematical properties of the exact functional (exact constraints), which include limits, scaling relations, equalities, and bounds and use experimental data sets, which are often of greatest interest to the user, for fitting purpose. These functionals may be good enough to interpolate between systems with similar properties but studies have shown [35, 36] that the non-empirical approach only can result in reliable prediction over the space of possible molecules, materials and properties. Minissota functional (M06-L) [37] is one of the most widely used empirical functionals.

It is worth mentioning here a relatively nascent approach, the machine–learning (ML) techniques within semi–emperical density functional approximation (DFA) design. The pioneering work on implementing ML techniques in DFT was conducted by Burke and coworkers when they used a ML approximation to construct an orbital-free non-interacting kinetic energy functional $T_s[n]$ for spinless fermion systems [38, 39]. Brockherde *et. al.* used ML to learn the Hohenberg-Kohn (HK) map between electron density and external potential to give a mechanism that bypasses solving the KS equations [40]. Several other works have focused on the XC potential problem [41, 42, 43, 44]. Other work included enforcing exact constraint in functional design using ML technique when Hollingsworth *et. al.* demonstrated that enforcing coordinate scaling constraints on kernel ridge regression models for Hook's atom model systems improved ML functional performance [45]. The ML techniques to self-consistently determine a SCAN-like meta-GGA by satisfying some of the exact constraints of SCAN is also achieved recently [46]. This approach is novel in its used of self-consistency calculation to determine the functional performance and it also demenstrated that the optimal meta-GGA did not deviate from SCAN. More recently, Nagai and his co-workers [47] introduced a method to analytically impose asymptotic constraints on ML models and constructed XC functional that is found to exhibit higher accuracy than existing standard functionals. This novel approach is soon becoming a bridge to incorporate both empirical and non-empirical approaches for the functional design.

### 1.6.4 Hybrid Functional

It is evident that even for a single-electron system, the exchange-correlation energy and Hartree energy do not cancel out each other in LDA and GGA functional and these functionals give rise to self-interaction error (SIE)[48] which results in delocalization especially for d and f states. In contrast, the Hartree-Fock (HF)[49]

theory accurately describes the single atom system and hence does not have issues regarding self-interaction error. The only shortcoming of the HF method is that it is applicable only to atomic systems where no correlation effect is included. The correlation effect is an integral part of molecular systems and also solids. As exchange-correlation functions such as LDA, GGA do capture these effects, a combination of these functional with Hartree-Fock is the major theoretical background in designing hybrid functionals[50]. Doing this allowed the HF theory to exactly describe non-interacting systems while the local exchange-correlation functionals captured accurately the description of the fully interacting systems. There are a number of different hybrid functionals used in the quantum computations. Out of them, HSE functional[51] is used for the calculation. The HSE functional can be expressed as

$$E_{xc}^{HSE} = aE_x^{SR}(\mu) + (1-a)E_x^{PBE,SR}(\mu) + E_x^{PBE,LR}(\mu) + E_c^{PBE} \tag{1.37}$$

where a is the mixing parameter whose value is $1/4$[52]. In the above expression, the first three terms correspond to the exchange energy while the last term gives the correlation energy. The mixing parameter is of huge importance here because varying its value gives us different results. The 0.25 value gives us hybrid functional while changing value to 0, results into PBE functional.

# Chapter 2

# The state-of-art research in meta-GGA, its construction and performance

## 2.1 Non-emperical mGGAs

### 2.1.1 Perdew-Kurth-Zupan-Blaha (PKZB) functional

The PKZB functional is constructed following the same philosophy as the PBE GGA functional of Perdew, Burke and Ernzerhof [32]. PBE is constructed by preserving and extending the correct formal properties of LSD. PKZB satisfies all the constraints satisfied by PBE. The constraints satisfied by the exchange energy are as follows:

1. The spin scaling relation for exchange energy

$$E_{\mathrm{x}}[n_\uparrow, n_\downarrow] = \frac{1}{2} E_{\mathrm{x}}[2n_\uparrow, 0] + \frac{1}{2} E_{\mathrm{x}}[2n_\downarrow, 0] \tag{2.1}$$

2. Uniform density scaling

$$E_{\mathrm{x}}[n_\lambda] = \lambda E_{\mathrm{x}}[n] \tag{2.2}$$

where $n_\lambda(\mathbf{r}) = \lambda^3 n(\lambda \mathbf{r})$

3. Lieb-Oxford bound

$$E_{\mathrm{x}}[n_\uparrow, n_\downarrow] \geq E_{\mathrm{xc}}[n_\uparrow, n_\downarrow] \geq -1.679 \int d^3 r \, n^{4/3} \tag{2.3}$$

The exchange energy for the spin unpolarized density is given by

$$E_{\mathrm{x}}^{MGGA}[n] = \int d^3r \, n\epsilon_{\mathrm{x}}^{\mathrm{unif}}(n) F_{\mathrm{x}}(n, \nabla n, \tau) \tag{2.4}$$

where $\epsilon_{\mathrm{x}}^{\mathrm{unif}}(n) = -\frac{3}{4\pi}(3\pi^2 n)^{1/3}$. One of the constraints that PBE fails to satisfy which is recovered by PKZB functional is the fourth order gradient expansion coefficient of Svendsen and von Barth [53] given as

$$F_{\mathrm{x}} = 1 + \frac{10}{81}p + \frac{146}{2025}q^2 - \frac{73}{405}qp + Dp^2 + O(\nabla^6) \tag{2.5}$$

where $F_{\mathrm{x}}$ is the enhancement factor.

$$p = |\nabla n|^2/[4(3\pi^2)^{2/3}n^{8/3}] \tag{2.6}$$

is the square of the reduced density gradient, and

$$q = \nabla^2 n/[4(3\pi^2)^{2/3}n^{5/3}] \tag{2.7}$$

is the reduced Laplacian density. The first two gradients of equation (2.5) are exactly known the third has uncertainty and fourth one is unknown. A new variable $\tilde{q}$ is defined that which reduces to q at a slowly varying limit

$$\tilde{q} = 3\tau/[2(3\pi^2)^{2/3}n^{5/3}] - 9/20 - p/12 \tag{2.8}$$

The PKZB meta-GGA exact form is now defined as,

$$F_{\mathrm{x}}(p, \tilde{q}) = 1 + \kappa - \frac{\kappa}{1 + x/\kappa} \tag{2.9}$$

and

$$x = \frac{10}{81}p + \frac{146}{2025}\tilde{q}^2 - \frac{73}{405}\tilde{q}p + [D + \frac{1}{\kappa}(10/81)^2]p^2 \tag{2.10}$$

where $\kappa = 0.804$ ensured that the Lieb-Oxford bound of equation (2.3) is satisfied for all possible densities. The value of D is estimated to be 0.113 which was equal to 0 in PBE functional. This value of D gives $F_x \geq 1$ which is what is expected on the slowly varying density for the surface exchange energy. The reason PBE fails to correctly capture the gradient expansion to second order for exchange energy is because it value for p in the enhancement factor is larger than the value 10/81 by a factor of 1.778. PKZB also recovers exact linear response function $\gamma_{\mathrm{x}}(k)$ up to fourth order in $k/2k_F$, where $k_F$ is the Fermi wave vector [54].

The correlation energy of PKZB is again built on the basis of PBE correlation energy, preserving all the constraints satisfied by it. The constraints for the correlation energy functional are not simple and transparent as that for the exchange functional. Some of the well-known constraints are:

1. Second order gradient expansion in slow varying limit $(t \to 0)$

$$E_c^{\text{GGA}}[n] = \int n\epsilon_c^{\text{unif}}(n)(1 + \beta_{GE}t^2)d^3 \tag{2.11}$$

where GEA second order expansion coefficient $\beta_{\text{GE}} = 0.066725$[55]

2. The rapid varying limit $(t \to \infty)$

$$E_c^{\text{GGA}}[n_\uparrow, n_\downarrow] = 0 \tag{2.12}$$

This constraint is required by the sum rule of correlation hole. In rapid varying limit, the only way to satisfy sum rule is to make the GEA correlation hole vanish.

3. High density limit $(r_s \to \infty)$

$$E_c^{\text{GGA}}[n_\uparrow, n_\downarrow] = -C \tag{2.13}$$

where C is a positive constant.

One of the advantages of meta-GGA functionals is that they can be self-interaction free for the spin polarized one electron density. The correlation energy is given by

$$E_c^{\text{MGGA}}[n_\uparrow, n_\downarrow] = \int d^3r \left\{ \begin{array}{l} n\epsilon_c^{\text{GGA}}(n_\uparrow, n_\downarrow, \nabla n_\uparrow, \nabla n_\downarrow)\left[1 + C\left(\frac{\sum_\sigma \tau_\sigma^w}{\sum_\sigma \tau_\sigma}\right)\right] \\ -(1+C)\sum_\sigma \left(\frac{\tau_\sigma^w}{\tau_\sigma}\right)^2 n_\sigma \epsilon_c^{\text{GGA}}(n_\sigma, 0, \nabla n_\sigma, 0) \end{array} \right\} \tag{2.14}$$

where $\epsilon_c^{\text{GGA}} = \epsilon_c^{\text{unif}} + H$ is the PBE GGA correlation energy per electron [32].

Also,

$$\tau_\sigma^W = \frac{1}{8}\frac{|\nabla n_\sigma|}{n_\sigma} \tag{2.15}$$

is the Weizsäcker kinetic energy density which is exact for a single electron system. For any value of C, 2.14 vanishes for one-electron density. The value of C = 0.53 gives surface correlation energy for jellium close to that of PBE. Having correlation self interaction free achieves uniform scaling behavior for all one-electron densities. In fact, it seems to work for many electron systems too. One of the shortcomings of PKZB functional is the fitted parameter which is very less in comparison to other empirical functionals.

PKZB functional performance [54] on the atomization energies of 20 small molecules is found to be remarkably

well. It seems to reduces the mean absolute error to 3 kcal/mol, more than a factor of 2 better than the PBE GGA and a factor of 10 better than LSD. The PBE GGA overbinding problem of multiply bonded molecules is reduced largely, without degrading the quality of the results for singly bonded molecules.

As discussed earlier, the PKZB functional has one empirical parameter in the exchange part which has resulted in success and failure. Some of the failures include an accurate strong-interaction limit for the correlation energy of a spin-unpolarized nonuniform density, atomization energies prediction, poor equilibrium bond lengths, poor description of hydrogen-bonded cases. There was a need to have a meta-GGA that corrected these issues and importantly it was non-empirical which resulted into the construction of TPSS functional.

### 2.1.2 Tao-Perdew-Staroverov-Scuseria (TPSS)

TPSS construction is based on PKZB. The main idea in the construction of the TPSS exchange energy is that the exchange potential must be finite at the nucleus for the one- and two-electron densities, the condition satisfied in LSD but not in GGA. TPSS also respects the constraints that are already satisfied by PKZB. The exchange energy is again obtained from the same equation given in (2.4) but with the following exchange enhancement factor

$$F_{\mathrm{x}}(p, z) = 1 + \kappa - \frac{\kappa}{1 + x(p, z)/\kappa} \tag{2.16}$$

where $\kappa = 0.804$ and the function x(p,z) is given as

$$
x(p, z) = \left\{ \left[ \frac{10}{81} + c \frac{z^2}{(1 + z^2)^2} \right] p + \frac{146}{2025} \tilde{q}_b^2 - \frac{73}{405} \tilde{q}_b \sqrt{\frac{1}{2} (\frac{3}{5} z)^2 + \frac{1}{2} p^2} \right.
$$
$$
\left. + \frac{1}{\kappa} (\frac{10}{81})^2 p^2 + 2\sqrt{e} \frac{10}{81} (\frac{3}{5} z)^2 + e\mu p^3 \right\} / (1 + \sqrt{e} p)^2 \tag{2.17}
$$

where the values of c = 1.59096 and e = 1.537 . Also

$$\tilde{q}_b = \frac{9}{20} \frac{(\alpha - 1)}{[1 + b\alpha(\alpha - 1)]^{1/2}} + \frac{2p}{3} \tag{2.18}$$

is an inhomogeneity parameter constructed from p and z, that reduces to reduced Laplacian q in the slowly varying limit. The parameter $\alpha$ is defined as

$$\alpha = (\tau - \tau^W)/\tau^{\mathrm{unif}} \tag{2.19}$$

z is defined as

$$z = \frac{\tau^W}{\tau} = \frac{5p}{(5p + 3\alpha)} \tag{2.20}$$

p is defined in equation (2.6), $\tau^W$ is defined in equation (2.15). Because of the relations obtained from equations (2.6),(2.15) and (2.20), the TPSS enhancement factor can be written as the function of s and $\alpha$, i.e. $F_x(s, \alpha)$. The important property of TPPS functional is the presence of $\alpha$ and the two different conditions that it gives rise to. In UEG, $\tau = \tau^{\text{unif}}$ and $\tau^W \to 0$ meaning $\alpha = 1$ and z =0. Similarly for one-or two-electron densities, $\tau = \tau^W$, so we have $\alpha = 0$ and z = 1. This was the first time when a meta-GGA level functional was able to distinguish the two different electron density in space. The two different densities have same reduced density so the GGA level functional could not distinguish them and hence treated them as the same density[56]. The convergence of the potential at the nucleus for one- or two electron densities in TPSS is achieved by

$$\left. \frac{dF_x(p = s^2, z = 1)}{ds} \right|_{s=0.376} = 0 \tag{2.21}$$

where s is the two-electron exponential density at nucleus. The values of c and e as discussed earlier are chosen so that equation (2.21) gives the correct exact ground state density for the hydrogen atom. The value of b=0.40 in equation is chosen so that it preserves the property fo $F_x$ to be monotonically increasing function of s even for large $\alpha$.

The correlation energy for TPSS is constructed by making some refinements to PKZB correlation functional which can be expressed as

$$E_c^{\text{MGGA}}[n_\uparrow, n_\downarrow] = \int n \, d^3r \, \epsilon_c^{\text{revPKZB}}[1 + d \, \epsilon_c^{\text{PKZB}}(\tau^W/\tau)^3] \tag{2.22}$$

where d = 2.8 hartree$^{-1}$, $\epsilon_c^{\text{revPKZB}}$ is the revised PKZB correlational functional which is expressed as

$$\epsilon_c^{\text{revPKZB}} = \left\{ \epsilon_c^{\text{PBE}}(n_\uparrow, n_\downarrow, \nabla n_\uparrow, \nabla n_\downarrow)[1 + C(\zeta, \xi)(\tau^W/\tau)^2] \right.$$
$$\left. - [1 + C(\zeta, \xi)](\tau^W/\tau)^2 \sum_\sigma \frac{n_\sigma}{n} \tilde{\epsilon}_c \right\} \tag{2.23}$$

Here $\epsilon_c^{\text{PBE}}$ is the main ingredient that already has corrrect second-order gradient expansion, scales properly under uniform density scaling to high- and low-density (weak- and strong-interaction) limits, is nonpositive and vanishes as $p \to \infty$. To ensure the exact constraint $E_c \leq 0$ for all possible densities, the value of $\tilde{\epsilon}_c$ is chose to be as

$$\tilde{\epsilon}_c = \max[\epsilon_c^{\text{PBE}}(n_\sigma, 0, \nabla n_\sigma, 0)] \tag{2.24}$$

15

Also

$$C(\zeta, \xi) = \frac{C(0, \xi)}{\{1 + \xi^2[(1+\zeta)^{-4/3} + (1-\zeta)^{-4/3}]/2\}^4} \tag{2.25}$$

where

$$C(\zeta, 0) = 0.53 + 0.87\zeta^2 + 0.50\zeta^4 + 2.26\zeta^6 \tag{2.26}$$

The performance for TPSS meta-GGA for atoms, molecules, solid and jellium surfaces are studied. For atoms, the performance is very accurate. The results show that it corrects the overestimated value of bond lengths given by PKZB in molecules, hydrogen-bonded complexes and ionic solids. TPSS shows a controlled interpolation between slowly varying and one- or two- electron limits as a result reduces the large LSD atomization energy and increases the very small LSD jellium surface energies [56].

### 2.1.3  revised TPSS (revTPSS) functional

Due to the high performance of TPSS, it was considered to be the workhorse semilocal functional for both molecules bonded to or reacting on solid surfaces. Unfortunately, due to its lattice constant error, TPSS was not widely accepted. Since lattice constant is considered very sensitive to many solid state properties like magnetism, ferroelectricity, bulk modulus and many more, it was seen that PBEsol [57], a modified PBE GGA for solids was accepted more than TPSS. PBEsol did predict good lattice constant and surface energies but the atomization energy was predicted poorly.

In 2009, Perdew *et. al.* [58] made some modification to the original TPSS exchange-correlation functional and named it revised TPSS or revTPSS. The modification was done in order to acquire good result for both geometry and energetics. The revTPSS preserves all the correct constraints of TPSS but yields lattice constant as good as the ones obtained from GGA's for solids. The semilocal exchange energy for spin-unpolarized density is given as

$$E_x^{sl}[n] = \int d^3 r n \epsilon_x^{unif}(n) F_x(p, z) \tag{2.27}$$

where $\epsilon_x^{unif}(n)$ and $F_x(p, z)$ terms are already explained above in the article. For the exchange part, specially for $\alpha \approx 1$, meta-GGA $F_x$ is modified to be more like PBSEsol GGA. A term in x is changed from $cz^2p/(a+z^2)^2$ to $cz^3p/(a+z^2)^2$ which shifts this term from 6th to 8th order in gradient expansion. $F_x$ remains unchanged for $\alpha = 0$ and large s for all $\alpha$ but its value is reduced at smaller s for $\alpha = 1$. The value of $\mu$ is changed to PBEsol value of 10/81 where c and e are adjusted accordingly to get values of c = 2.35204 and e =2.1677.

The correlation energy for revTPSS is obtained from TPSS with $\beta$ given as

$$\beta(r_s) = 0.066725(1 + 0.1r_s)/(1 + 0.1778r_s) \tag{2.28}$$

For $r_s \to \infty$, the above equation helps to cancel the second-order gradient terms for exchange and correlation energy. In addition to using equation (2.28), $C(\zeta, 0)$ in the correlation term in TPSS is replaced by

$$C(\zeta, 0) = 0.59 + 0.9269\zeta^2 + 0.62225\zeta^4 + 2.1540\zeta^6 \qquad (2.29)$$

With these corrections to exchange and correlation part, revTPSS performed about as well as the PBEsol. The lattice constant is highly accurate with MAE of 0.036. The atomization energy results show that revTPSS values are good and better on average that TPSS values. The MAE dropped from 5.9 from TPSS to 3.1 kcal/mol for revTPSS for G3 pure hydrocarbons. The MAE is obtained to be 1.0 kcal/mol slightly worse than TPSS error of 0.9 kcal/mol for hydrogen bonds.

### 2.1.4 regularized TPSS (regTPSS)

The TPSS and revTPSS functionals use both $\alpha$ and z to construct exchange enhancement factor $F_x$ and use Eq. 2.20 to eliminate z dependence. However, this equation experiences unphysical order of limits anomaly:

$$\lim_{p \to 0} \lim_{\alpha \to 0} z = 1, \lim_{\alpha \to 0} \lim_{p \to 0} z = 0 \qquad (2.30)$$

The two different ways about how both alpha and z approach to 0 results in two different values of $F_x$, ( $\lim_{p \to 0} F_x(p, \alpha = 0) = 1.1470$ and $\lim_{\alpha \to 0} F_x(p = 0, \alpha) = 1.0143$). This order of limits problem has been identified as the source of several failures in describing materials properties. Ruzsinszky *et.al* [59] proposed a solution to remove the order of limits by considering a weighted difference of the revTPSS $F_x$ at $\alpha = 0$ and ordinary $\alpha$ values,

$$F_x^{regTPSS}(s, \alpha) = F_x^{regTPSS}(s, \alpha) + f(\alpha)exp(-cs^2) \times [F_x^{regTPSS}(s, \alpha = 0) - F_x^{regTPSS}(s, \alpha)] \quad (2.31)$$

where c = 3 and d = 1.475. In Eq. (2.31), the term in square bracket which includes the order of limits problem is subtracted from the exchange enhancement factor. The function $f(\alpha) = (1 - \alpha)^3/(1 + (d\alpha)^2)^{3/2}$ is used to recover the exact fourth-order gradient expansion of revTPSS. The new exchange enhancement factor $F_x$ is now the function of $\alpha$ instead of z.

For the correlation part, a modified PBE correlation functional is used that takes a density-dependent form as shown by Eq. (2.28). The drawback however of using this correlation functional is the failure of one-electron self-correlation freedom as seen in the revTPSS correlation functional.

### 2.1.5  Made Simple (MS) functional

In 2012, Sun et al. [60] proposed a breakthrough concept in developing the meta-GGAs by discovering that $\alpha$, defined in equation (2.19) is able to distinguish three different types of chemical interactions in solids, i.e., single covalent bond ($\alpha = 0$), metallic bond ($\alpha \approx 1$) and van der Waals interaction ($\alpha \to \infty$). Based on this theory, a new meta-GGA, called meta-GGA made simple or MGGA-MS was proposed. In contrast to previously obtained meta-GGAs like TPSS, revTPSS, the importance of $\alpha$ in a meta-GGA enhancement factor is emphasized. The $\alpha$ dependence of $F_{\mathrm{x}}(s, \alpha)$ here is completely disetangled from its s dependence. Similar to revTPSS, MGGA-MS adopts the interpolation form between $\alpha = 1$ and $\alpha = 0$. The exchange enhancement factor that entangles $\alpha$ and p is expressed as

$$F_{\mathrm{x}}^{\mathrm{int}}(p, \alpha) = F_{\mathrm{x}}^{1}(p) + f(\alpha)[F_{\mathrm{x}}^{0}(p) - F_{\mathrm{x}}^{1}(p)] \qquad (2.32)$$

where

$$F_{\mathrm{x}}^{1}(p) = F_{\mathrm{x}}^{\mathrm{int}}(p, \alpha = 1) = 1 + \kappa - \kappa/(1 + \mu^{\mathrm{GE}}p/\kappa) \qquad (2.33)$$

and

$$F_{\mathrm{x}}^{0}(p) = F_{\mathrm{x}}^{\mathrm{int}}(p, \alpha = 0) = 1 + \kappa - \kappa/(1 + (\mu^{\mathrm{GE}}p + c)/\kappa) \qquad (2.34)$$

$F_{\mathrm{x}}^{\mathrm{int}}(p, \alpha)$ interpolates between $F_{\mathrm{x}}^{1}(p)$ and $F_{\mathrm{x}}^{0}(p)$ through

$$f(\alpha) = \frac{(1 - \alpha^2)^3}{1 + \alpha^3 + \alpha^6} \qquad (2.35)$$

$f(\alpha)$ is chose because it recovers second order gradient expansion, gives good jellium surface energies and Hartree–Fock exchange energies of 12 non-interacting electron hydrogenic anion with nuclear charge Z = 1. In the case of slowly varying density, the second term equation (2.32) is negligible. $F_{\mathrm{x}}^{\mathrm{int}}(p, \alpha)$ reduces to $F_{\mathrm{x}}^{1}(p)$ in order to recover second order gradient expansion. Here $\mu^{\mathrm{GE}} = 10/81$, c = 0.28771 and $\kappa = 0.29$. In comparison to revTPSS, the equation (2.32) is very simple and does not exhibit any order-of-limits problem, but still recovers revTPSS behavior in regions of small s around $\alpha \approx 1$. When the exchange functional of MS0 is combined with the correlation of PBE but with the parameters use in revTPSS discussed in the earlier section, it respects a tight Lieb-Oxford bound with $F_{\mathrm{xc}} \leq 2.137$, with standard value being 2.273. One of the important observations for made simple meta-GGA is that the monotonically decreasing dependence of enhancement factor $\alpha$ is qualitatively equivalent to monotonically increasing s-dependence which is well shown by considering 10-electron hydrogenic anion to 12-electron one and on the correlation between changes. It is seen that varying the $\alpha$-dependence in the exchange functional, results in the formation of the intershell region between the outermost core and the valence of an atom within a solid is associated with an increase of

$\alpha$ and a decrease of s. This suggests that monotonically decreasing $\alpha$-dependence of an enhancement factor is qualitatively equivalent to monotonically increasing s-dependence for the intershell regions.

The MS functional performance on lattice constants for SL20 solids, jellium surface energies, atomization energies of AE6 molecules, exchange energies of rare gas atoms and dissociation energies for W6 water clusters are studied. The atomization energies results are very accurate with MAE of 5.5kcal/mol much better than PBE. Compared to robust revTPSS, the MS functional gives better result for SL20 solids, comparable result for the jellium surface exchange-correlation energies but extremely bad for the exchange part alone, and worse for the G3 molecules. However, the MS functional predicts the most accurate dissociation energies of the W6 water clusters, suggesting a good description for the hydrogen bond.

In 2013, Sun *et al.* [61] introduced other MGGA made simple functions called MGGA-MS1 and MGGA-MS2 based upon one and two parameters respectively fitted empirically. The enhancement factor for these functionals remain the same just as used in MS0, as described by equation (2.32) but to tune the $\alpha$ dependence, a new parameter b is added in the denominator of the original $f(\alpha)$ as,

$$f(\alpha) = \frac{(1 - \alpha^2)^3}{1 + \alpha^3 + b\alpha^6} \tag{2.36}$$

For a slowly varying density where $\alpha \approx 1$, the numerator of $f(\alpha)$ controls the mechanism and the second order gradient expansion is recovered with the first principle coefficient $\mu^{\text{GE}} = 10/81$. The parameter c is determined for each $\kappa$ to reproduce the exchange energy of the hydrogen atom, where $\alpha = 0$. Since $b\alpha^6$ is negligible for $0 < \alpha < 1$ and the numerator of $f(\alpha)$ modulates the behavior of $F^{\text{int}}(p, \alpha)$ for $\alpha \approx 1$, b mainly controls the behavior for $\alpha > 1$. Similarly, $\kappa$ mainly controls the behavior of $F^{\text{int}}(p, \alpha)$ for large s. For MGGA-MS1, the value of parameters b =1 and $\kappa = 0.404$ results exact exchange energy value of 12-noninteracting-electron hydrogenic anion is obtained to be -1.8652 Ha. For MS2, the values are b = 4 and $\kappa = 0.504$ with exact exchange energy value -1.8558 Ha. This value is comparable to the exact value of -1.8596 Ha which suggests that formation of hydrogenic ion is preserved by equation (2.36).

### 2.1.6 Meta-GGA made very simple (MVS)

In 2014, for the first time, a strongly and optimally tightened bound on the exchange energy was obtained for one- and two-electron densities, and conjectured for all densities, resulting in the construction of MVS functional [62]. While LSDA is known to satisfy this constraint, all GGAs violet it strongly for good energetic predictions [63]. The meta-GGA enhancement factor is dependent upon two variables $s$ and $\alpha$. For two-electron systems, where $\alpha = 0$, it has been shown from reference [63] that an optimal lower bound on the

exchange energy will be satisfied for all possible densities if and only if

$$F_{\text{x}}(s, \alpha = 0) \leq 1.174, \tag{2.37}$$

and it is conjectured that

$$F_{\text{x}}(s, \alpha) \leq F_{\text{x}}(s, \alpha = 0) \leq 1.174 \tag{2.38}$$

This tight bound given by equation 2.38 is not satisfied at GGA level because the enhancement factor would be too small for large values of $s$ compared with famous PBE functional [32]. At meta-GGA level, however, monotonically decreasing dependence of enhancement factor $\alpha$ compensates for the monotonically increasing $s$-dependence, demonstrating a bound $F^{MGGA-MS} \leq 1.29$, close to 1.174 [60]. To include the tight bound, the enhancement factor is obtained as

$$F_{\text{x}}(s, \alpha) = \frac{h_{\text{x}}^1 + f_{\text{x}}(\alpha)[h_{\text{x}}^0 - h_{\text{x}}^1]}{(1 + bs^4)^{1/8}} \tag{2.39}$$

where

$$h_{\text{x}}^0 = 1 + k_0 \tag{2.40}$$

where $k_0 = 0.174$ for the tight lower bound ($\alpha = 0$) and

$$h_{\text{x}}^1 = 1 \tag{2.41}$$

for the Uniform electron gas (UEG) limit ($\alpha = 1$). $f_{\text{x}}(\alpha)$ is constructed as

$$f_{\text{x}}(\alpha) = \frac{(1 - \alpha)}{[(1 + e_1 \alpha^2)^2 + c_1 \alpha^4]^{1/4}} \tag{2.42}$$

which interpolates between $\alpha = 0$ and $\alpha = 1$ and extrapolates to a constant as $\alpha \to \infty$. Here $e_1 = $ -1.6665 and $c_1 = 0.7438$ are chosen. $b = 0.0233$ is obtained fitting $F_{\text{x}}(s, \alpha = 0)$ to exchange energy of hydrogen atom. The exchange part is then combined with the modified PBE GGA correlation, the one used as the correlation part of the meta-GGA MS functional.

The MVS functional is found to show better performance for the exchange energies of rare-gas atoms compared to other functional, including PBE, PBEsol, B88[64]. The exchange enhancement factor plot for MVS functional shows $F_{\text{x}}$ smaller than 1.174 and a very small variation of $s$ for $0 < s < 2$. The energetically important regions for atoms is $s \leq 1$ for $\alpha \approx 0$, where MVS shows more exchange enhancement than any GGA, which explains why MVS achieves accurate exchange energies for atoms. For molecules and solid, MVS

matches PBE for the heat of formation and matches PBEsol for bond lengths and lattice constants. MVS performance is much better than PBE for the barrier heights and the weak interactions, with a remarkable mean absolute error (MAE) of 0.8 kcal/mol for the S22 set. For G3 heats of formation, MVS is not especially impressive compared with other meta-GGAs, like meta-GGA MS, TPSS.

### 2.1.7 Strongly constrained and appropriately normed semilocal density functional (SCAN)

In 2015, Sun *et al.* [62] constructed the first meta-GGA functional that satisfies all the possible known exact constraints; 17 to be specific where about 6 for exchange, 6 for correlation and 5 for the combination of both. The functional also satisfies appropriate norms for which it is extremely accurate ie, for the energies of rare gas atoms and nonbonded interactions. The norms contain the information about $0 < \alpha < \infty$ where the nonbonded interaction contain information for $\alpha \gg 1$. The constraints satisfied are listed:

**For exchange:**

1. Exchange energy has to be negative.

2. Spin scaling relation given in equation 2.1 [65]

3. Uniform density scaling as in equation 2.2 [66]

4. Fourth-order gradient expansion [53]

5. Non-uniform density scaling [67, 68]

6. Tight bound for two-electron densities [63, 69]

**For correlation:**

1. Correlation energy has to be non-positive

2. Second order gradient expansion [68]

3. Uniform density scaling to high density limit [66]

4. Uniform density scaling to high density limit [66]

5. Zero correlation energy for any one-electron spin-polarized density

6. Non-uniform density scaling [67, 68]

**For Exchange and correlation energy combined:**

1. Size extensivity

2. General Lieb-Oxford bound [69, 32]

3. Weak dependence upon relative spin polarization in the low-density limit [70, 56]

4. Static linear response of the uniform electron gas[71]

5. Lieb-Oxford bound for two-electron densities [69]

The semilocal exchange-correlation functional is expressed as

$$E_{\text{xc}}[n_\uparrow, n_\downarrow] = \int d^3 r n \epsilon_{\text{x}}^{\text{unif}}(n) F_{\text{xc}}(r_{\text{s}}, \zeta, s, \alpha) \tag{2.43}$$

Here $\alpha$ is assumed same for the spin-unpolarized case. Also $\epsilon_{\text{x}}^{\text{unif}}$ is the exchange energy per electron of a uniform electron gas mentioned before. The exchange energy part for the spin unpolarized case is given by,

$$E_{\text{x}}[n] = \int d^3 r n \epsilon_{\text{x}}^{\text{unif}}(n) F_{\text{x}}(s, \alpha) \tag{2.44}$$

$F_{\text{x}}(s, \alpha)$ is the exchange enhancement factor. s is given by

$$s = |\nabla n| / [2(3\pi^2)^{1/3} n^{4/3}] \tag{2.45}$$

is the dimensionless density gradient. The exchange enhancement factor is interpolated between $\alpha = 0$ and $\alpha \approx 1$ and extrapolates to $\alpha \to 0$ as

$$F_{(s, \alpha)} = h_{\text{x}}^1(s, \alpha) + f_{\text{x}}(\alpha)[h_{\text{x}}^0 - h_{\text{x}}^1(s, \alpha)] g_{\text{x}}(s) \tag{2.46}$$

where $f_{\text{x}}(\alpha)$ is defined as

$$f_{\text{x}}(\alpha) = \exp[-c_{1\text{x}} \alpha / (1 - \alpha)] \theta(1 - \alpha) - d_{\text{x}} \exp[c_{2\text{x}} / (1 - \alpha)] \theta(\alpha - 1) \tag{2.47}$$

Here $h_{\text{x}}^1(s, \alpha)$ term helps to obtain fourth-order gradient expansion for slowly varying densities with small s and $\alpha \approx 1$ and it is defined as,

$$h_{\text{x}}^1(s, \alpha) = 1 + \kappa_1 - \kappa_1 / (1 + \text{x} / \kappa_1) \tag{2.48}$$

with x defined as

22

$$\mathrm{x} = \mu_{\mathrm{AK}}s^2[1 + (b_4 s^2/\mu_{\mathrm{AK}})\exp(-|b_4|s^2/\mu_{\mathrm{AK}})]$$
$$+\left\{b_1 s^2 + b_2(1-\alpha)\exp[-b_3(1-\alpha)^2]\right\}^2 \tag{2.49}$$

The parameters have values like $\mu_{\mathrm{AK}} = 10/81$, $b_2 = (5913/405000)^{1/2}$, $b_1 = (511/13500)/(2b_2)$, $b_3 = 0.5$ and $b_4 = \mu_{\mathrm{AK}}^2/\kappa_1 - 1606/18225 - b_1^2$.

For $\alpha = 0$, strongly tightened bound $F_{\mathrm{x}} \leq 1.174$ is imposed. In this case the enhancement factor reduced to $F_{\mathrm{x}}(s, \alpha = 0) = h_{\mathrm{x}}^0 g_{\mathrm{x}}(s)$ with $h_{\mathrm{x}}^0 = 1.174$. Also

$$g_{\mathrm{x}}(s) = 1 - \exp[-a_1 s^{-1/2}] \tag{2.50}$$

Here $a_1 = 4.9479$. To satisfy the constraint that exchange energy per particle has to be negative under nonuniform coordinate scaling, as $s \to \infty$, $F_{\mathrm{x}}$ vanishes as $s^{-1/2}$. $\theta$ in Eq. 2.47 is step function of x, $c_{1\mathrm{x}} = 0.667$, $c_{2\mathrm{x}} = 0.8$, $d_{\mathrm{x}} = 1.24$ and the value of $\kappa_1$ is obtained from the appropriate norm. Because of the constrained imposed it is seen that SCAN exchange enhancement factor $F_{\mathrm{x}}$ follows the Lieb-Oxford bound of $F_{\mathrm{x}} \leq 1.174$ not only for $\alpha = 0$ and instead for all values of $\alpha$, something not achieved by previous functionals.

For the correlation part, the correlation energy is obtained exactly same as the exchange part as the interpolation between $\alpha = 0$ and $\alpha \approx 1$ and extrapolation to $\alpha \to \infty$. The correlation energy is given as,

$$E_{\mathrm{c}}[n_\uparrow, n_\downarrow] = \int d^3r \, n\epsilon_{\mathrm{c}}(r_{\mathrm{s}}, \zeta, s, \alpha) \tag{2.51}$$

where $\epsilon_{\mathrm{c}}$ has the form

$$\epsilon_{\mathrm{c}} = \epsilon_{\mathrm{c}}^1 + f_{\mathrm{c}}(\alpha)(\epsilon_{\mathrm{c}}^0 - \epsilon_{\mathrm{c}}^1) \tag{2.52}$$

where $f_{\mathrm{c}}(\alpha)$ is defined as

$$f_{\mathrm{c}}(\alpha) = \exp[-c_{1\mathrm{c}}\alpha/(1-\alpha)]\theta(1-\alpha) - d_{\mathrm{c}}\exp[c_{2\mathrm{c}}/(1-\alpha)]\theta(\alpha-1) \tag{2.53}$$

The PBE form is revised for the two-dimensional limit under nonuniform scaling to get

$$\epsilon_{\mathrm{c}}^1 = \epsilon_{\mathrm{c}}^{\mathrm{LSDA1}} + \mathrm{H}_1 \tag{2.54}$$

with

$$\mathrm{H}_1 = \gamma\phi^3\ln[1 + \mathrm{w}_1(1 - g(At)^2))] \tag{2.55}$$

$$t = (3\pi^2/16)^{1/3}s/(\phi r_s^{1/2}) \tag{2.56}$$

$$w_1 = \exp[-\epsilon_c^{LSDA1}/(\gamma\phi^3)] - 1 \tag{2.57}$$

$$A = \beta(r_s)/(\gamma w_1) \tag{2.58}$$

and

$$g(At^2) = 1/(1 + 4At^2)^{1/4} \tag{2.59}$$

$\epsilon_c^{LSDA1}$ is the correlation energy of the UEG. Here $\gamma$ has the value of $\gamma = 0.031091$.

$$\beta(r_s) = 0.066725(1 + 0.1r_s)/(1 + 0.1778r_s) \tag{2.60}$$

$$\phi = [(1 + \zeta)^{2/3} + (1 - \zeta)^{2/3}]/2 \tag{2.61}$$

$\epsilon_c^0$ is designed similar to $\epsilon_c^1$ as

$$\epsilon_c^0 = (\epsilon_c^{LDA0} + H_0)G_c(\zeta) \tag{2.62}$$

where

$$\epsilon_c^{LDA0} = -b_{1c}/(1 + b_{2c}r_s^{1/2} + b_{3c}r_s \tag{2.63}$$

$$G_c(\zeta) = \{1 - 2.3631[d_x(\zeta) - 1]\}(1 - \zeta^{12}) \tag{2.64}$$

$$d_x(\zeta) = [(1 + \zeta)^{4/3} + (1 - \zeta)^{4/3}]/2 \tag{2.65}$$

The term $G_c(\zeta)$ helps correlation energy vanish for one-electron density to satisfy a constraint for atomization energy which was previously satisfied by TPSS and revTPSS. Just as $H_1$ was built, $H_0$ is given by

$$H_0 = b_{1c}\ln[1 + w_0(1 - g_\infty(\zeta = 0, s))] \tag{2.66}$$

with

$$w_0 = \exp[-\epsilon_c^{LDA0}/b_{1c}] - 1 \tag{2.67}$$

$$g_\infty(\zeta, s) = \lim_{r_s \to \infty} g(At^2) = 1/(1 + 4\chi_\infty s^2)^{1/4} \tag{2.68}$$

$$\chi_\infty(\zeta) = (3\pi^2/16)^{2/3}\beta(r_s \to \infty)\phi/[c_x(\zeta) - f_0] \tag{2.69}$$

Since,

$$c_x(\zeta) = -(3/4\pi)(9\pi/4)^{1/3}d_x(\zeta) \tag{2.70}$$

24

with $f_0$ = -0.9. So at $\zeta = 0$, $\chi(\zeta = 0) = 0.128026$ The values of the remaining parameters are $b_{1c} = 0.0285764$, $b_{2c} = 0.0889$ and $b_{3c} = 0.125541$, $\gamma_{x1}$ = -0.2259, $\gamma_{x2} = 0.2551$ and $\gamma_{c1} = 0.03888$.

In addition to these, GE4 is used to recover a nearly exact linear response for uniform density that satisfies general Lieb-Oxford bound as $F_{xc} \leq 2.215$.

The performance of SCAN for the exchange, correlation and combined exchange-correlation energies for rare-gas atoms shows that the error in $E_x$ is found to be less than 0.5% and error in $E_{xc}$ less than 0.1% shows that rare gas atoms are approximately normed. The performance for the chemical barrier height for the set of BH76 shows that MAE is 7.7kcal/mol close to the performance of M06L [37], which is heavily fitted functional. For the performance of weak interaction energies, the set of S22[72] exhibits SCAN performs better than other functionals and competes with M06L again. This improved performance is considered due to appropriate norms.

Despite these broad success, SCAN, however, is well-known to yield overly large saturation magnetization in elemental metals (e.g., Fe and Ni) which reflects an over-sensitivity of the iso-orbital indicator ($\alpha$) used in SCAN to distinguish between various chemical bonding environments[73]. The iso-orbital indicator $\alpha$ for two spin-channel are seen to be magnified by SCAN's interpolation function $f_x(\alpha)$ for these transition metals, especially for $\alpha < 1$ region resulting into an enhanced magnetization values [73].

### 2.1.8   TM

So far in this review we have concerned ourselves with meta-GGAs derived as energy densities that satisfy exact constraints. This is not the only way in which one may go about constructing new functionals, and derivation around an exchange hole model is a further way. The exchange hole,

$$e_x(\check{r}) = \frac{1}{2} \int d^3 u \frac{\rho_x(\check{r}, \check{r} + \check{u})}{u}, \tag{2.71}$$

represents the interaction between an electron at $\check{r}$ and the resulting reduction in probability of finding an electron at point $\check{r} + \check{u}$ as a result of the tendency of electrons to repel each other.

One way of using the exchange hole in functional construction is through Taylor expansion models [64, 74, 75], another is by density matrix expansion under a general coordinate transformation. Tao and Mo use the latter approach derive the TM functional following the latter approach [76], a non-empirical meta-GGA exchange functional.

Much like other meta-GGA functionals, TM exists as an interpolation between two limiting cases,

$$F_x = w(z)F_x^{DME} + [1 - w(z)]F_x^{SC}, \tag{2.72}$$

25

where $w(z) = (z^2 + 3z^3)/(1 + z^3)^2$, with $z$ the familiar iso-orbital indicator of Eq. 2.20. This interpolation is made between a functional derived from the density matrix expansion, $F_{\mathrm{x}}^{\mathrm{DME}}$, and the fourth order slowly varying density gradient expansion for exchange, $F_{\mathrm{x}}^{SC}$.

For correlation, Tao and Mo identify three constraints as important: one electron self-interaction freedom, the correct slowly varying density limit, and near-exactness and spin independence for the low-density limit. Following these conditions they take the TPSS correlation functional for use with TM exchange, but simplify Eq. 2.25 to,

$$C(\zeta, \chi) = \frac{0.1\zeta^2 + 0.32\zeta^4}{\left\{1 + \chi^2 \left[(1+\zeta)^{-4/3} + (1-\zeta)^{-4/3}\right]/2\right\}^4}. \tag{2.73}$$

The resulting functional is accurate for many systems[76, 77], though it's accuracy for some problems is severely limited by an order-of-limits problem in its design, as will be discussed shortly.

A revision of the functional was proposed by Jana, Sharma, and Samal, termed "revTM" [78] which aims to improve functional performance by adjusting the slowly varying exchange term, $F_{\mathrm{x}}^{\mathrm{SC}}$. They report improved cohesive energies, metal surface energies, lattice constants, and bulk moduli compared to TM. The revision does not resolve the order-of-limits problem however, so performance for transition pressures likely remains limited.

Like TPSS it suffers an order-of-limits problem that harms its accuracy for transition pressure predictions [79]. Like TPSS, this is a result of the use of $z$ in the interpolation function in combination with the $p$ dependence of the interpolated energy densities.

Revised forms have been proposed that adjust the correlation functional following the philosophy of revTPSS. The OOL problem is not a necessary limitation of TM[79] however, and [80] propose a "regTM" that avoids it.

They do this by taking a regularised iso-orbital indicator,

$$z' = \frac{1}{1 + \left(\frac{3}{5}\right)\left[\frac{\alpha}{p + f(\alpha, p)}\right]}, \tag{2.74}$$

where,

$$f(\alpha, p) = \frac{(1-\alpha)^3}{(1 + (d\alpha)^2)^{3/2}} e^{-cp}, \tag{2.75}$$

with $d = 1.475$ and $c = 3.0$. This regularisation was first suggested in Ref. [59] for the revTPSS functional. While the regTM functional thereby avoids the order-of-limits problem, the "regTM" correlation constructed alongside it fails to be one-electron self-correlation free. Despite this limitation it maintains the parent functional's good overall performance and significantly improves transition pressure predictions.

### 2.1.9 TASK

The TASK functional was proposed by Aschebrock and Kümmel in Ref. [81] as a meta-GGA that places emphasis on minimising self-interaction error without including non-local ingredients beyond $\tau$. This is achieved by focusing on the potential response and derivative discontinuity features, rather than being exclusively concerned with energy densities. At the time of writing only a TASK exchange functional has been published, which is recommended for use with PW92 local density approximation type correlation [68], until an appropriate correlation functional has been determined.

The TASK exchange functional is derived by first noting that a derivative discontinuity of appropriate size and sign can be determined by enforcing,

$$\frac{\partial e_{\mathrm{x}}}{\partial \tau} > 0, \tag{2.76}$$

by construction. Following the iso-orbital indicator driven interpolation ansatz this leads one to the design constraint of,

$$\frac{\partial F_{\mathrm{x}}}{\partial \alpha} < 0, \tag{2.77}$$

with a more negative slope corresponding to a larger band gap. This is in agreement with the tight two electron bound constraint of $F_{\mathrm{x}}(s, \alpha) \leq 1.174$ and results in a tendency to localise electrons.

Following this analysis TASK adopts the $\alpha$ driven interpolation framework of SCAN, but redesigns the interpolation function to use Chebyshev rational functions. As TASK seeks to maximise the derivative with respect to $\alpha$ the interpolation derivatives do not disappear at $\alpha \to 1$ as they do for SCAN, and so the slowly varying density exchange, $h_{\mathrm{x}}^1$, is modified to maintain the correct slowly varying density gradient expansion up to fourth order. The correlation functional tailored for use with TASK exchange, however, has not been constructed yet and hence PW92-LDA [68] correlation is used along with the exchange.

TASK shows much improved band gaps for most systems when compared against SCAN and the band gaps values are closer to experiment for systems ranging from semiconductors to minerals like MgO and LiCl. The chemical performance is however found to be less impressive, probably as a result of its relatively primitive correlation functional.

### 2.1.10 Regularized and Restored SCAN

The SCAN functional, otherwise successful, has a well reported numerical problems [82, 83] that prevent its application to especially sensitive or large scale problems. In addition to this the SCAN XC potential diverges in single orbital systems complicating the generation of pseudopotentials for hydrogen and helium
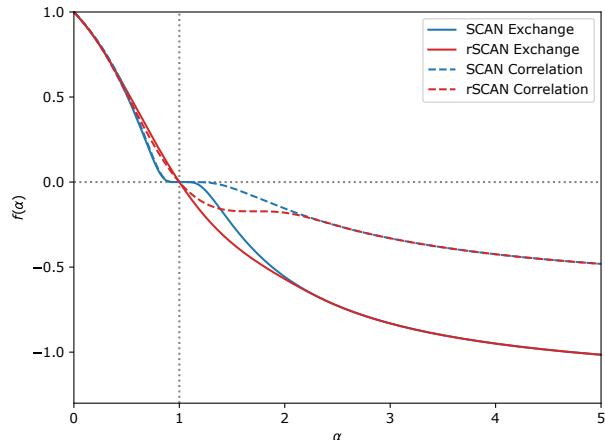
Figure 2.1: Comparison of the SCAN and rSCAN interpolation functions.

atoms [84, 85]. Some modifications to SCAN were presented by Mezei, Csonka, and Kállay that improve the accuracy of atomisation energies for multi-reference systems but does not address the numerical sensitivities.

In response to this Bartok and Yates proposed a regularisation of SCAN termed "rSCAN". This made two substitutions.

The first regularising the $\alpha$ iso-orbital indicator,

$$\alpha \to \alpha' = \frac{\tilde{\alpha}^3}{\tilde{\alpha}^2 + \alpha_r} \tag{2.78}$$

where,

$$\tilde{\alpha} = \frac{\tau - \tau_W}{\tau_U + \tau_r}, \tag{2.79}$$

where $\alpha_r = 10^{-3}$ and $\tau_r = 10^{-4}$ are regularisation constants. This controls the single orbital diverge at the expense of breaking the uniform density limit and coordinate scaling constraints obeyed by SCAN.

The second regularisation is to change the interpolation from the piecewise exponential function of SCAN which introduce a kink around $\alpha = 1$, into a smooth polynomial interpolation, see Figure 2.1.

While these are successful in resolving the numerical problems, they break four of the exact constraints obeyed by SCAN. As a result the functional's accuracy is less transferable and is degraded for atomisation energies [86, 85].

In following work, Furness, Kaplan, Ning, Perdew, and Sun modify rSCAN to restore adherence to the exact constraints while keeping the functional's useful regularisations[79]. The resulting r$^2$SCAN functional obeys all the exact constraints SCAN does excepting the fourth order slowly varying density gradient expansion. This restoration of the exact constraints to the well regularised rSCAN form gives a functional

that maintains the accuracy of SCAN while avoiding the parent's numerical issues [79, 87].

## 2.1.11 De-orbitalised versions

Out of the two ingredients in meta-genralized approximations, $\tau(\mathbf{r})$ is more commonly used and is well understood as recognizing different chemical environments through iso-orbital indicator variables, as discussed above. While theoretically convenient, $\tau$ introduces an implicit dependence on the KS orbitals, which brings some complications. 1) It reduces computational efficiency by requiring additional basis function derivatives to be computed on the numerical quadrature grid, which can be more costly for Fourier transform based periodic codes. 2) It prevents the functional being used in orbital-free DFT calculations. 3) Evaluation of the XC potential for $\tau$-dependent functionals requires either optimised effective potential (OEP) techniques [88, 89], or a generalised KS scheme[90, 91, 92]. While a generalised KS treatment can be computationally convenient, the effective XC potential operator of a $\tau$ dependent mGGA is no longer a multiplicative function, $v_{\text{xc}}(\mathbf{r})$, and is instead a non-local operator, $\hat{v}_{\text{xc}}$.

Mejia-Rodriguez and Trickey [93, 13, 94] circumvented these complications when they replaced $\tau(\mathbf{r})$ with functions of laplacian, $\nabla^2 n(\mathbf{r})$ in many mGGA XC functionals to recover similar (but not identical) performance to the parent functionals. The construction of these laplacian based density functional is achieved by replacing the exact orbital-dependent kinetic-energy density $\tau$ with an approximate kinetic-energy density $\tau_s$. The iso-orbital indicator becomes,

$$\alpha = \frac{\tau_s - \tau_W}{\tau_U} \tag{2.80}$$

where $\tau_\theta = \tau_s[n] - \tau_W[n]$ is an approximation to the exact Pauli term. The approximate kinetic-energy density $\tau_s$ is chosen from a variety of available single-point kinetic energy density functionals (KEDFs) which would produce $\tau_\theta$, obtained by the Perdew and Constantin parameterization of $\tau$ [95]. Thus obtained orbital-free version of SCAN and $r^2$SCAN (SCAN-L and $r^2$SCAN-L) are found to predict smaller magnetic moments in the ferromagnets and also predict more accurate lattice constants of simple metals. It has also been shown that $r^2$SCAN has a computational cost similar to that of PBE in solids. [93, 13, 94].

Recently, Kaplana and Perdew [96] extended the work by Mejia-Rodriguez and Trickey by constructing an orbital-free $r^2$SCAN called OFR2 (orbital-free $r^2$SCAN) by restoring the the fourth-order gradient expansion for exchange, the constriant missing in $r^2$SCAN-L, by simplifying the construction of the approximate $\tau$ (consider Ref. [96] for more detail about construction). Doing so, OFR2's performance on lattice constant of solids is found to match to that of SCAN. It also more accurately describes transition-metal magnetism and structural properties of alkali metals than $r^2$SCAN but fails to perform well on their cohesive energies. For

molecules, however, the performance is poor with MAE of 11kcal/mol for AE6 in comparison to r$^2$SCAN (3.65 kcal/mol) and r$^2$SCAN-L (3.92 kcal/mol).

# Chapter 3

# Sensitivity of the electronic and magnetic structures of cuprate superconductors to density functional approximations

## 3.1   Introduction to Superconductivity

### 3.1.1   Conventional Superconductors

The superconductivity phenomenon was first discovered by Kamerlingh Onnes in 1911[97] where he observed a certain drop in the resistivity of the mercury after a certain temperature. The second incident of superconductivity was discovered by Meissner and Ochenfeld in 1933[98] when they observed the expulsion of the magnetic flux from the superconducting state. After that, a lot of work and major advances were made in an attempt to explain the superconducting phenomenon. But it was only at 1957, the universally accepted microscopic theory of the phenomenon was successfully explained by Bardeen, Cooper, and Schrieffer[99] for which they were awarded Noble prize in 1972.

BCS theory is based on the assumption that when the attractive Cooper pair interaction dominates the Coulomb repulsive force, superconductivity arises. Cooper pair is electron-electron bound pair, which is weak in nature, mediated by phonon interaction. The electrons which are fermions, after pairing by phonon

coupling, act as bosons and hence condense into a single coherent ground state which allows the other electrons to move through the crystal without losing their momentum. The paired electrons have equal and opposite momentum so the total momentum of the electrons is conserved and hence superconductivity arises. Since the Coulomb repulsion is strong so the pairs are far from each other and the attraction via phonon is long range; thus is a quantum mechanical explanation.

### 3.1.2 High-Temperature Superconductors

The conventional superconductors were only possible at a very low temperature so the search for high-temperature superconductors continued for a couple of decades after that. In 1986, Bednorz and Müller, discovered a new class of superconducting materials, LaBaCuO, showing superconductivity at 30K[100]. The following year, the discovery of $YBa_2Cu_3O_{7-\delta}$ which was superconducting at 90K[101] resulted in high-temperature superconductivity as a serious area of research. The common component in all these high-temperature superconductors was the presence of $CuO_2$ plane and they were referred to as "cuprates".

The superconductivity in cuprates has always been elusive to understand. In their stoichiometric form, these materials are antiferromagnetic Mott insulators. The BCS theory explaining superconductivity in conventional superconductors suggest that magnetism cannot co-exist with superconductivity. This difference between new high-temperature superconductors(HTSCs) and conventional superconductors created great excitement and scientists all over the world are working on to understand the physics, which till date is still not fully comprehended.

Cuprates are layered materials whose elementary units are $CuO_2$ planes, separated by spacer layers containing other atoms. The spacer layers are where dopant atoms are introduced and not directly into the $CuO_2$ planes as shown in figure 3.1. The doping can be both electrons as well as the hole. Hole doped systems have been studied more because these systems have a high superconducting temperature. My work is focused on one of the hole-doped systems, Lanthanum copper oxide ($La_2CuO_4$).

Just as the Cuprate family, LCO consists of layered $CuO_6$ layer where the Cu and O atoms together form an octahedral structure as shown in figure 3.2. Depending upon the octahedral tilt modes, LCO is found to exhibit a variety of phases. High Temperature Tetragonal phase (HTT) where all $CuO_6$ octahedra are aligned axially is a high-temperature phase. A transition of phase occurs at a low temperature resulting into (LTO) phase where $CuO_6$ octahedra are aligned along the (010) direction in alternate layers. A low-temperature tetragonal (LTT) phase is a special condition obtained by doping Ba or by substituting La with Nd, where octahedral tilts of the Cu–O–Cu bonds are aligned along the (110) zone diagonal. These different phases hold true for both pristine LCO and Strontium doped $La_{2-x}Sr_xCuO_4$ (LSCO) system. My thesis work is based on
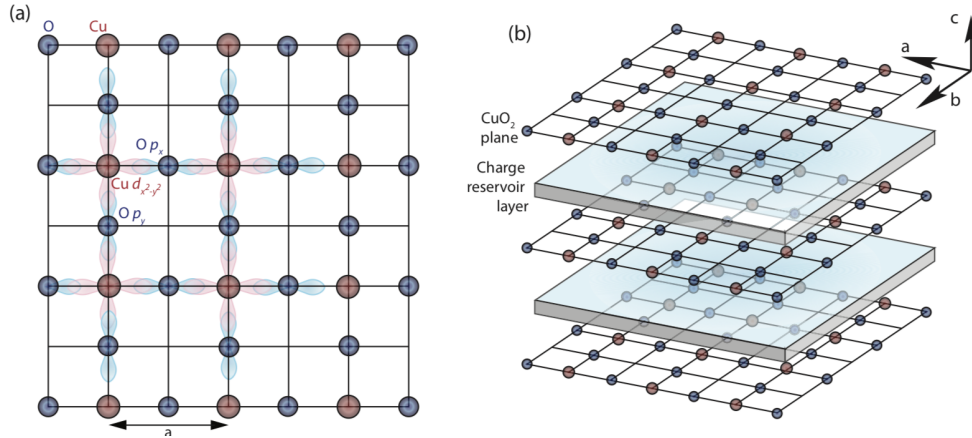
Figure 3.1: (a) CuO$_2$ plane where Cu atoms in red and oxygen atoms in blue. (b) Cuprate crystal structure with alternatting CuO$_2$ planes and spacer layer [1].

both the pristine and the doped systems. The different phases of LCO/LSCO is shown in figure 3.2
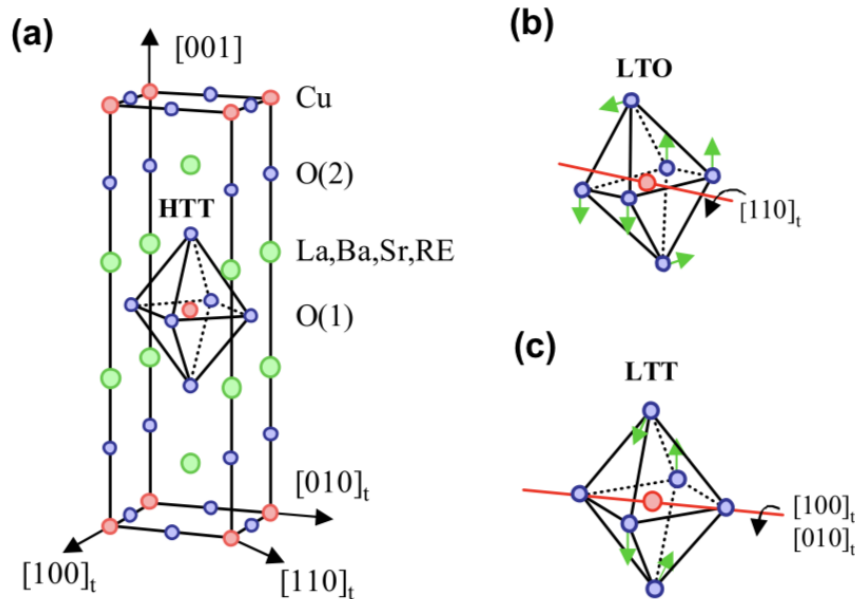


Figure 3.2: The crystal structure of (a) HTT (b) LTO (c) LTT phases depending upon CuO$_2$ octahedra tilts [2].

## 3.2  Problem/Motivation of the research

Ever since the discovery of cuprate superconductivity in 1986 by Bednorz and Müller[100], the anomalous behavior of the pristine as well as the doped cuprate has eluded theoretical explanation and still remains an unsolved problem in condensed matter physics. La$_2$CuO$_4$ (LCO), in particular, has been a significant challenge

to describe within a coherent theoretical framework. The Hohenberg-Kohn-Sham density functional theory (DFT)[21, 22] with some classes of popular exchange-correlation (XC) approximations fails spectacularly to capture the insulating antiferromagnetic ground state of LCO, let alone the metal insulator transition (MIT) under doping. [102]. Specifically, the local spin-density approximation (LSDA) XC functional incorrectly predicts the parent compound to be a metal, yielding a vastly underestimated value for the copper magnetic moment of $0.1\mu_B$ [103, 104] compared to the experimental value of $0.60\pm0.05$ $\mu_B$[7]. The PBE generalized gradient approximation (GGA) [32] still predicts LCO to be a metal with a slightly improved magnetic moment of $0.2\mu_B$ [105]. The Becke-3-Lee-Yang-Parr (B3LYP)[106, 107, 50, 108] hybrid functional correctly explains the AFM ground state in LCO but fails to capture the MIT upon doping [109]. These failures have led to the (incorrect) belief that DFT is fundamentally incapable of capturing the physics of the cuprates and other correlated materials. Therefore, "beyond DFT" methodologies, such as the quantum Monte Carlo methods [110], DFT+U [111, 112], and dynamical mean-field theory (DMFT)[113, 114, 115] have been introduced to handle strong electron correlation effects. These approaches have been useful for understanding the physics of the cuprates, although they typically introduce *ad hoc* parameters, such as the Hubbard U, to tune the correlation strength, which limits their predictive power.

Recent progress in constructing advanced density functional approximations (DFA) provides a viable new pathway for addressing the electronic structures of correlated materials. In particular, the strongly-constrained and appropriately-normed (SCAN) meta-GGA [12] , which obeys all 17 known constraints applicable to a meta-GGA functional, has been shown to accurately predict many key properties of the pristine and doped $La_2CuO_4$ and $YBa_2Cu_3O_6$ [3, 116, 117]. In LCO, SCAN correctly captures the size of optical band gap, the magnitude and the orientation of the copper magnetic moment, and the magnetic form factor in comparison with the corresponding experimental results [116]. In near-optimally doped $YBa_2Cu_3O_7$, 26 competing uniform and stripe phases are identified [117]. In this case, the treatment of charge, spin, and lattice degrees of freedom on the same footing is crucial in stabilizing the stripe phases without invoking any free parameters. Furthermore, SCAN has been applied to the $Sr_2IrO_4$ parent compound yielding the subtle balance between electron correlations and strong spin-orbit coupling in excellent agreement with experiment[118].

SCAN's success in the copper and iridium oxides is a significant achievement for the DFT and suggests capability for treating a wider class of correlated materials. SCAN, however, is well-known to yield overly large saturation magnetization in elemental metals (e.g., Fe and Ni) [119, 120, 121] and has the problem of numerical instabilities [82, 122, 123, 79], which may limit its applicability. A number of natural questions therefore arise: Is SCAN a unique XC density functional that is able to correctly capture a variety of properties of the cuprates or do other meta-GGAs perform similarly well? How do hybrid XC functionals perform in comparison? Answers to these questions are important for benchmarking the performance of

SCAN and related DFAs, and for opening a pathway to their more extensive use.

With this motivation, this paper compares the accuracy of 13 DFAs. In particular, we assess the efficacy of LSDA [124, 68], PBE[32], SCAN[12], SCAN-L[93], rSCAN[123], r$^2$SCAN[79], r$^2$SCAN-L[94], TPSS[56], revTPSS[58], MS0[60], MS2[61], M06L[37], and HSE06[125, 126, 127, 128] with respect to their predictions for crystal, electronic, and magnetic structures of the pristine and doped prototypical high-temperature superconductors La$_{2-x}$Sr$_x$CuO$_4$. Various XC density functionals employed span the levels of the Perdew—Schmidt hierarchy[129], allowing us to evaluate the performance of each functional class for the description of correlated condensed matter systems.

## 3.3 Computational details

The calculations were performed using the pseudopotential projector-augmented wave method[130] implemented in the Vienna ab initio simulation package (VASP)[131, 132]. The energy cutoff for the plane-wave basis set was taken to be 550eV for all meta-GGA calculation whereas 520eV for HSE functional. To sample the Brillouin zone, for meta-GGAs, $8 \times 8 \times 4$ Γ-centered k-point mesh was used while a small mesh of $6 \times 6 \times 2$ was used for HSE functional. The structures were initially relaxed for meta-GGA using conjugate gradient algorithm with an atomic force tolerance of $0.008eV/A^o$ and total energy tolerance of $10^{-5}eV$. For HSE functional, the unrelaxed structure was used for the calculation. The computational cost for HSE increases drastically as compared to meta-GGA calculations so smaller energy, smaller k-point and unrelaxed structures were used. The unit cell was rotated to obtain a $\sqrt{2} \times \sqrt{2}$ AFM unit cell[133] where Sr was doped in place of one La to obtain a doped structure. In the AFM structure obtained, due to crystal symmetry, lanthanum substitution position was equivalent at all position so replacing one La by Sr resulted in an effective average doping of 25%.

## 3.4 Results

### 3.4.1 Crystal structure

The phase diagram of the cuprates displays a complex intertwining of magnetic and charge ordered states that evolve with doping to reveal a superconducting dome. Interestingly, structural phase transitions associated with various octahedral tilt modes[134, 135] mainly follow the electronic phase boundaries.[136] At high temperatures LCO is found to be tetragonal (HTT) with all CuO$_6$ octahedra aligned axially. A phase transition occurs upon lowering the temperature resulting in a low-temperature orthorhombic (LTO) phase where the octahedra are tilted along the (110) zone diagonal. An additional low-temperature tetragonal
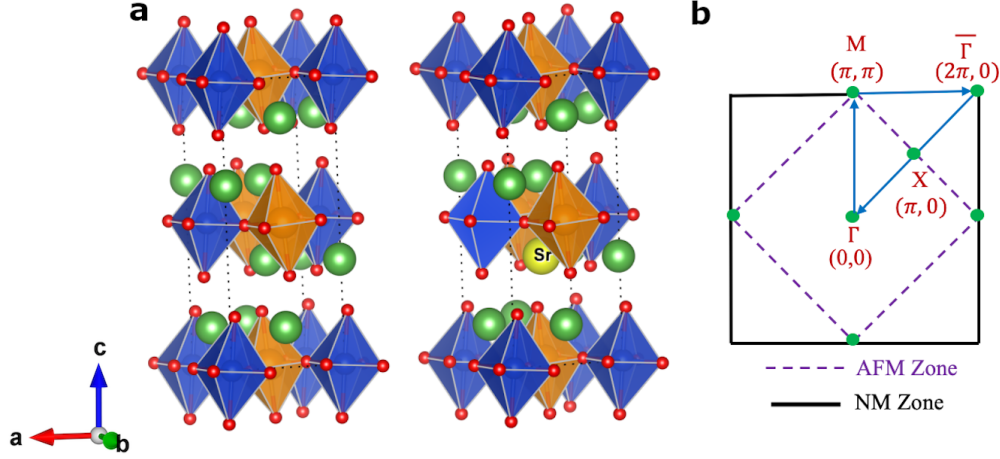
Figure 3.3: (a) Theoretically predicted crystal structure of $La_{2-x}Sr_xCuO_4$ in the LTO phase for $x = 0.0$ and 0.25. Copper, oxygen, lanthanum, and strontium atoms are represented by blue, red, green, and yellow spheres, respectively. Octahedral faces are shaded in blue (orange) to denote spin-up (down). Black dotted lines mark the unit cell. (b) A schematic of the non-magnetic (NM) and anti-ferromagnetic (AFM) Brillouin zone, where the path followed in the electronic dispersions in FIG.3.9 is marked.

(LTT) phase arises upon substituting La with Ba or Nd, where the octahedral tilts are aligned along the (100) and (010) directions in alternating $CuO_2$ layers. Therefore, in order to properly disentangle the connection between the electronic and the physical properties of the cuprates, it is imperative to capture the correct ground state crystal structure. To calculate the total energies of various crystalline phases, we consider the $\sqrt{2} \times \sqrt{2}$ supercell of the body-centered-tetragonal I4/mmm primitive unit-cell to accommodate both the octahedral tilts and the $(\pi, \pi)$ AFM order within the $CuO_2$ planes. We treat the doping within a relatively simple "$\delta$- doping" scheme in which one La atom in the supercell is replaced by a Sr atom to yield an average hole doping of 25%[3]. This approach has been recently used for doping LSCO via molecular beam epitaxy techniques[133]. Figure 3.3 (a) shows the crystal structures of LCO and LSCO in the LTO phase where the $CuO_6$ octahedra have been shaded blue and orange to represent the AFM order. The Sr doping site is also indicated.

Figures 3.4 (a) and 3.4(d) present energy differences between the AFM and NM phases for the pristine and doped $La_{2-x}Sr_xCuO_4$ in each crystal structure for the DFAs considered. Firstly, we note that LSDA does not stabilize an AFM order over the Cu sites, whereas in PBE the AFM phase is marginally more stable, consistent with previous studies[3]. All meta-GGAs find the AFM phase to be the ground state, with an energy separation of $-0.2$ to $-0.9$ eV between the AFM and NM states in the pristine structure, whereas in the doped case the energy difference is smaller by a factor of two. These trends are consistent across the various crystal structures.

Figures 3.4 (b-c) and 3.4(e-f) present energy differences between the HTT, LTT, and LTO crystal structures

36
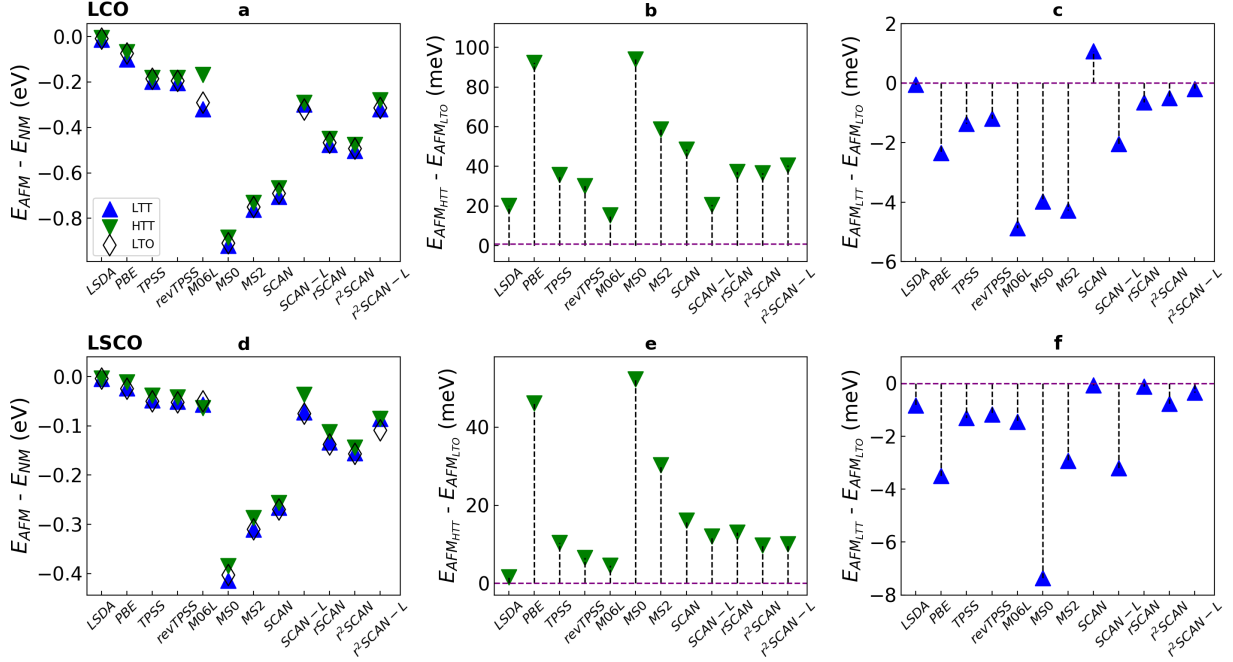
Figure 3.4: (**a**) Energy differences between the G-AFM and NM phases for the HTT (green upside-down triangle), LTO (white diamond), and LTT (blue triangle) structures for various XC density functionals. (**b-c**) Relative energies per formula unit for AFM in pristine LCO between LTO and HTT (**b**) and LTO and LTT (**c**). (**d- f**) Same as (**a-c**) except that these panels refer to LSCO instead of LCO.

for pristine and doped $La_{2-x}Sr_xCuO_4$ for various density functional approximations. In all cases, the HTT phase lies at much higher energy compared to the LTO and LTT phases. Difference between the LTO and LTT appears more delicate. For the undoped case, only SCAN correctly predicts LTO to be the ground state, while LSDA, rSCAN, r²SCAN, and r²SCAN-L find LTO and LTT to be nearly degenerate with an energy difference of less than 1 meV. In the doped case, all XC functionals correctly predict the ground state to be LTT [137], while SCAN and rSCAN yield a marginal energy difference between LTT and LTO. Note that near 12% doping, the LTO and LTT phases are found experimentally to be virtually degenerate [3].

Figure 3.5 shows the equilibrium lattice constants for LCO in the HTT, LTT, and LTO phases. The LSDA and PBE values were taken from Ref. [3] and experimental values from Refs. [138, 139, 140]. The LSDA is seen to underestimate the lattice constant for all crystal structures. PBE, on the other hand, underbinds the atoms and yields an exaggerated orthorhombicity in the LTO phase, similar to the super-tetragonality spuriously predicted by PBE for ferroelectric materials [141]. TPSS, revTPSS, MS0, MS2, SCAN, SCAN-L, rSCAN, r²SCAN and r²SCAN-L correct PBE by reducing the $b$ lattice constant in line with the experimental values in LTO and LTT.

Curiously, all XC density functionals underestimate the lattice parameters in the HTT phase, except for
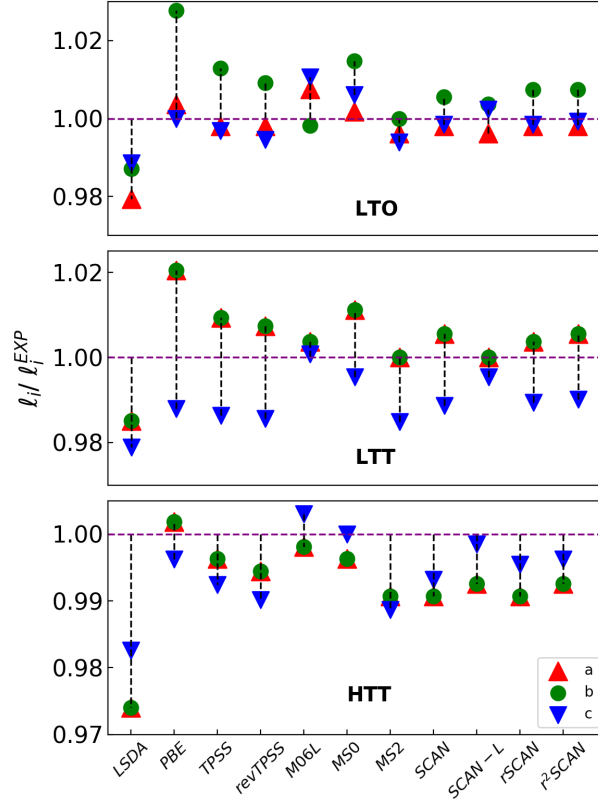
Figure 3.5: Comparison of the theoretically obtained and experimental lattice constants a, b, c for the HTT, LTT, and LTO crystal structures using various density functional approximations for $La_2CuO_4$. The lattice constant values are divided by corresponding experimental values.

PBE and M06L. The empirical M06L XC functional predicts lattice constants with greater accuracy than other XC functionals in all cases. Note that HTT is a high-temperature phase and therefore the experimental lattice constant should, in principle, be corrected for finite-temperature effects for comparison with DFT results. Figure 3.6 considers the octahedral tilt angles. Here, M06L underestimates the tilt angle, while all other XC functionals overestimate it within a few degrees. We note, however, that the experimental tilt angles should be regarded as average values because the $CuO_6$ octahedra are not rigid objects: these octahedra couple to various phonon modes and deform dynamically. Molecular dynamics or phonon calculations will be needed to capture the octahedral tilts more accurately.

Lattice constants and octahedral tilts are not included for $r^2$SCAN-L in Figs. 3.5 and 3.6 because we found a non-zero stress tensor at the energy-minimized equilibrium volume in this case. This suggests an error in the stress tensor implementation of $r^2$SCAN-L, See Section S3 of Supplementary Materials for more details. The experimental structures were therefore used for the electronic and magnetic properties calculations using $r^2$SCAN-L . The experimental structures were also used for HSE06 based calculations as the computational
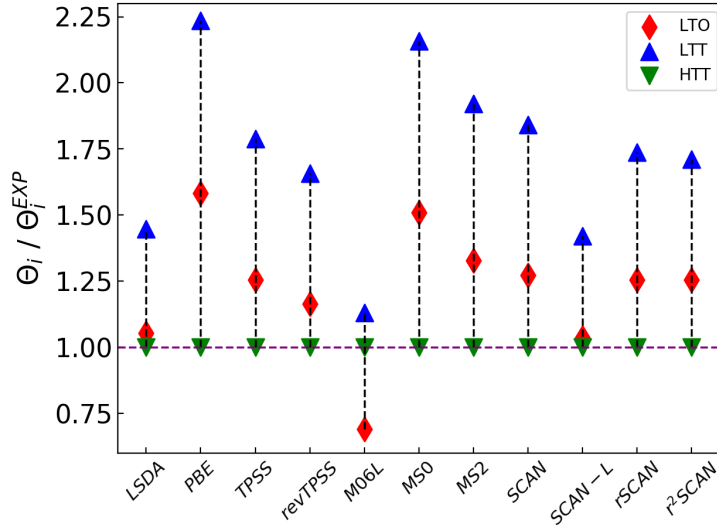
Figure 3.6: Theoretically predicted values of octahedra tilt angle using various density functional approximations for LCO. The LSDA and PBE value are taken from reference [3] The octahedra tilt values for LTO, LTT and HTT are divided by corresponding experimental values.

cost for hybrid XC functionals is much greater than the meta-GGAs.

Notably, within the "SCAN family" of XC density functionals (SCAN, SCAN-L, rSCAN, and r$^2$SCAN) all members show similar performance for lattice constants and tilt angles (Figs.3.5 and 3.6). The potential speedup of running r$^2$SCAN-L in a density-only KS scheme and the improved numerical performance inherited from r$^2$SCAN suggest that r$^2$SCAN-L could be used to optimize geometry followed by a single point SCAN or r$^2$SCAN calculation for obtaining electronic properties. This approach may also present an advantage of minimizing the numerical challenges associated with SCAN. A similar scheme was suggested in Ref. [87] in the context of spin-crossover prediction.

### 3.4.2 Electronic and Magnetic Structures

Figure 3.7 compares the theoretically predicted electronic bandgaps and copper magnetic moments obtained from various XC functionals for the three crystalline phases of LCO. The range of experimentally observed bandgaps [4, 5, 6], and median copper magnetic moments[7] are marked by the grey and blue shaded regions, respectively. LSDA and PBE greatly underestimate the bandgaps and magnetic moments because they fail to stabilize the AFM order. A large variation is seen in the results of the meta-GGAs. TPSS and revTPSS both underestimate the bandgaps and magnetic moments. MS0, MS2 and SCAN yield values that lie within the experimental ranges. Other meta-GGAs predict reduced bandgaps and magnetic moments that are below experimental values. M06L underestimates both the moment and the bandgap
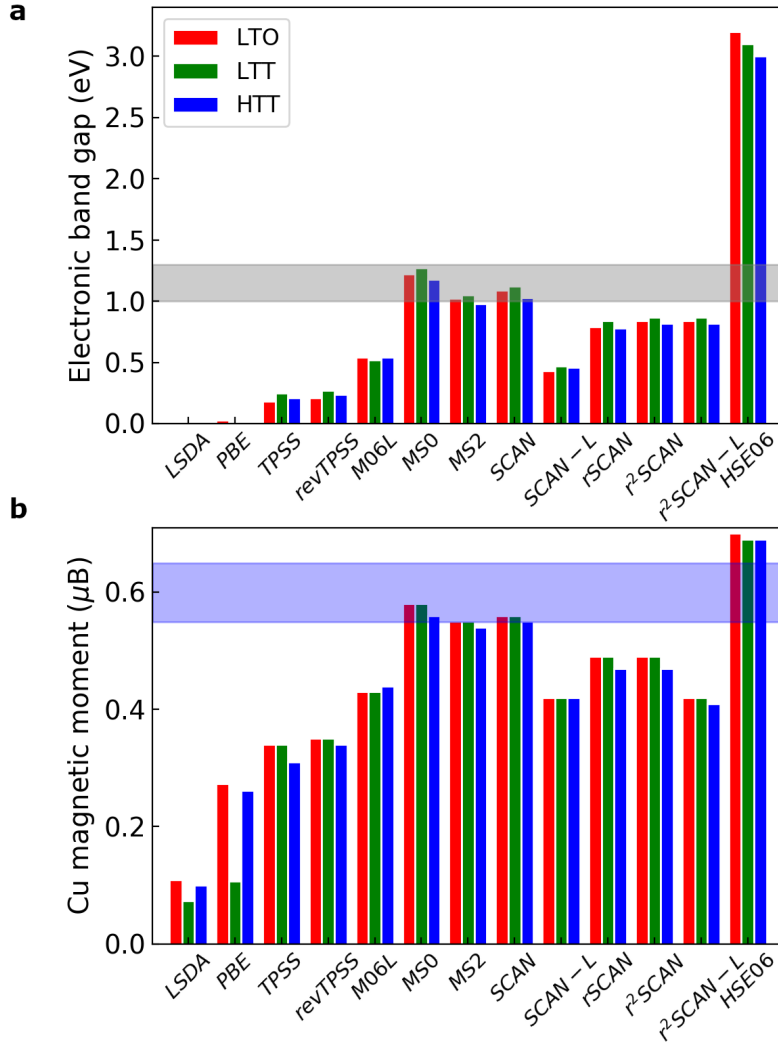
Figure 3.7: Theoretical predicted values of (**a**) electronic band gap and (**b**) copper magnetic moment for all three phases of pristine LCO obtained within various density functional approximations. The gray shaded region in (**a**) gives the spread in the reported experimental values for the leading edge gap [4, 5, 6]. In (**b**), the blue shaded region represents the experimental value of magnetic moment [7]. The LSDA and PBE values are taken from Ref. [3]

value, possibly due to the bias towards molecular systems which is encoded in its empirical construction. M06L yields ferrimagnetic order and, therefore, the average of the magnetic moment is given in Fig. 3.7. Finally, the hybrid functional (HSE06) overestimates bandgaps, predicting a value of around 3 eV, and it also overestimates magnetic moments.

Ando[142] has stressed that one should estimate the bandgap not from the lowest energy absorption peak, but from the leading edge gap in the optical spectra[4]. The leading edge gives the minimum energy needed by an electron to be elevated from the valence to the conduction band, in good agreement with the transport
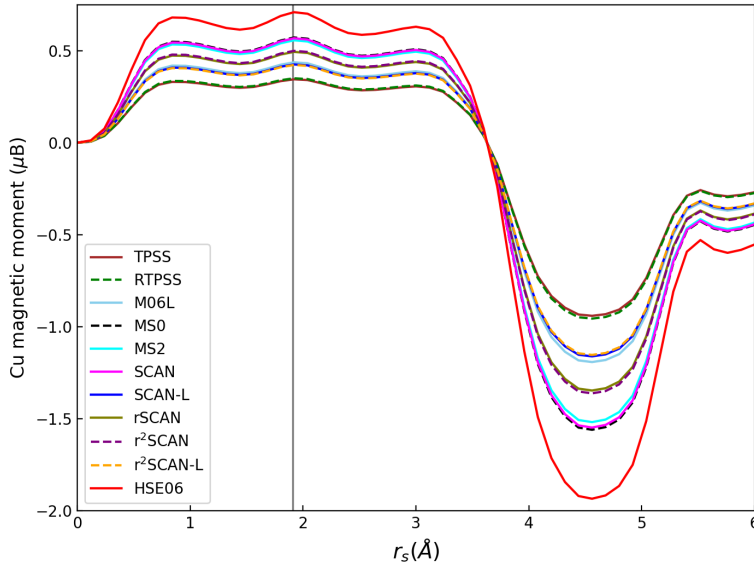
Figure 3.8: Copper magnetic moments of $La_2CuO_4$ in the LTO crystal structure by various functional approximations when Wigner-Seitz radius is varied. The vertical grey line represents Cu-O bond length.

gap in the cuprates. In contrast, the energy of the absorption peak in the optical spectrum depends on finer details of the electronic structure such as the presence of flat bands or Van Hove singularities. The theoretically predicted bandgaps here should be compared to the fundamental band gaps [143, 144, 145, 146], which are typically larger than the corresponding optical band gaps due to excitonic effects. Notably, a recent measurement on LCO reports an optical bandgap of about $\approx 1.3$ eV [5].

Regarding magnetic moments, the values obtained by neutron scattering involve uncertainties since the copper form factor is not *a priori* known. Appendix E of Ref.[116] compares copper magnetic moments from various experiments, including the values given in the recent review of Tranquada[7]. Note that, when estimating the copper magnetic moment, we computed the copper (Cu) magnetic moment by varying the Wigner-Seitz radius ($r_s$) beyond the default of 1.16 Å  to the value of 1.91 Å  (the Cu-O bond length) to fully capture the magnetic density centered on the Cu site and the part of the magnetic density originating from the strong hybridization between the copper and oxygen atoms. Cu magnetic moments as a function of the Wigner-Seitz radius based on using various functionals are shown in Figure 3.8: slightly enhanced magnetic moments are seen for all functionals when the overlap between the Cu and oxygen atoms is taken into account. At $r_s$ of 1.91 Å, we fully enclose the Cu site, resulting in the maximum positive magnetic moment ($S_0$) for all functional approximations. As $r_s$ increases further, the negative density from the tails of the first nearest-neighbor shell of 4 atoms start to contribute. At $r_s \sim 3.63$ Å, we approximately capture

1/4 of each nearest-neighbor site, yielding a moment of zero due to the staggered magnetization. For $r_s \sim$ 4.5 Å, the Wigner-Seitz sphere now fully encompasses the central atomic site and the first nearest-neighbor shell, producing a large negative value since $S = S_0 + 4S_{nn}$, where $S_{nn}$ is the magnetic moment value on the nearest-neighbor sites and $S_{nn} = -S_0$. Note that the Cu moment for large $r_s$ values will depend on the coordination number and thus on the crystal structure.

While these predicted magnetic moments are in approximate agreement with the experimentally measured value, it has been suggested that this is not the correct comparison. This is because 1) given a static magnetic moment, fluctuation can cause a 30% reduction [147]. 2) DFT works with spin symmetry breaking [148], and the DFT magnetic moments should be compared to the static value. We believe this issue is unresolved and that self-consistency can capture some average effects of fluctuation due to the DFT correlation potential. We hope to discuss this further in a future publication.

Figure 3.9 presents the electronic band dispersions in pristine and doped $La_2CuO_4$ in the LTO crystal structure for the AFM phase using SCAN, r²SCAN, r²SCAN-L, M06L, and HSE06. The copper (red circles) and planar oxygen (blue dots) orbital contributions are overlayed. For all XC functionals, LCO is seen to be an insulator. At the valence band edge, SCAN, r²SCAN and r²SCAN-L produce a significant avoided crossing between the $d_{x^2-y^2}$ and in-plane oxygen dominated bands along $\Gamma - M$ and $M - \bar{\Gamma}$, but this feature is essentially absent in M06L. In SCAN and r²SCAN, the gap is direct, with its smallest value occurring at M symmetry point or very close to it. In contrast, r²SCAN-L and M06L predict indirect bandgaps. Finally, the conduction bands in M06L display significant spin splittings indicative of ferrimagnetic ordering consistent with the observed ferrimagnetic moments.

Turning to the doped system in Fig.3.9, all meta-GGAs are seen to capture the metal-insulator transition, with various XC functionals producing small differences in band splittings around the Fermi level. In contrast, HSE06 maintains a small gap and predicts a nearly flat impurity-like band just above the Fermi level, consistent with the B3LYP results [109]. See Supplementary Materials for further details of the electronic band dispersions in LTO, LTT and HTT phases. The SCAN-based magnetic moments and bandgaps given in this study differ by $\sim 0.02$ $\mu_B$ and 0.11eV respectively, from those given in Ref.[3]. These small differences, which do not affect the overall conclusions of Ref.[3], are due to an error in the VASP implementation that was used in Ref. [3].

### 3.4.3 Effective U and exchange coupling

The band gap that develops in the half-filled Cu $d_{x^2-y^2}$ dominated band by splitting the up- and down-spin bands is due to strong multi-orbital intrasite electron-electron interactions. The strength of these interactions

is a key quantity that can be used to characterize various regions of the phase diagram and classify the phenomenology of the cuprate family as a whole[149]. In order to estimate the correlation strengths implicit in the underlying XC density functionals, we map our site-resolved partial densities of states to a multiorbital Hubbard model[150] along the lines of Ref. [116]. For this purpose, we consider a d orbital $\mu$ of spin $\sigma$ in a ligand field with on-site correlations in the mean field, and express its energy as

$$E_{\pm}^{\mu\sigma} = E_{\text{atomic}}^{\mu} + U\langle n_{\mu\bar{\sigma}}\rangle^{\pm} + U'\sum_{\nu\neq\mu}\langle n_{\nu\bar{\sigma}}\rangle^{\pm} + (U' - J_{\text{H}})\sum_{\nu\neq\mu}\langle n_{\nu\sigma}\rangle^{\pm} \pm h,$$

where $\pm$ indexes the bonding $(-)$ and antibonding $(+)$ states, and h is the hybridization strength. $\mu(\nu)$ and spin $\sigma(\bar{\sigma} = -\sigma)$ are orbital and spin indices, respectively, and $\langle n_{\mu\sigma}^{\pm}\rangle$ is the average electron occupation for a given state in the mean field. By taking the difference between the up- and down-spin channels and summing over bonding and anti-boding levels, U and $J_{\text{H}}$ can be shown to connect the spin splitting of a given orbital to the differences in various spin-dependent orbital occupations,

$$E^{\mu\uparrow} - E^{\mu\downarrow} = U(N_{\mu\downarrow} - N_{\mu\uparrow}) - J_{\text{H}}\sum_{\nu\neq\mu}(N_{\nu\uparrow} - N_{\nu\downarrow}), \tag{3.1}$$

where $N_{\mu\sigma} = \sum_{\pm}\langle n_{\mu\sigma}^{\pm}\rangle$. Furthermore, $E^{\mu\sigma}$ may be obtained from the density of states:

$$E^{\mu\sigma} = \int_{W} g_{\mu\sigma}(\varepsilon)\varepsilon d\varepsilon \tag{3.2}$$

where $W$ represents the bandwidth. The average spin splitting of a given orbital can then be expressed as:

$$E^{\mu\uparrow} - E^{\mu\downarrow} = \int_{W}[g_{\mu\uparrow}(\varepsilon) - g_{\mu\downarrow}(\varepsilon)]\varepsilon d\varepsilon. \tag{3.3}$$

We thus arrive at the following coupled set of equations for the interaction parameters,

$$\int_{W}[g_{\mu\uparrow}(\varepsilon) - g_{\mu\downarrow}(\varepsilon)]\varepsilon d\varepsilon = \tag{3.4}$$
$$U(N_{\mu\downarrow} - N_{\mu\uparrow}) - J_{\text{H}}\sum_{\nu\neq\mu}(N_{\nu\uparrow} - N_{\nu\downarrow}).$$

By using the copper-atom-projected partial density-of-states in the AFM phase of LTO La$_2$CuO$_4$ where the d$_{\text{x}^2-\text{y}^2}$ orbital is half-filled and all other orbitals are completely filled, we can simplify the preceding set

of coupled equations into the form:

$$\int_W [g_{d_{x^2-y^2}\uparrow}(\varepsilon) - g_{d_{x^2-y^2}\downarrow}(\varepsilon)]\varepsilon d\varepsilon = U/2 \tag{3.5}$$

$$\int_W [g_{(\mu \neq d_{x^2-y^2})\uparrow}(\varepsilon) - g_{(\mu \neq d_{x^2-y^2})\downarrow}(\varepsilon)]\varepsilon d\varepsilon = J_H/2 \tag{3.6}$$

Finally, we evaluate $\int_W [g_{\mu\uparrow}(\varepsilon) - g_{\mu\downarrow}(\varepsilon)]\varepsilon d\varepsilon$ over the full band width $W$ for each orbital to solve for U and $J_H$. The estimated values of U and $J_H$ so obtained are presented in Table 3.1. The average spin-splittings are strongly orbital dependent [116], and we have taken the largest value as the upper bound on $J_H$.

Table 3.1: Theoretically predicted values of U and $J_H$ using various DFAs for three different phases of pristine LCO.

| Functional | Phase | U (eV) | $J_H$ (eV) |
|---|---|---|---|
| | LTO | 2.23 | 0.54 |
| TPSS | LTT | 2.19 | 0.55 |
| | HTT | 2.19 | 0.54 |
| | LTO | 2.32 | 0.60 |
| revTPSS | LTT | 2.31 | 0.60 |
| | HTT | 2.3 | 0.58 |
| | LTO | 3.14 | 0.51 |
| M06L | LTT | 3.14 | 0.54 |
| | HTT | 3.19 | 0.55 |
| | LTO | 5.60 | 1.36 |
| MS0 | LTT | 5.71 | 1.32 |
| | HTT | 5.91 | 1.34 |
| | LTO | 5.00 | 1.16 |
| MS2 | LTT | 5.09 | 1.13 |
| | HTT | 5.108 | 1.18 |
| | LTO | 5.40 | 1.25 |
| SCAN | LTT | 5.40 | 1.27 |
| | HTT | 5.36 | 1.24 |
| | LTO | 3.13 | 0.61 |
| SCAN-L | LTT | 3.13 | 0.61 |
| | HTT | 3.16 | 0.60 |
| | LTO | 4.24 | 1.04 |
| rSCAN | LTT | 4.25 | 1.03 |
| | HTT | 4.26 | 1.02 |
| | LTO | 4.45 | 1.06 |
| r²SCAN | LTT | 4.43 | 1.06 |
| | HTT | 4.41 | 1.05 |
| | LTO | 3.14 | 0.61 |
| r²SCAN-L | LTT | 3.15 | 0.62 |
| | HTT | 3.16 | 0.61 |
| | LTO | 11.79 | 1.27 |
| HSE06 | LTT | 11.30 | 1.36 |
| | HTT | 11.58 | 1.27 |

Results of Table 3.1 show that TPSS and revTPSS yield a smaller value for U compared to the recent cRPA calculations ($\sim 3.2$ eV) [151], since they fail to adequately capture the bandgaps and magnetic moments, while M06L, SCAN-L and r$^2$SCAN-L yield comparable values. MS0,MS2, rSCAN and r$^2$SCAN, find larger values than the cRPA values. The hybrid HSE06 XC functional predicts exaggerated values for U.

In order to determine the exchange coupling strength, we use a mean-field approach, where we map the total energies of the AFM and ferromagnetic (FM) phases onto those of a nearest-neighbor spin$-\frac{1}{2}$ Heisenberg Hamiltonian [152, 153, 154]. The difference in the energies of the AFM and FM phases in the mean field limit is given by

$$\Delta E = E_{AFM} - E_{FM} = JNZ<S>^2 \tag{3.7}$$

where N is the total number of magnetic sites in the unit cell, S $=1/2$ is the spin on each site, and Z is the coordination number. Since the in-plane interactions within the Cu-O planes in La$_2$CuO$_4$ are much stronger than the interplanar interactions, we take Z = 4. For our AFM $\sqrt{2} \times \sqrt{2}$ unit cell, N = 4. In this way, we obtain the J values for various XC functionals listed in table 3.2.

Table 3.2 shows that SCAN is most accurate in predicting the experimental value of $-133 \pm 3$ meV [155, 156, 157] for the exchange coupling in LCO. MS0 and MS2 slightly overestimate J compared to SCAN. TPSS, revTPSS, SCAN-L, rSCAN, r$^2$SCAN and r$^2$SCAN-L underestimate and HSE06 significantly overestimates J. M06L failed to converge for the FM case. Notably, here and in Ref. [116],our modeling involves only the nearest-neighbor J in keeping with the related experimental analysis. We would expect some renormalization of the J values if we were to include next and higher nearest neighbors in our modeling.

In order to gain further insight into the multiorbital nature of the electronic structure, two additional descriptors were estimated: (1) Charge-transfer energies between the Cu 3d and O 2p orbitals ($\Delta_{dp}$); and (2) the tetragonal splitting of the e$_g$ states ($\Delta_{e_g}$), which are defined as

$$\Delta_{dp} = \varepsilon_d - \varepsilon_p \tag{3.8}$$

and

$$\Delta_{e_g} = \varepsilon_{x^2-y^2} - \varepsilon_{z^2}. \tag{3.9}$$

The various band centers $\varepsilon_\mu$ are defined using the corresponding partial density-of-states as

$$\varepsilon_\mu = \frac{\int g_\mu(\varepsilon)\varepsilon d\varepsilon}{\int g_\mu(\varepsilon)d\varepsilon}, \tag{3.10}$$

along the lines of Refs.[158] and [159]. We used an integration window of $-8$ eV to the top of the band in

Table 3.2: Theoretically predicted values of exchange coupling using various XC functionals for three different phases of pristine LCO.

| Functional | Phase | J (meV) |
|---|---|---|
| TPSS | LTO | -26.74 |
| | LTT | -25.9 |
| | HTT | -22.24 |
| revTPSS | LTO | -26.89 |
| | LTT | -27.47 |
| | HTT | -24.74 |
| M06L | did not converge | - |
| MS0 | LTO | -158.29 |
| | LTT | -159.36 |
| | HTT | -160.75 |
| MS2 | LTO | -140.46 |
| | LTT | -141.76 |
| | HTT | -139.94 |
| SCAN | LTO | -131.08 |
| | LTT | -131.32 |
| | HTT | -125.97 |
| SCAN-L | LTO | -48.48 |
| | LTT | -50.62 |
| | HTT | -49.95 |
| rSCAN | LTO | -87.16 |
| | LTT | -88.37 |
| | HTT | -82.09 |
| r$^2$SCAN | LTO | -93.12 |
| | LTT | -95.04 |
| | HTT | -88.33 |
| r$^2$SCAN-L | LTO | -49.01 |
| | LTT | -50.61 |
| | HTT | -49.88 |
| HSE06 | LTO | -182.11 |
| | LTT | -188.51 |
| | HTT | -180.27 |

Eq.3.10. This window covers only the anti-bonding bands for $\Delta_{e_g}$. Results of Table 3.3 show that compared to PBE, the meta-GGAs generally tend to enhance $\Delta_{dp}$ and $\Delta_{e_g}$ due to the stabilization of the AFM order. TPSS and revTPSS performances are comparable to PBE while other meta-GGAs predict larger $\Delta_{dp}$ and $\Delta_{e_g}$ values. For the doped case, $\Delta_{dp}$ increases, whereas $\Delta_{e_g}$ reduces compared to the pristine results. HSE06 predicts significantly large $\Delta_{dp}$ and $\Delta_{e_g}$ for both pristine and doped cases.

### 3.4.4 Meta-GGA performance discussion

The present results for the crystal, electronic, and magnetic properties clearly demonstrate that meta-GGAs provide an improvement over LSDA and PBE. Among the various meta-GGAs considered (TPSS, revTPSS,

Table 3.3: Theoretically predicted values of the charge-transfer energies between Cu 3d and O 2p orbitals and two Cu energy splitting using various XC functionals for three different phases of pristine LCO and doped LSCO systems

| Functional | Phase | pristine LCO | | doped LSCO | |
|---|---|---|---|---|---|
| | | $\Delta_{\mathrm{dp}}$(eV) | $\Delta_{\mathrm{e_g}}$(eV) | $\Delta_{\mathrm{dp}}$(eV) | $\Delta_{\mathrm{e_g}}$(eV) |
| PBE | LTO | 2.41 | 0.74 | 3.49 | 0.60 |
| | LTT | 2.38 | 0.75 | 3.30 | 0.62 |
| | HTT | 2.41 | 0.79 | 3.46 | 0.59 |
| TPSS | LTO | 2.41 | 0.77 | 3.52 | 0.62 |
| | LTT | 2.23 | 0.78 | 3.50 | 0.63 |
| | HTT | 2.26 | 0.80 | 3.44 | 0.63 |
| revTPSS | LTO | 2.37 | 0.77 | 3.50 | 0.61 |
| | LTT | 2.24 | 0.78 | 3.49 | 0.62 |
| | HTT | 2.23 | 0.80 | 3.46 | 0.63 |
| M06L | LTO | 2.52 | 1.00 | 3.95 | 0.73 |
| | LTT | 2.54 | 1.06 | 3.91 | 0.74 |
| | HTT | 2.46 | 1.07 | 3.75 | 0.81 |
| MS0 | LTO | 2.99 | 1.34 | 5.00 | 1.07 |
| | LTT | 2.84 | 1.37 | 4.75 | 1.14 |
| | HTT | 2.93 | 1.35 | 5.16 | 1.09 |
| MS2 | LTO | 3.00 | 1.21 | 4.76 | 0.89 |
| | LTT | 2.91 | 1.22 | 4.97 | 0.87 |
| | HTT | 2.92 | 1.20 | 4.66 | 0.93 |
| SCAN | LTO | 3.01 | 1.23 | 4.84 | 0.95 |
| | LTT | 2.93 | 1.24 | 4.79 | 0.95 |
| | HTT | 2.92 | 1.24 | 4.71 | 0.96 |
| SCAN-L | LTO | 2.64 | 0.96 | 4.18 | 0.72 |
| | LTT | 2.54 | 0.96 | 4.20 | 0.72 |
| | HTT | 2.49 | 0.95 | 3.89 | 0.80 |
| rSCAN | LTO | 2.55 | 1.06 | 4.17 | 0.92 |
| | LTT | 2.45 | 1.08 | 4.18 | 0.92 |
| | HTT | 2.47 | 1.12 | 4.1 | 0.93 |
| r$^2$SCAN | LTO | 2.52 | 1.08 | 4.19 | 0.92 |
| | LTT | 2.45 | 1.09 | 4.22 | 0.93 |
| | HTT | 2.47 | 1.13 | 4.15 | 0.93 |
| r$^2$SCAN-L | LTO | 2.65 | 0.98 | 4.18 | 0.73 |
| | LTT | 2.55 | 0.98 | 4.21 | 0.74 |
| | HTT | 2.46 | 0.96 | 3.91 | 0.83 |
| HSE06 | LTO | 7.35 | 2.76 | 9.89 | 2.80 |
| | LTT | 6.91 | 2.82 | - | - |
| | HTT | 7.15 | 2.74 | - | - |

MS0, MS2, SCAN, rSCAN, r$^2$SCAN, M06L), M06L is less satisfactory for predicting the LCO properties, which is heavily parameterized for molecular systems. The earlier generalized-KS (gKS) meta-GGAs such as TPSS and revTPSS are less accurate than the more recently developed approximations (e.g. SCAN). The success of SCAN is a consequence of its enforcing all the known 17 rigorous constraints that a semilocal functional can satisfy[12]. In addition, SCAN localizes d electrons better by reducing self-interaction errors

that tend to over-delocalize d electrons in the presence of ligands involving s and p electrons[146]. SCAN thus stabilizes the magnetic moment of Cu and opens a sizable bandgap in LCO[3], its shortcomings in exaggerating magnetic moments in 3d elemental solids notwithstanding [119].

rSCAN solves the numerical grid issues encountered in SCAN by regularizing the problematic interpolation function of SCAN with a smooth polynomial, which unfortunately violates exact constraints [123, 79], and some of rSCAN's tranferability is lost [86, 85]. r$^2$SCAN retains the smoothness of rSCAN and maximally restores the exact constraints violated by the regularization of rSCAN and it has been shown to improve the accuracy over rSCAN while maintaining the numerical efficiency[79]. In the present study of cuprates, r$^2$SCAN and rSCAN both perform similarly, with only slight underestimations of the band gaps and magnetic moments.

By replacing the kinetic energy density with the Laplacian of the electron density and thus de-orbitalizing the underlying meta-GGAs, SCAN-L [93] and r$^2$SCAN-L [94] are constructed from SCAN and r$^2$SCAN, respectively. The XC potentials in SCAN-L and r$^2$SCAN-L are locally multiplicative while in their orbital dependent parent functionals, the potentials are nonmultiplicative. Perdew *et al.*[145] have shown that for a given DFA, the gKS orbital band gap is equal to the corresponding fundamental band gap in solids, which is defined as the second order ground-state energy difference with respect to electron number. This indicates that within the gKS formalism a DFA with better total energy also improves the band gap [146]. The preceding statement also applies to DFAs with multiplicative potentials as they have the same potentials in the KS and gKS schemes. The bandgaps and copper magnetic moments from SCAN-L and r$^2$SCAN-L are consistently underestimated compared to the corresponding values from the parent SCAN and r$^2$SCAN XC functionals.

M06L being an empirical functional is heavily parametrized. It is constructed by fitting to molecular data sets, and therefore, it tends to be less reliable for systems outside its fitting set with limited transferability.

### 3.4.5  Why does HSE06 open a gap in the doped LSCO?

HSE06 with the admixing parameter value of 1/4 works well for bandgap predictions in semiconductors. This improvement is due to the reduction of the self-interaction error present in PBE through the introduction of exact exchange [144, 146]. However, Hartree-Fock is not applicable to metallic systems where there is no bandgap to separate the occupied and unoccupied bands. Therefore, hybrid functionals are not suited for metallic systems.

With the preceding consideration in mind, it is reasonable that the HSE06 XC functional produces an insulator in LCO but fails to capture the metal-insulator transition under doping. Figure 3.10 shows HSE06

based band structures of LSCO for various mixing parameters "$a$". For $a = 0$, HSE06 is reduced to PBE, and thus predicts LSCO to be metallic. At $a = 0.05$, a slight change in the band structure can be seen: the conduction bands are slightly pushed up and split due to the stabilization of the magnetic moments on Cu, and the bands around the Fermi level at $X$ start to separate from one another. Increasing $a$ to 0.15 results in a separation of the valence bands at the Fermi level and the splitting of the conduction bands, and the two valence bands near the Fermi level split off from the remaining valence bands. Finally, at the standard value of $a = 0.25$, the highest valence band completely splits off, leaving a 0.2 eV gap at the Fermi level.

The resulting conduction band displays significant spin-splitting, indicative of a strong uncompensated ferri-magnetic order. Our spin density calculations show that the spin-down band now lies just above the Fermi level where the doped hole is localized in the copper $d_{z^2}$ and apical-oxygen $p_z$ hybridized band, see in Figure S5(a) of the Supplementary Material. Moreover, the band-projected charge density for the spin-down band (Supplementary Figure S5(b)) clearly displays a $d_{z^2}$ orbital shape for copper sites and a $p_z$ orbital shape on the apical oxygen sites, similar to the results from B3LYP [109].

Band structures of fig. 3.10 show that for small values of the mixing parameter ($a$), the conduction band and valence bands around the M point near the Fermi level are more dominated by copper $d_{x^2-y^2}$ states. As the value of the mixing parameter increases, the copper $d_{z^2}$ orbitals gain more weight. This implies that, as the fraction of exact exchange increases, electrons are more localized on in-plane copper atoms. This is expected since the LSDA gives the extreme covalent regime while the Hartree-Fock leads to the extreme ionicity.

## 3.5    Conclusion

Our study demonstrates that the meta-GGA class of XC functionals within the generalized Kohn-Sham scheme correctly predict many experimental results for pristine LCO, and also capture the insulator-to-metal transition with Sr doping. Among the different meta-GGAs considered, SCAN's performance for structural, electronic, and magnetic properties of LCO/LSCO is closest to the corresponding experimental results. In contrast, the hybrid XC functional (HSE06) fails to capture the metal-insulator transition and overestimates the magnetic moments and bandgaps in pristine LCO, and it needs adjustment of the standard 25% value of the mixing parameter to produce the metallic states. Our study thus indicates that the meta-GGAs provide a robust new pathway for the first-principles treatment of strongly correlated materials.
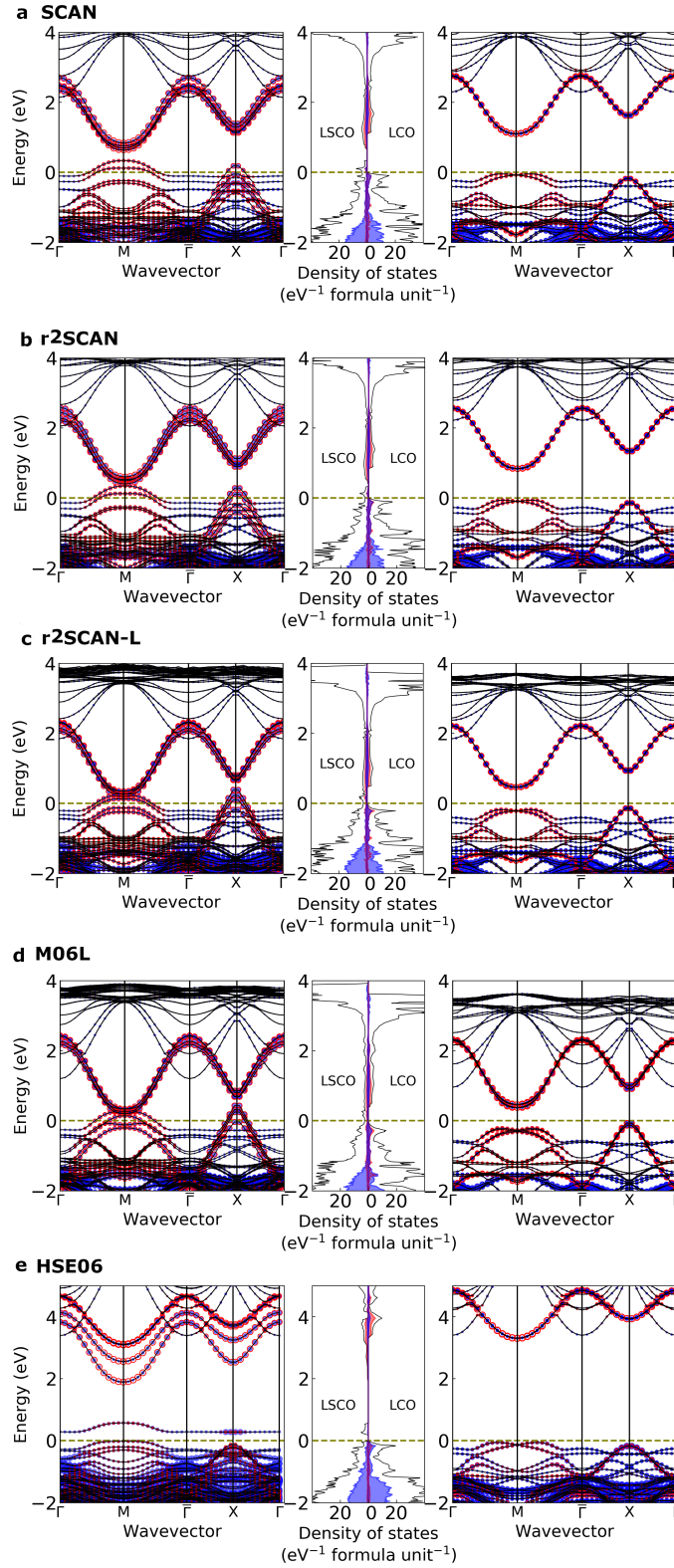
Figure 3.9: Electronic band structure and density of states of LCO and LSCO in the LTO phase using (**a**) SCAN (**b**) $r^2$SCAN (**c**) $r^2$SCAN-L (**d**) M06L (**e**) HSE06. The contribution of Cu-$d_{x^2-y^2}$ and O -$p_x + p_y$ are marked by the red and blues shadings, respectively. The path followed by the dispersion in the Brillouin zone is shown in Fig 3.3(**b**).
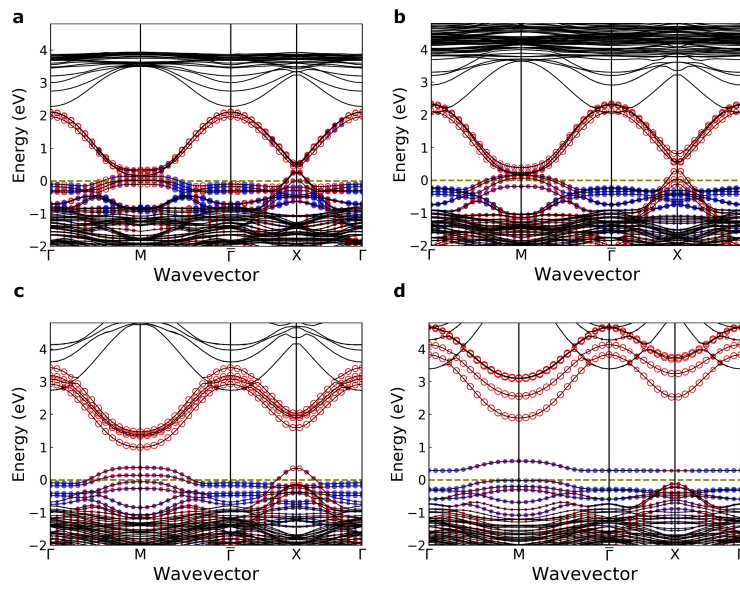
Figure 3.10: Band structure comparison by varying mixing parameter in the HSE06 hybrid functional for (**a**) $a = 0$ (**b**) $a = 0.05$ (**c**) $a = 0.15$ and (**d**) $a = 0.25$ in doped LTO phase. The blue filled and red empty circles correspond to copper $d_{z^2}$ and copper $d_{x^2-y^2}$ orbitals respectively. The projection strength is denoted by marker size.

# Chapter 4

# Transition metal compounds

## 4.1 Introduction/Motivation

Transition metal (TM) compounds are a unique class of solids whose physics is extremely rich. These are metals, large-gap insulators, and also systems that exhibit metal-insulator transitions. The magnetic properties of these systems are also diverse as most strong magnets are TM compounds. The high-$T_c$ superconductors also falls in this category [160]. Because of these unusual properties, the TM compounds fall in the category of enigmatic systems.

The early studies of late $3d$ transition-metal monoxides (MnO, FeO, CoO, and NiO) incorrectly predicted them to be metallic, contrasting the experimental result as an insulator [161]. This led to the general concept that mean-field approaches are inappropriate for predicting the electronic structure of these materials and inter-electronic interaction $U$ is required to open a band gap between the occupied and unoccupied degenerate states while retaining symmetry[146]. Recently however, it has been shown that this concept of Mott insulators in fact, is not needed for the $3d$ binary oxides MnO, FeO, CoO, and NiO and that the mean-field band theory can indeed open a band gap without an on-site inter-electronic interaction $U$. This has been achieved with polymorphous representation of the unit cell in conjunction with a recently developed non-empirical exchange-correlation (XC) density-functional (SCAN) [146]. In addition, SCAN has been shown to accurately predict many key properties of correlated materials, with the likes of the pristine and doped $La_2CuO_4$(LCO) and $YBa_2Cu_3O_6$ [3, 116, 162, 117]. In LCO, SCAN correctly captures the size of optical band gap, the magnitude and the orientation of the copper magnetic moment, and the magnetic form factor in comparison with the corresponding experimental results [116]. In near-optimally doped $YBa_2Cu_3O_7$, 26 competing uniform and stripe phases are identified [117]. Furthermore, SCAN has been applied to the

$Sr_2IrO_4$ parent compound yielding the subtle balance between electron correlations and strong spin-orbit coupling in excellent agreement with experiment[118].

SCAN's success in $3d$ TM compounds is a significant achievement for the DFT and suggests capability for treating a wider class of correlated materials. A number of natural questions therefore arise: Is SCAN a unique XC density functional that is able to correctly capture a variety of properties of $3d$ TM compounds or do other meta-GGAs perform similarly well? To answer these questions, we compare the accuracy of 11 DFAs, LSDA[124, 68], PBE[32], TPSS[56], revTPSS[58], MS0[60], MS2[61], SCAN[12], SCAN-L[93], rSCAN[123], r²SCAN[163], r²SCAN-L[94]. The performance of these functionals on the band gap and magnetic moment are listed in Table 4.1 while the band gap plots are shown in figures 4.1,4.2,4.3, and 4.4.

### 4.1.1 Result

Results from Table 4.1 shows that LSDA, in general, performs poorly for all four TM compounds, for both band gap and magnetic moment. PBE tends to improve over LSDA while for meta-GGAs, we observe mixed performances. The earlier meta-GGAs such as TPSS and revTPSS are less accurate than the more recently developed approximations (e.g. SCAN). Especially for FeO, they fail to open the band gap. MS0 is found to predict band gap and magnetic moment values closest to experimental result for almost all four systems, followed by SCAN. The other SCAN family functionals (rSCAN and r²SCAN) perform similarly with a slight underestimated values compared to SCAN. The laplacian dependent meta-GGAs (SCAN-L and r²SCAN-L) show performances either comparable to TPSS and revTPSS or only slightly better. One important thing to note here is that the band gap produced by all meta-GGAs are significantly reduced compared to the experimental values. Having said that, when compared to PBE density functional, which predicts metallic behavior, the gap opening is a remarkable step forward. The significant underestimation of band gap from recently developed approximations like SCAN is likely due to the residual self interaction error(SIE)[146]. Compared to band gap, the magnetic moments are found to be more closer to the experimental values for all meta-GGAs.
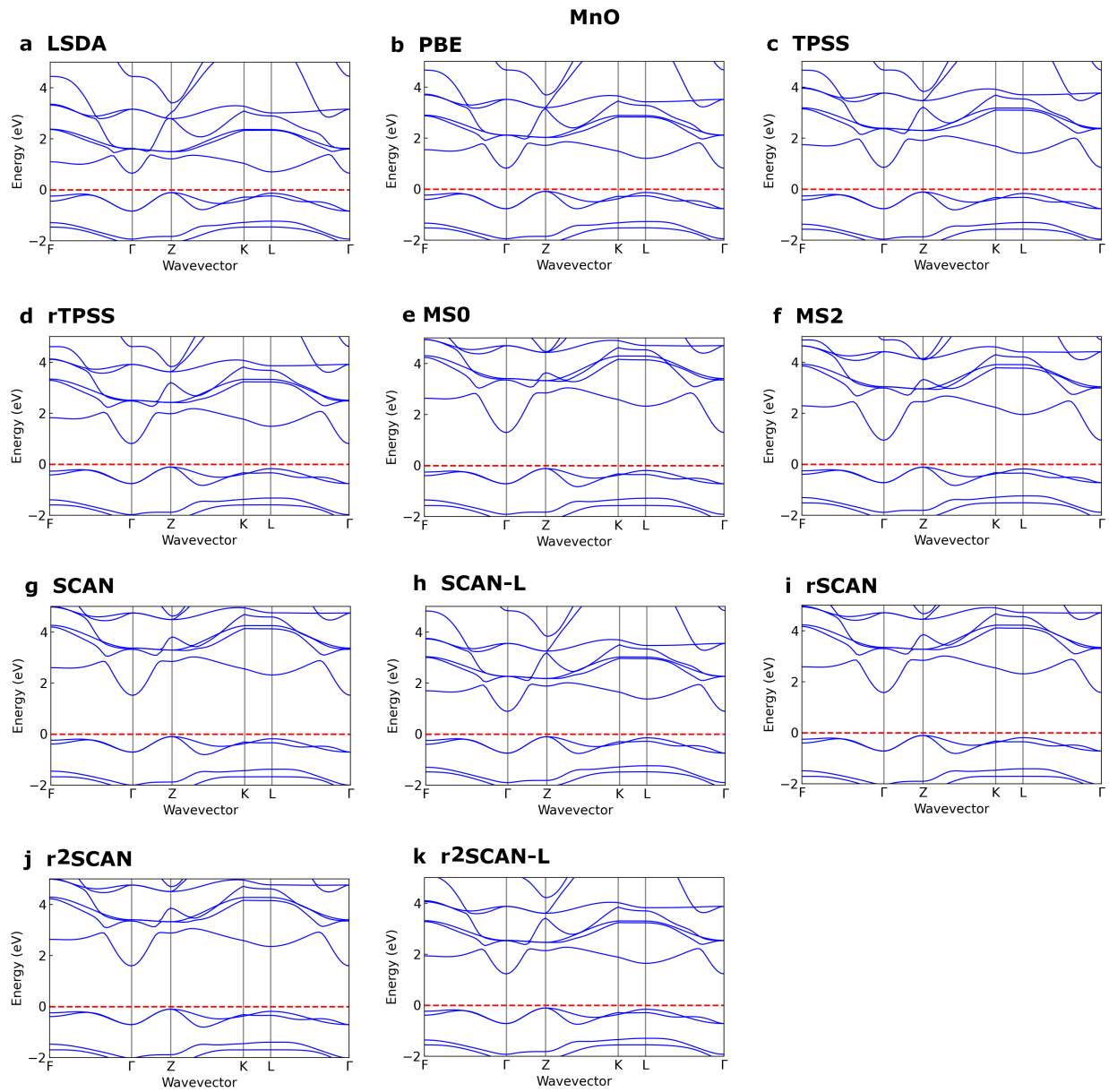
Figure 4.1: Band structure plot for MnO from the various DFAs considered.
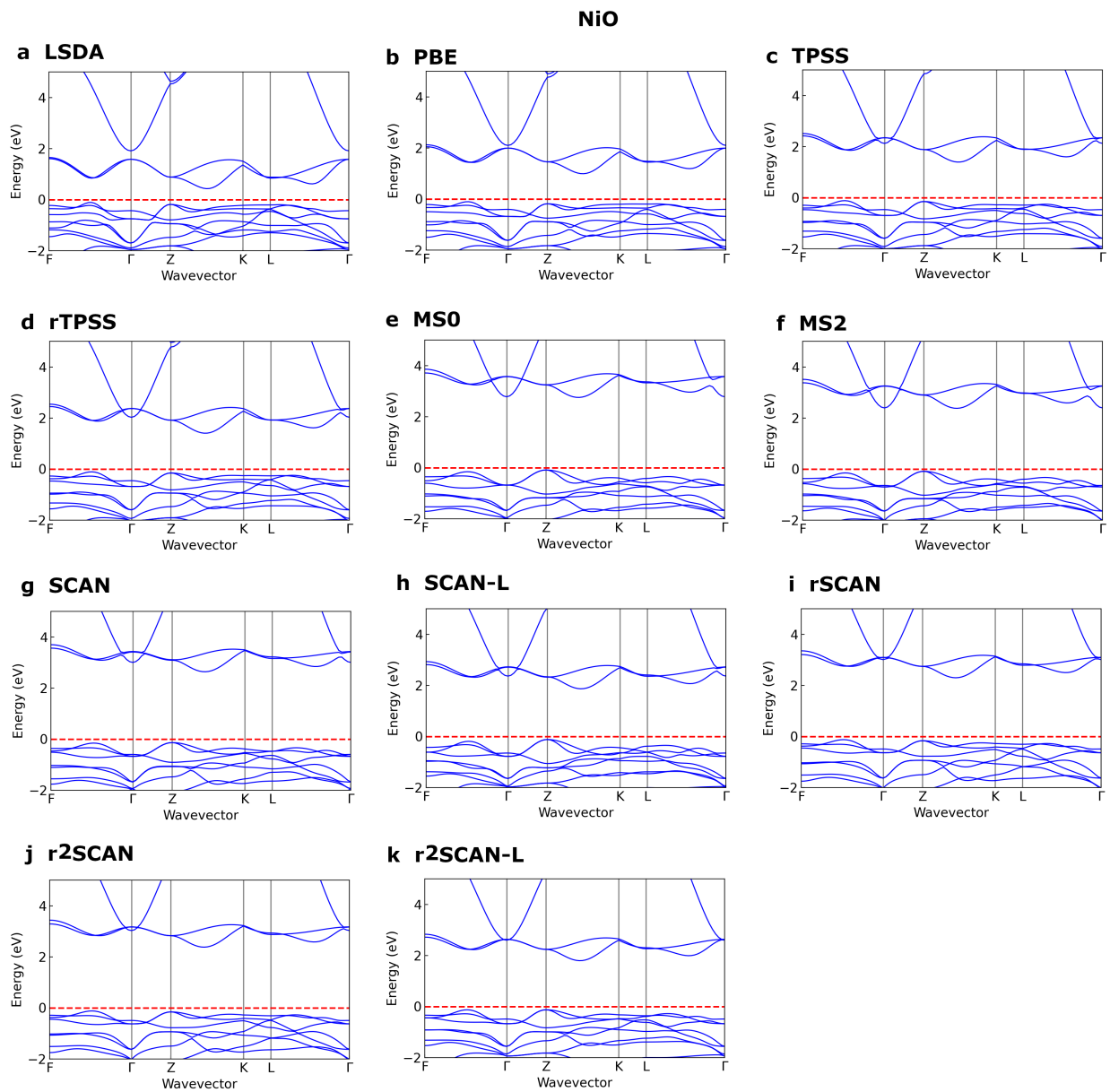
Figure 4.2: Band structure plot for NiO from the various DFAs considered.

**FeO**
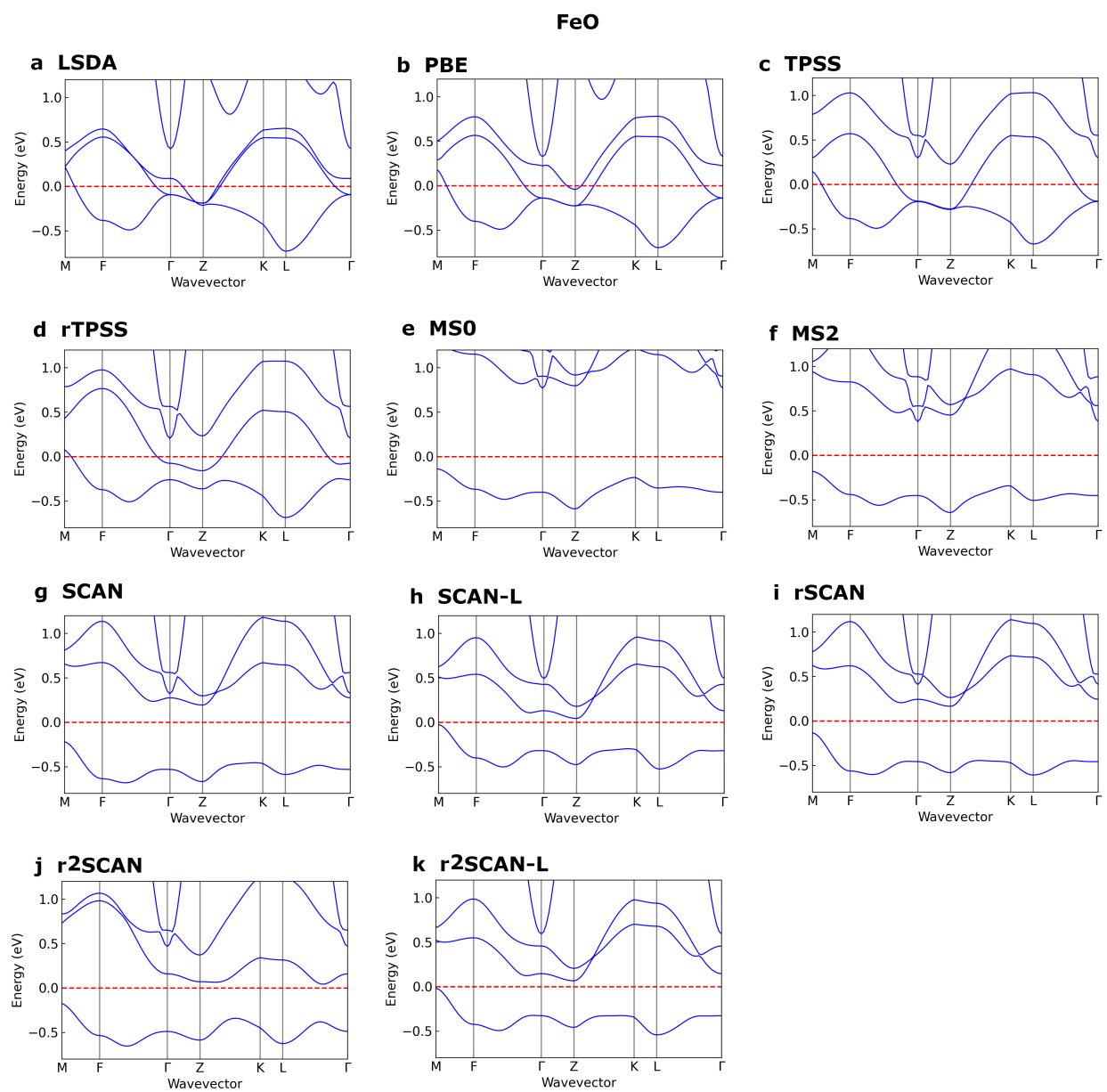


Figure 4.3: Band structure plot for FeO from the various DFAs considered.

**CoO**
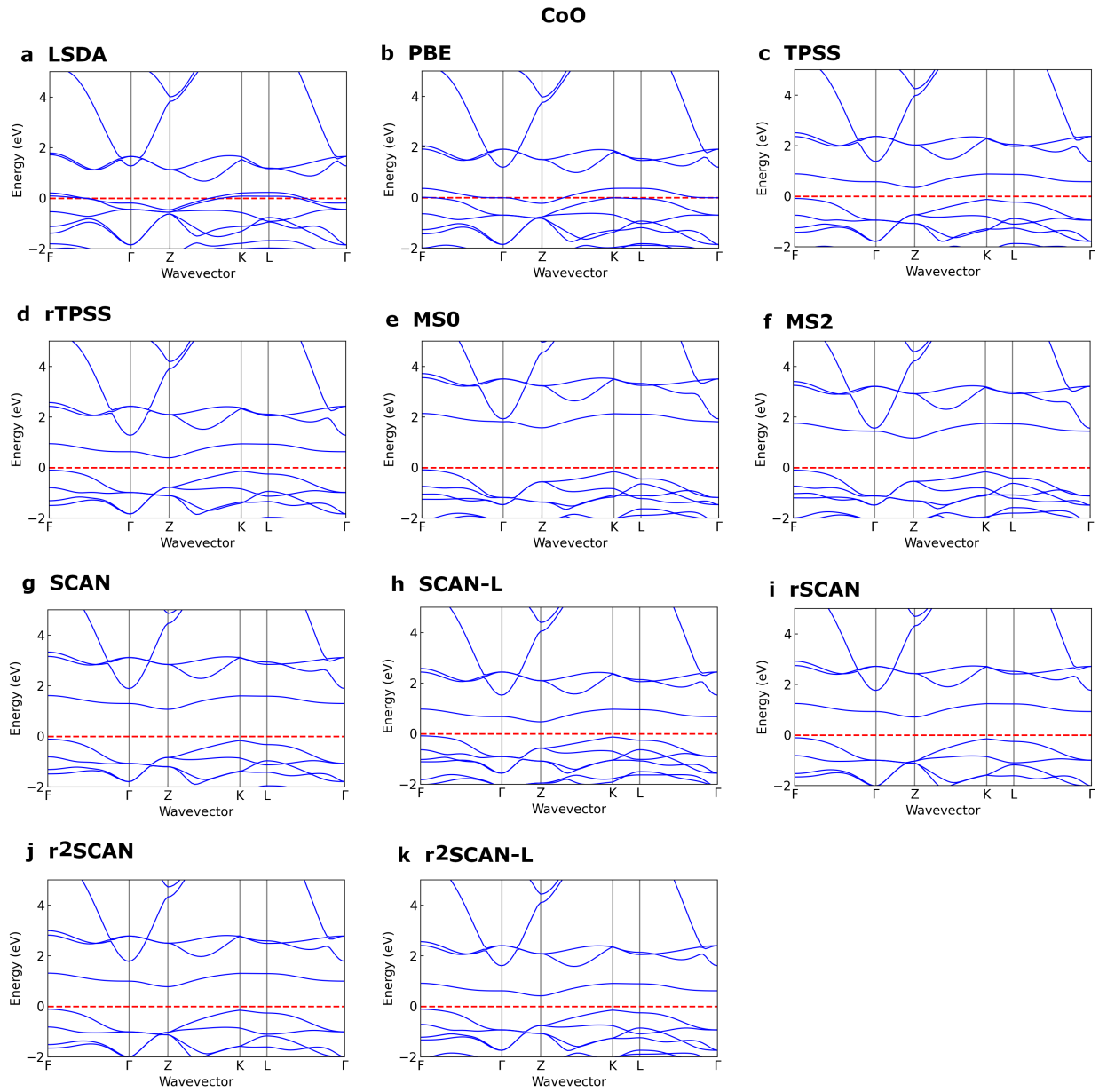


Figure 4.4: Band structure plot for CoO from the various DFAs considered.

Table 4.1: Band gaps, and local magnetic moments of four $3d$ monoxides in the G-type AFM phase calculated by various DFAs without $U$

| Functional | Band gap (eV) | | | | Magnetic moment ($\mu$B) | | | |
|:---:|:---:|:---:|:---:|:---:|:---:|:---:|:---:|:---:|
| | MnO | NiO | FeO | CoO | MnO | NiO | FeO | CoO |
| Expt. | 3.5[164] | 3.5[164] | 2.1[164] | 2.8[164] | 4.58[165] | 1.90[165] | 4.0[165] | 3.8~3.98[165] |
| LSDA | 0.75 | 0.47 | - | - | 4.23 | 1.15 | 3.36 | 2.33 |
| PBE | 0.90 | 1.02 | - | - | 4.32 | 1.36 | 3.44 | 2.43 |
| TPSS | 0.96 | 1.42 | - | 0.43 | 4.37 | 1.45 | 3.49 | 2.52 |
| revTPSS | 0.91 | 1.42 | - | 0.48 | 4.39 | 1.45 | 3.5 | 2.54 |
| MS0 | 1.40 | 2.76 | 0.87 | 1.65 | 4.47 | 1.61 | 3.55 | 2.61 |
| MS2 | 1.05 | 2.38 | 0.56 | 1.26 | 4.43 | 1.58 | 3.52 | 2.58 |
| SCAN | 1.61 | 2.67 | 0.38 | 1.17 | 4.44 | 1.59 | 3.55 | 2.58 |
| SCAN-L | 0.98 | 1.90 | 0.06 | 0.55 | 4.35 | 1.51 | 3.45 | 2.49 |
| rSCAN | 1.67 | 2.33 | 0.29 | 0.81 | 4.45 | 1.57 | 3.55 | 2.57 |
| r$^2$SCAN | 1.69 | 2.40 | 0.21 | 0.88 | 4.45 | 1.58 | 3.56 | 2.58 |
| r$^2$SCAN-L | 1.33 | 1.82 | 0.08 | 0.52 | 4.41 | 1.51 | 3.49 | 2.51 |

## 4.2 Why meta-GGA improves over GGA?

The improvement of meta-GGAs and especially SCAN over PBE for transition metal oxides [146] and f-electron compounds has been understood as a consequence of following three factors:

### 4.2.1 tau dependence

In addition to the electron density and its gradient used as ingredients in PBE, SCAN is also dependent on the non-interacting kinetic energy density, $\tau$. The kinetic energy density is a semilocal quantity built from the occupied orbitals immediately available in DFT calculations. By correctly building the kinetic energy density into a dimensionless orbital-overlap indicator, SCAN distinguishes between density regions characterizing different chemical bonds (including covalent, ionic, metallic, hydrogen, and van der Waals bonds) and treats them properly through appropriate GGA constructions, allowing SCAN to address diverse types of bonding in materials and systematically improving over PBE in general[122, 61, 34]. In addition, it also allows SCAN to satisfy exact constraints that are mutually exclusive for functionals at the GGA level, such as PBE.

### 4.2.2 generalized Kohn–Sham (gKS) scheme

$\tau$ is an orbital-dependent non-local functional of the electron density. This orbital dependence means $\tau$-dependent meta-GGAs, such as SCAN, are typically implemented in the gKS formalism in which the XC potential is an orbital dependent operator, rather than multiplicative. It has been shown that within this generalized framework the frontier orbitals have a well defined physical interpretation, and consequently the

band gaps predicted by gKS calculations have a strong physical connection to the experimentally measured fundamental gap [145, 146].

The fundamental band gap is defined as $E_g = I - A$, where $I$ is the ionization energy, and $A$ is the electron affinity. Since, $I$ and $A$ are ground-state energy differences, this fundamental band gap in principle, can be calculated exactly from DFT. Similarly, the band gap from Kohn-Sham (KS) or gKS DFT calculations can be obtained as $\epsilon^{CBM} - \epsilon^{VBM}$ where CBM and VBM stand for conduction band minimum and and valence band maximum. As the XC potential in KS scheme is multiplicative, the exact KS potential jumps by an additive-constant discontinuity as an electron is added to neutral solids [145]. This derivative discontinuity is found missing in LSDA and in GGA(PBE), which should be added to the KS band gap for the correct prediction of the fundamental band gap [166], certifying the underestimated band gaps predicted for four monoxide in the AFM phase shown in table 4.1. In gKS scheme on the other hand, the effective potential is not a multiplication operator but is in practice continuous. The earlier works [143, 144, 145] have also shown that $\epsilon^{CBM} - \epsilon^{VBM}$ band gap for a solid is equal to the fundamental band gap if the gKS potential operator is continuous and when an electron or hole is added, the density change is delocalized. The above work imply that any functional that improves the total energies, must also improve the orbital band gaps. As the recent meta-GGA SCAN is implemented in the gKS scheme, there is no derivative discontinuity in its effective potential, and therefore consistently opens the band gap in the four monoxides considered.

### 4.2.3 Self interaction error (SIE)

The construction of most approximate XC functionals leads to basic flaws. One such flaws is the self-interaction error[167], which comes from the residual interaction of an electron with itself. The error appears because the self-interaction of the approximate XC functional $E_{xc}$ and that of the Coulomb functional do not cancel completely in the density functional scheme, as they do in Hartree-Fock. Since the repulsive self-Coulomb exceeds the attractive self exchange correlation, the net SIE is generally positive [146] causing electrons to delocalize between nuclear centers. Such delocalized orbitals are far from observing symmetry breaking and hence underestimate the fundamental band gap [146].

The self-interaction correction (SIC) which is referred to as the reduction in the delocalization error is important in improving the band gap prediction. For orbital dependent density functionals implemented in gKS scheme with symmetry breaking, the lower the delocalization error, the better is the band gap prediction. The Perdew-Zunger (PZ) SIC which uses an effective $U$ to reduce SIE is found to be have an improved band gap values for binary and $ABO_3$ $3d$ oxides. [104]. In this regard, compared to PBE, SCAN reduces the amount of SIE [146, 168] and as result, consistently opens the band gap for the four TM compounds considered. This

minimization of SIE is especially important[146] for the open-shell $d$- and $f$-electron compounds.

## 4.3 Challenges for meta-GGA functionals

### 4.3.1 Self-interaction error

The SIC seems to have reduced the delocalization error in recent meta-GGAs, suggested by the consistent band gap opening by SCAN. However, the band gap predicted by meta-GGAs is significantly reduced compared to the experimental values, suggesting a further need to overcome SIE. Resolving SIE in a true first-principle spirit requires the necessity for nonlocal corrections [169, 170], which are computationally expensive and, at the same time, scale poorly with system size. Pederson and co-workers extended the PZ SIC to make the SIC computationally efficient by constructing size-extensive SIC orbitals.[170]. Yang and his collaborators presented a promising route to the first-principles approach for correcting SIE efficiently but is limited to its availability to solids [171].

The other approach is to use PZ SIC to meta-GGA, as Shahi and his collaborators did with SCAN functional [172]. They found that using PZ SIC with SCAN removes SIE seen primarily for stretched bonds but introduces other errors like orbital-density nodality errors[172]. The following alternative to effectively reduce SIE is the use of DFT+$U$ [173]. This method penalizes the $d$-electron delocalization and effectively reduces semilocal functionals' SIE. However, this approach seems to be more like an empirical one as the $U$ value depends upon systems and properties to be studied [168]. In addition, this is not considered as the first-principles basis and is looked as "beyond DFT" methodology.

# Chapter 5

# Exact constraints and appropriate norms in machine learned exchange-correlation functionals

## 5.1 Artificial neural network

### 5.1.1 Introduction

Inspired by the nervous system, the artificial neural network is a machine-learned prediction algorithm. An artificial neural network consists of neurons, a connecting topology, and a learning algorithm. The neurons are called units. A typical unit is shown in the figure 5.1. The input signals $(x_1, x_2, .....x_m)$ either comes from the external environment or outputs from the other units in the network. With each input are weights associated which have adjustable values that are to be learned. There is also an activation function that acts as a trigger which fires the neuron when the necessary condition is satisfied.
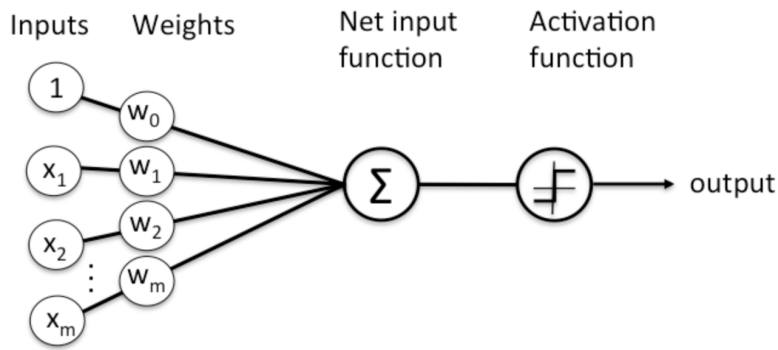
Figure 5.1: Single perceptron unit

The figure above represents a perceptron. Perceptron takes vectors of real-valued inputs, calculates the linear combination of inputs along with the weights associated and produces output as 1 if the result is greater than a certain threshold and produces -1 otherwise. We can imagine perceptron as hyperplane surface for which 1 lies at one end and -1 at the other end. The output for the perceptron is obtained as

$$o(x_1, x_2, ......x_m) = \begin{cases} 1, & \text{if } w_0 + w_1x_1 + w_2x_2 + ..... + w_mx_m > 0 \\ -1, & \text{otherwise} \end{cases} \tag{5.1}$$

where $w_i$ are weights, $w_0$ the bias. Learning a perceptron means that the correct values of these weights are to be obtained. Even though s single perceptron is building block of neural network, it alone is insufficient to express the system and hence a need for the multilayer networks of threshold units.

### 5.1.2 Multilayer perceptron network
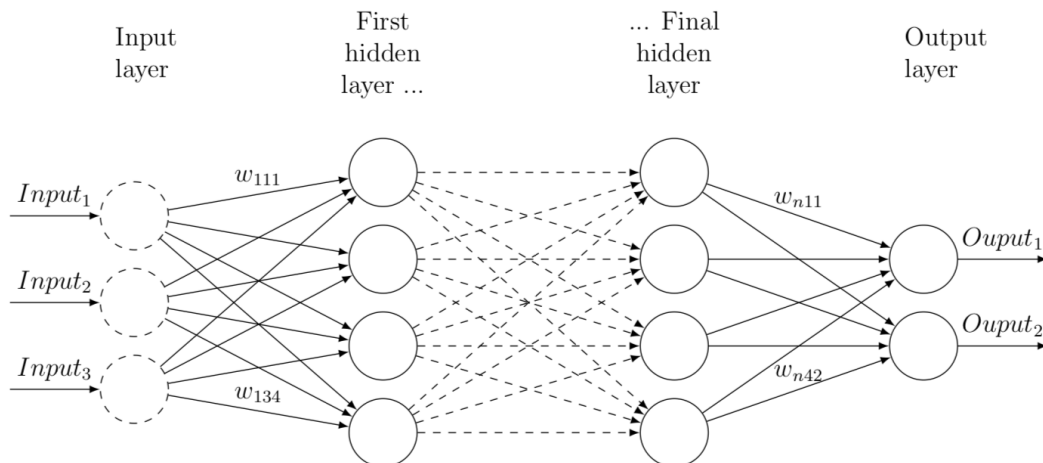


Figure 5.2: Multilayer neural network

The figure 5.2 represents a multi layer perceptron network or also termed as deep neural network. A neural network (NN) with more than one hidden layer is called as deep network. As is shown in the figure, the hidden layers can be of any number depending up on the data as well as the design per individual. The working mechanism is similar to a single perceptron but the activation function can vary from using sigmoid, hyper tangent, RELU or any other. The only motive of using different activation function is to induce more non linearity and the model becomes more expressive. The other important aspect of multilayer perceptron network is the back propagation algorithm used for learning the weights. It employs gradient descent to minimize the squared error between network output and target values for these outputs. Unlike feed forward network, in back propagation algorithm, the errors are propagated backward through the network. One of the challenges of back propagation algorithms is that through gradient descent, the weights have tendency to acquire local minima rather than global minima which can induce error. Despite this problem, back propagation algorithm has been found to produce excellent result in many real world applications.

### 5.1.3 Activation function

Different activation functions are used to induce more non linearity and the model becomes more expressive. The most commonly used activation functions were the logistic function and other sigmoid functions. Sigmoid refers to "S"-shaped functions, for example the hyperbolic tangent (tanh). More recently, Nair et al.[174] introduced the rectified linear unit (ReLU), a neuron with an activation function that is linear for positive inputs and zero for negative inputs. Krizhevsky, Sutskever, et al.[175] showed that ReLUs produce significantly

better results on image recognition tasks using deep networks than the common sigmoid-shaped activation functions . Since, by the chain rule, the derivative of a composed function is the product of each of the derivatives of its composing functions, the training signal can get exponentially small. The ReLU does not have this problem, at least in the positive range, because there its derivative is simply one. While the ReLU solved the problem of vanishing gradients for positive values, it completely cut off the gradient for negative ones; thus once a neuron enters the negative regime (either through initialization or during training) for most samples, no training signal can pass through it. To resolve this problem Maas et al. [176] introduced the leaky ReLU, which is also linear for negative values but with a very small, although non-zero, slope; for positive values it behaves like the ReLU. Soon after He et al.[177] demonstrated that it is advantageous to make the slope of the negative part of the leaky ReLU an additional parameter of each neuron. This parameter was trained alongside the weights and biases of the neural network using gradient descent.



(a) hyperbolic tangent (sigmoidal)　　　　(b) exponential linear unit

(c) ReLU　　　　(d) leaky ReLU
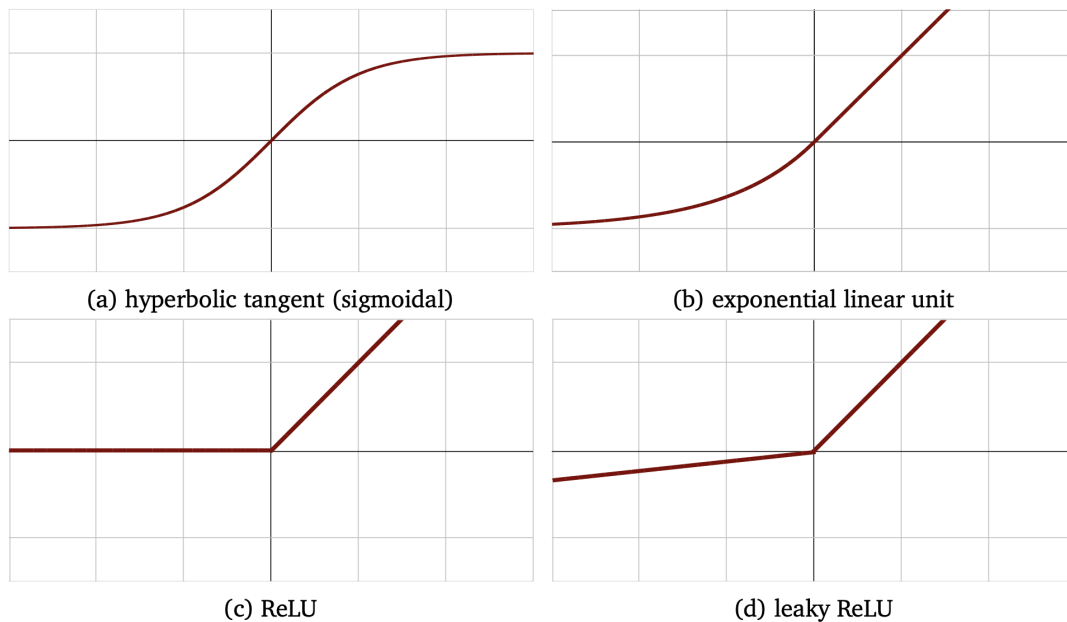
Figure 5.3: Various activation functions used commonly in neural networks [8]

## 5.1.4　Back propagation

Back propagation algorithm is one of the most widely used learning procedures for multi-layer network because of its simplicity. When training a neural network, a loss function is obtained, which represents how far the network predicts compared to the true values. Back propagation calculates the gradient of the loss function with respect to each of the weights of the network. This enables every weight to be updated individually to gradually reduce the loss function over many training iterations [178].

64

The mechanism of back propagation is to calculate the gradient proceeding backwards through the feed forward network from the last layer through to the first. To calculate the gradient at a particular layer, the gradients of all following layers are combined via the chain rule of calculus.

Let us assume that for a particular input pattern $X_n$ in the training set, the error function is defined as,

$$E_n = \frac{1}{2} \sum_{k=1}^{K} (t_k - y_k)^2 \tag{5.2}$$

where $y_k$ is the output predicted by the neural network, and $t_k$ is the corresponding target value. The derivative of the error function with respect to output $y_k$ is

$$\frac{\partial E_n}{\partial y_k} = y_k - t_k \tag{5.3}$$

Suppose we have sigmoidal activation functions given by the equation

$$h(a) = \frac{1}{1 + e^{-a}} \tag{5.4}$$

The output of each neuron is between 0 and 1. The derivative of sigmoidal function is simple and is expressed as

$$h'(a) = h(a)(1 - h(a)) \tag{5.5}$$

The training includes forward propagation first given by

$$a_j = \sum_{i=0}^{D} w_{ji}^{(1)} x_i \tag{5.6}$$

$$z_j = h(a_j) \tag{5.7}$$

$$a_k = \sum_{j=0}^{M} w_{kj}^{(2)} z_j \tag{5.8}$$

$$y_k = h(a_k). \tag{5.9}$$

This is the output of the ANN and now the derivatives of error function with respect to weight can be calculated using the chain rule,

$$\frac{\partial E_n}{\partial w_{kj}^{(2)}} = \frac{\partial E_n}{\partial y_k} \cdot \frac{\partial y_k}{\partial a_k} \cdot \frac{\partial a_k}{\partial w_{kj}^{(2)}} = \sum_{k=1}^{K} [(y_k - t_k).y_k(1 - y_k)] z_j \tag{5.10}$$

$$\frac{\partial E_n}{\partial w_{ji}^{(1)}} = \frac{\partial E_n}{\partial y_k} \cdot \frac{\partial y_k}{\partial a_k} \cdot \frac{\partial a_k}{\partial z_j} \cdot \frac{\partial z_j}{\partial a_j} \cdot \frac{\partial a_j}{\partial w_{ji}^{(1)}} \tag{5.11}$$

$$\frac{\partial E_n}{\partial w_{ji}^{(1)}} = \sum_{k=1}^{K} [(y_k - t_k).y_k(1 - y_k).w_{kj}^{(2)}].z_j(1 - z_j).x_i \tag{5.12}$$

Now as all the derivatives have been calculated, the weight value is adjust using the gradient descent algorithm defined by,

$$\mathbf{W}^{(\tau+1)} = \mathbf{W}^{(\tau)} - \eta \nabla E(\mathbf{W}^{(\tau)}) \tag{5.13}$$

Here $\tau$ represents the iteration stepps and the $\eta$ is known as the learning rate. After each step, the gradient is re-evaluated for new weight vector and the process is repeated. Note that the error function is defined with respect to the training set, and so each step requires to re-calculate the output of the neural network. Hence, each step of the gradient descent algorithm comprises two stages: in the first stage, known as forward propagation, the output of the neural network for a set of weights w is calculated. In the second stage, known as BackPropagation, the derivatives of the error function with respect to the weights are evaluated. These derivatives are then used to compute the adjustments to be made to the weight and bias parameters.

## 5.2    Motivation of the research

The density functional theory (DFT) of Hohenberg, Kohn, and Sham [21, 22] allows for efficient computation of material properties by avoiding the complicated many-electron wave function in favor of the computationally convenient electron density when solving the electronic structure problem. Due to its useful accuracy and efficiency, DFT has become the most widely used computational approach for solving problems in chemistry and condensed matter physics/electronic structure.

In the Kohn–Sham (KS) formulation of DFT, the majority of the energy is calculated exactly, leaving only a small portion of the energy, known as the exchange-correlation (XC) energy, to be approximated. There has been extensive research on improving approximations to the XC energy and the resulting functionals are roughly categorized into a hierarchy of increasing complexity and expected accuracy [179]. The meta-generalized gradient approximations (mGGAs), the highest category that depends only on semi-local ingredients, are becoming increasingly popular for allowing high accuracy at favorable computational cost. The mGGA functionals commonly consist of an XC energy density, $e_{\mathrm{xc}}$, built from three ingredients: the electron density, $n(\mathbf{r})$, its gradient, $|\nabla n(\mathbf{r})|$, and the kinetic energy density $\tau(\mathbf{r}) = \sum_i^{\mathrm{occ.}} |\nabla \varphi_i(\mathbf{r})|^2$, where $\varphi_i$ are the occupied KS orbitals. Though less common, density functionals depending on the density Laplacian $\nabla^2 n(\mathbf{r})$ instead of (or in addition to) $\tau$ are also included at the mGGA level. The total XC energy for the system is calculated

by integrating this XC energy density over all space,

$$E_{\mathrm{xc}} = \int d\mathbf{r}\, e_{\mathrm{xc}}^{\mathrm{mGGA}}(n(\mathbf{r}), |\nabla n(\mathbf{r})|, \tau(\mathbf{r}), \nabla^2 n(\mathbf{r})), \tag{5.14}$$

$$= \int d\mathbf{r}\, F_{\mathrm{xc}}^{\mathrm{mGGA}}(n(\mathbf{r}), |\nabla n(\mathbf{r})|, \tau(\mathbf{r}), \nabla^2 n(\mathbf{r})) n(\mathbf{r}) \epsilon_{\mathrm{x}}^{\mathrm{LDA}}(\mathbf{r}), \tag{5.15}$$

where $F_{\mathrm{xc}}^{\mathrm{mGGA}}$ is the XC enhancement factor and $\epsilon_{\mathrm{x}}^{\mathrm{LDA}}(\mathbf{r}) = -(3/4\pi^2)(3\pi^2 n)^{1/3}$ is the exchange energy per particle of the uniform electron gas.

The kinetic energy density, $\tau$, is commonly used in mGGAs to recognise different chemical environments through iso-orbital indicator variables [180, 12, 122], and as a component of the spherical exchange hole expansion[181]. While theoretically convenient, $\tau$ introduces an implicit dependence on the KS orbitals, which brings some complications. 1) It reduces computational efficiency by requiring additional basis function derivatives to be computed on the numerical quadrature grid, which can be more costly for Fourier transform based periodic codes. 2) It prevents the functional being used in orbital-free DFT calculations. 3) Evaluation of the XC potential for $\tau$-dependent functionals requires either optimised effective potential (OEP) techniques [88, 89], or a generalised KS scheme[90?, 92]. While a generalised KS treatment can be computationally convenient, the effective XC potential operator of a $\tau$ dependent mGGA is no longer a multiplicative function, $v_{\mathrm{xc}}(\mathbf{r})$, and is instead a non-local operator, $\hat{v}_{\mathrm{xc}}$.

Despite the potential advantages offered avoiding the use of orbital dependent ingredients such as $\tau$, $\nabla^2 n(\mathbf{r})$ remains a less explored ingredient and its physical significance for the XC energy is unclear. Recently, Mejia-Rodriguez and Trickey [93, 13] replaced $\tau(\mathbf{r})$ with functions of $\nabla^2 n(\mathbf{r})$ in many mGGA XC functionals to recover similar (but not identical) performance to the parent functionals. This suggests an intriguing but unclear relationship between $\tau(\mathbf{r})$ and $\nabla^2 n(\mathbf{r})$, though an explicit relationship remains elusive despite significant effort [182].

Machine learning (ML) has proven to be a powerful tool for building complicated non-linear mappings for which little theoretical guidance exists. It has proved successful in building complex models across a wide variety of fields including robotics [183, 184], pattern recognition[185, 186], drug design [187, 188, 189], and gaming [190]. Within DFT research, there has been a recent practice of applying ML to construct density functionals. In 2012, Synder *et. al.* used a ML approximation to construct an orbital-free non-interacting kinetic energy functional $T_s[n]$ for spinless fermion systems [38, 39]. Brockherde *et. al.* used ML to learn the Hohenberg-Kohn (HK) map between electron density and external potential to give a mechanism that bypasses solving the KS equations [40]. Several other works have focused on the XC potential problem [41, 42, 43, 44]. A perspective surveying the current state of ML in computational chemistry and materials science was recently published by Westermayr, Gastegger, and Schütt in Ref. [191].

The Strongly Constrained and Appropriately Normed (SCAN) functional [12] has proven to be effective for describing a wide variety of systems [34], such as liquid water and ice [192], semiconductor materials [193] and metal oxides [194], as well as for key properties of correlated materials like cuprates [3, 116, 195]. SCAN's success is credited to its adherence to all of the known exact-constraints applicable to a meta-GGA functional, along with the philosophy of using "appropriate norms" to set free parameters with minimal empiricism. These appropriate norms are the systems for which a semi-local density functional approximation can be expected to be highly accurate, that is: the total energies of systems with highly localized exchange-correlation holes [12].

In light of this dual success of both constraint driven design and ML techniques, a question arises. Is the philosophy of exact constraints and appropriate norms compatible with ML for functional design? Growing evidence that exact constraint adherence can improve ML transferability suggests it is. Indeed, earlier works from Hollingsworth *et. al.* show that enforcing coordinate scaling constraints can improve machine-learned functionals [45]. Nagai and collaborators [47] recently introduced a method to analytically impose asymptotic constraints on an ML XC functional, finding generally improved accuracy. More recently, Kirkpatrick and co- workers [41] developed a functional DM21 (DeepMind21) that for the first time, obeys two classes of constraints on systems with fractional electrons, which are fractional charge systems and fractional spin systems [196].

In our work, we explore this idea of exact constraints and appropriate norms satisfaction by training a deep artificial neural network (ANN) to reproduce the XC energy density of the SCAN functional using $\nabla^2 n(\mathbf{r})$ instead of $\tau(\mathbf{r})$, a similar goal to the SCAN-L functional [13]. The de-orbitalization of SCAN stands as a convenient application for exploring the idea of constraint satisfaction in ML functionals, with SCAN-L providing an analytical benchmark for the task.

The ML models will be trained to perform the transformation,

$$F_{\mathrm{xc}}^{\mathrm{SCAN}}\left(n(\mathbf{r}), |\nabla n(\mathbf{r})|, \tau(\mathbf{r})\right) \to F_{\mathrm{xc}}^{\mathrm{SCAN-ML}}\left(n(\mathbf{r}), |\nabla n(\mathbf{r})|, \nabla^2 n(\mathbf{r})\right)$$

We approach this mapping of orbital free ingredients onto the SCAN XC energy density using two different ML models adhering to different numbers of exact conditions. One model is a single totally-connected ANN trained for equation 5.2 directly, termed the "combined model". The other model is built as two complementary exchange and correlation-like ANN designed to obey exact spin-scaling constraints, termed the "spin-scaled model". We also impose the general Lieb–Oxford bound [69] on these models to create models that also satisfy this constraint.

## 5.3   Exact Constraints

While the exact XC functional remains unknown, it is known to obey many mathematical conditions, commonly called the "exact constraints" of XC functionals. Currently, 17 exact constraints [12], are known to apply at the semi-local functional level. These can be broken down as conditions for the exchange energy: (1) negativity, (2) spin-scaling [65], (3) uniform density scaling [66], (4) the slowly-varying density gradient expansion (to fourth order) [53], (5) non-uniform density scaling [67, 68], and (6) a tight bound for two-electron densities [63, 69]. For correlation: (7) non-positivity, (8) the slowly-varying density gradient expansion (to second order) [197], (9) uniform density scaling to the high-density limit [66], (10) uniform density scaling to the low-density limit [66], (11) zero correlation energy for any one-electron spin-polarized density, and (12) nonuniform density scaling [67, 68]. Finally, there are constraints known for the exchange and correlation together: (13) size extensivity, (14) the general Lieb–Oxford bound [198, 69], (15) weak dependence upon relative spin polarization in the low-density limit [70, 56], (16) static linear response of the uniform electron gas [71], and (17) the Lieb–Oxford bound for two-electron densities [69].

Here, we consider a subset of the 17 constraints that are easy to enforce in an ML model.

The first of these is the behavior of the exchange energy under constraint (3), behavior under uniform density scaling,

$$n_\gamma(\mathbf{r}) = \gamma^3 n(\gamma\mathbf{r}), \tag{5.16}$$

where $\gamma$ is a positive real number. The exact exchange energy is known to scale as,

$$E_\mathrm{x}[n_\gamma] = \gamma E_\mathrm{x}[n], \tag{5.17}$$

under this transformation. The effect of this condition on kernel ridge regression models was investigated by Hollingsworth, Baker, and Burke in Ref. 45 for Hook's atom model systems, concluding that its inclusion improved ML functional performance.

Condition (2), the spin-scaling relation for exchange energy,

$$E_\mathrm{x}[n_\uparrow, n_\downarrow] = \frac{E_\mathrm{x}[2n_\uparrow] + E_\mathrm{x}[2n_\downarrow]}{2}, \tag{5.18}$$

is simple to enforce for ML exchange models by requiring separate exchange and correlation models, and that the same exchange model handle each spin channel independently.

Condition (14), the general Lieb–Oxford bound on the XC enhancement factor, states that,

$$0 \leq F_{\mathrm{xc}}(\mathbf{r}) \leq 2.215. \tag{5.19}$$

These bounds can be enforced on ML models by including a post-processing step that maps ML model output, denoted $\mathrm{ANN}_{\mathrm{xc}}(\mathbf{r})$, to the desired domain, e.g.

$$F_{\mathrm{xc}}^{\mathrm{ML}}(\mathbf{r}) = \frac{2.215}{1 + \mathrm{ANN}_{\mathrm{xc}}(\mathbf{r})^2}. \tag{5.20}$$

A similar approach can be applied to impose condition (6), the tight bound for the exchange enhancement factor $F_{\mathrm{x}}(\mathbf{r}) \in [0, 1.174]$, if exchange and correlation models are separated. Conveniently, such post-processing also enforces conditions (1) and (7), non-positivity, by constraining $F_{\mathrm{xc}} \geq 0$. It appears more challenging to enforce the exact constraints outside this subset in ML models. For example, while enforcing the second (and fourth) order gradient expansions for correlation (and exchange) is relatively straightforwards in analytical functionals, the ML design contains thousands of parameters which cannot be fully controlled. Thus, it is non-trivial to enforce such gradient expansion constraints on the model *a priori*. Despite this, the nature of supervised training against methods that obey such constraints (such as SCAN) will result in the trained model effectively learning a degree of the constraints. Without the rigorous enforcement described above it is unclear how well such adherence will transfer out of the training domain however.

## 5.4   Input domain

Identifying input domain is a critical part of ML model design as a model's performance can be strongly dependent upon the nature of its inputs. Since our central interest is to replace kinetic energy density $\tau(\mathbf{r})$ dependence we will only consider orbital free ingredients. Four density inputs were intially identified,

$$r_{\mathrm{s}} = \left( \frac{3}{4\pi n} \right)^{1/3} \quad - \text{ Wigner-Seitz radius} \tag{5.21}$$

$$s = \frac{|\nabla n|}{2(3\pi^2)^{1/3} n^{4/3}} \quad - \text{ Reduced density gradient} \tag{5.22}$$

$$\zeta = \frac{n_\uparrow - n_\downarrow}{n_\uparrow + n_\downarrow} \quad - \text{ Spin polarization} \tag{5.23}$$

$$q = \frac{\nabla^2 n}{4(3\pi^2)^{2/3} n^{5/3}} \quad - \text{ Reduced density laplacian} \tag{5.24}$$

The above dimensionless ingredients are preferred for XC functionals rather than using the density variables directly because the correct uniform coordinate density-scaling behaviour can be satisfied with them

[66]. The Weigner–Seitz radius is the radius of a sphere which on average contains one electron. The reduced density gradient introduces inhomogeneity which measures how fast and how much the density varies on the scale of the local Fermi wavelength $2\pi/k_F$. The reduced density Laplacian also measures the density inhomogeneity and can distinguish bonds, in contrast to reduced gradient which vanishes at the middle of the bond [182].

Further exploration revealed that including additional ingredients directly from the SCAN exchange and correlation functionals (see Ref.12 supplemental material 'SX') could improve model performance:

$$\epsilon_c^0(r_s, s, \zeta) - \text{Single orbital correlation} \tag{5.25}$$

$$\epsilon_c^1(r_s, s, \zeta) - \text{Slowly varying correlation} \tag{5.26}$$

$$g_x(s) - \text{Exchange inhomogeneity} \tag{5.27}$$

$$h_0 = 1.174 - \text{Single orbital exchange} \tag{5.28}$$

$$h_1 = 1.065 - \frac{0.065}{(1 + \frac{10s^2/81}{0.065})} - \text{X } 2^{\text{nd}} \text{ order gradient expansion} \tag{5.29}$$

These additional inputs are combinations of the original density ingredients and do not provide any new information directly. Their inclusion makes learning more efficient however, as it reduces the manipulations that the network must learn. This limits dependence on the network to only learning $\tau$ dependent aspects, rather than requiring it to learn every detail of the SCAN functional.

The possible range of the input parameters is very different to desired range of the model outputs: $0 \leq F_{\text{xc}}^{\text{ML}} \leq 2.215$. For example, the domain of $r_s$ and $s$ is $[0, +\infty)$ while $q$ is $(-\infty, \infty)$. Such a mismatch in the magnitude of input and output is known to be challenging for ML models. To correct for this we pre-processed the unbounded inputs using the hyperbolic tangent function, $\tanh(x)$ [199], to smoothly map the unbounded quantities to $(-1, +1)$. With pre-processing, the inputs are defined as,

$$\tilde{r}_s = \tanh(r_s), \tag{5.30}$$

$$\tilde{s} = \tanh(s), \tag{5.31}$$

$$\tilde{q} = \tanh(q). \tag{5.32}$$

Finally, we pre-process $\zeta$ as,

$$\tilde{\zeta} = \frac{1}{2} \left[ (1 + \zeta)^{4/3} + (1 - \zeta)^{4/3} \right], \tag{5.33}$$

to ensure the model is a symmetric function of spin polarisation [65]. The inputs of equations 5.25-5.29 are unprocessed as their ranges are already correctly bounded. Note that the pre-processed variables (Eqs.
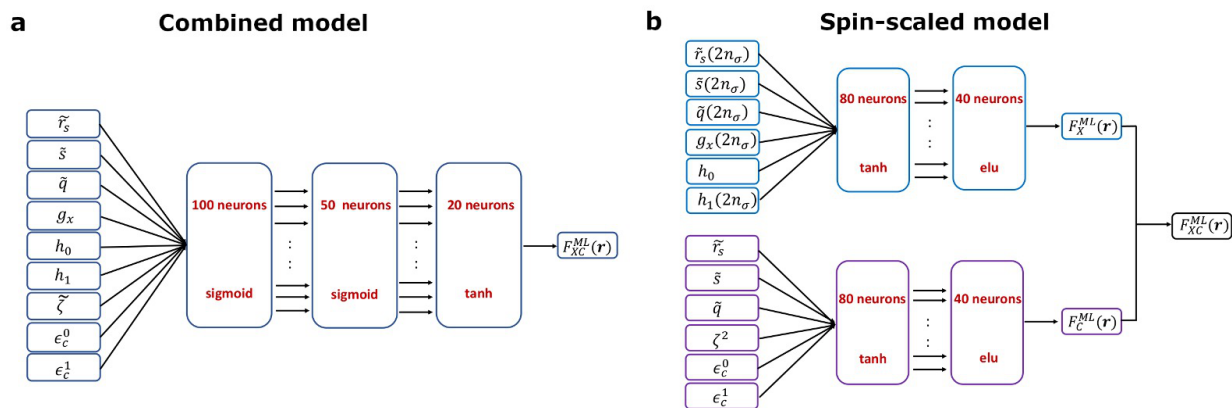
Figure 5.4: ML model architecture and workflow for (**a**) combined model (**b**) spin-scaled model. For the combined model, total density $(n_\uparrow + n_\downarrow)$ is given as the input. In the spin-scaled model, the upper architecture is for the exchange model learning while the lower is the correlation-like model. Spin-scaling is satisfied in the exchange model represented by $(2n_\sigma)$ where $\sigma = \uparrow\downarrow$ spin channels.

5.30-5.33) are only supplied to the network and are not used to generate the additional inputs of Eqs. 5.25-5.29.

Having identified the input domain, a training data set consisting of 20 atoms was generated using accurate spherical Hartree–Fock orbitals [9, 10, 11] containing open and closed shell atoms (He, Li, Be, B, C, N, O, F, Ne, Na, P, Cl, Ar, K, Cr, Cu, Cu+, As, Kr, Xe) with $s$, $p$, and $d$ valence shells. The energetically important region of the atomic density is typically between 0 and 4 $a_0$ and the density of each atom was therefore sampled in shells of decreasing sample density for models, with 2500 points evenly distributed radial sample in $r < 1$ bohr (core), 1500 in $1 \leq r < 4$ bohr, and 500 in the tail region $4 \leq r < 10$ bohr.

This atomic training data was augmented with densities from the "appropriate norm" systems used in SCAN's construction. The first norm is the one electron hydrogen atom, which is used to ensure SCAN's one electron self-correlation freedom (constraint 11). The second and third norms are the jellium surface densities for $r_s = 2, 3, 4$ and 6 [200, 201], and the converged SCAN orbitals of the compressed argon dimer with nuclear separations of 1.6, 1.8, and 2.0 Å, which were used to fix SCAN's interpolation function parameters [12]. We restrict the training data set to only these appropriate norms and avoid including chemically bonded systems. While increasing the domain of the training data is expected to give the resulting ML models higher accuracy for a wider range of problems, our intent here is to observe how exact constraint satisfaction can transfer knowledge from minimal training data onto diverse problems.

## 5.5 Neural Network architecture and Training

In this work, all the networks were built on the basis of the ML framework Tensorflow [202]. For the models, the non-linearity in the mapping is acquired by using sigmoid[203], tanh and exponential linear unit (elu) [204] activation functions, chosen as commonly used continuously differentiable activation functions. Ensuring smooth activation functions was found to be essential for obtaining reasonable XC potentials, as discussed below. The data set was randomly divided into training (80%) set and validation (20%) set, using train-test split feature of sci-kit learn [205]. Hyper-parameter search identified a 3 layered model with sigmoid, sigmoid and tanh activation functions as preferable for the combined model while a 2 layered model with tanh and elu activation functions for spin-scaled model were obtained. The network weights and biases were optimized by stochastic gradient descent with the Adam optimizer [206] using a learning rate of 0.05, applying a gradient step after each sample in the training data set. The optimized model was chosen as that which minimizes the error for the validation set, generally found after one complete pass of the training data.

### 5.5.1 Combined Model

Figure 5.4 a) presents a schematic for the simple neural network(NN) architecture, termed the "combined model". As the name suggests, the combined model receives inputs constructed from total density $(n_\uparrow + n_\downarrow)$ as the features, and targets SCAN's exchange-correlation enhancement factor. Different numbers of hidden layers and neuron counts were tested, with a three layered model with 100, 50 and 20 neurons in respective layers found to perform best.

For the combined model, the loss function to be optimized in the learning process is defined as,

$$\mathcal{L}_{\text{combined}} = \frac{1}{N} \sum_i^N \left( F_{\text{xc}}^{\text{ML}} - F_{\text{xc}}^{\text{SCAN}} \right)^2, \tag{5.34}$$

where $N$ is the number of training data points, thus minimizing the mean square difference between SCAN XC enhancement and the learned XC enhancement. The Lieb-Oxford bound for the combined model is introduced as a post-processing mechanism following the explanation in Eq. 5.20.

### 5.5.2 Spin-Scaled Model

The spin-scaled model follows a more complex architecture that allows it to obey the spin-scaling exact constraint by treating exchange and correlation separately, as discussed above. The overall architecture for the spin-scaled model is presented in Figure 5.4 b). The spin-scaled model is comprised of two separate networks, one for exchange and one for correlation. These networks are trained separately and later combined

to form the complete model. Training is therefore carried out as a two step process.

This separation by spin channel reduces the input domain for the exchange network to six features suitable for exchange, $\{\tilde{r}_{s\sigma}, \tilde{s}_\sigma, \tilde{q}_\sigma, g_{x\sigma}, h_{0\sigma}, h_{1\sigma}\}$, separately generated for each spin $\sigma$. The exchange network is trained first to minimize the mean square difference with the SCAN exchange enhancement defined as,

$$\mathcal{L}_{\text{exchange}} = \frac{1}{N} \sum_i^N \left(F_x^{\text{ML}} - F_x^{\text{SCAN}}\right)^2, \tag{5.35}$$

with the spin-scaled exchange enhancement,

$$F_x^{\text{ML}} = \frac{F_x(2n_\uparrow)e_x^{\text{LDA}}(2n_\uparrow) + F_x(2n_\downarrow)e_x^{\text{LDA}}(2n_\downarrow)}{2e_x^{\text{LDA}}(n_\uparrow + n_\downarrow)}. \tag{5.36}$$

As the exchange energy must be invariant to permutation of spin labels, the same exchange network used for both spin channels and should trained on both spin channels of the training data. The exchange network has two layers with 80 and 40 neurons at the first and second layers respectively and the activation functions are tanh and exponential linear unit (elu) [204].

The correlation energy is not subject to the same spin scaling constraint and is handled by a separate model. This second model takes a reduced set of the total density $(n_\uparrow + n_\downarrow)$ input variables suitable for correlation: $\{\tilde{r}_s, \tilde{s}, \tilde{q}, \zeta^2, \epsilon_c^0, \epsilon_c^1\}$. This second network has the same hyper-parameters as the exchange network.

The loss function for the second network is,

$$\mathcal{L}_{\text{correlation}} = \frac{1}{N} \sum_i^N \left[F_c^{\text{ML}} - (F_{xc}^{\text{SCAN}} - F_x^{\text{ML}})\right]^2, \tag{5.37}$$

where $F_x^{\text{ML}}$ is the output of the previously trained exchange network. This second network is therefore not a true model of SCAN correlation as the loss function of Eq. 5.37 drives it to compensate for deficiencies in the exchange network, though correlation effects will dominate if the exchange network is accurate.

Finally, the total enhancement factor is obtained by summing the exchange network and second network enhancement factors as,

$$F_{xc}^{\text{spin-scaled}} = F_x^{\text{ML}} + F_c^{\text{ML}}. \tag{5.38}$$

The Lieb-Oxford bounds for the spin-scaled model are introduced separately for exchange and the correlation parts as they are trained separately. For the exchange part, we follow similar mechanism as explained in Eq. 5.20 where the bound is introduced to the exchange enhancement factor as,

$$F_x^{\text{ML-bound}}(\mathbf{r}) = \frac{1.174}{1 + \text{ANN}_x(\mathbf{r})^2}. \tag{5.39}$$

Here we choose a tight bound of 1.174 for the exchange.

For correlation, we introduce the bound by modifying the loss function to include an additional penalty term,

$$\mathcal{L}_{\text{correlation}}^{\text{bound}} \quad = \quad \frac{1}{N} \sum_i^N \{ \left[ F_{\text{c}}^{\text{ML}} - (F_{\text{xc}}^{\text{SCAN}} - F_{\text{x}}^{\text{ML}}) \right]^2 \; + \; \mu \; \times \; relu(-1 \; \times \; (2.215 \; - \; F_{\text{xc}}^{\text{ML}})) \}, \quad (5.40)$$

where $\mu$ value is chosen to be 20. Here we see that if the total XC enhancement factor is smaller than the tight bound 2.215 the penalty term is zero whereas any value of total XC enhancement factor greater than 2.215 will incur penalty. This total loss function is minimized to satisfy the Lieb–Oxford bound introduced in the ML model.

## 5.6 Results and discussion

### 5.6.1 Atomic Performance

Figure 5.5 shows the SCAN and ML-model XC enhancement for the silicon atom, which was not part of the training set. Figures a) and b) show combined and spin-scaled models respectively without Lieb–Oxford bound, while c), d) include Lieb–Oxford bound constraint. All the ML models show good agreement with the SCAN's XC enhancement factor for this system. The combined model without Lieb–Oxford bound shows slightly less variation in the energetically important region between r = 0 and r = 4, the nuclei and inter-shell regions.

During training we did not target total XC energy directly, in favor of learning the XC energy density of an existing mGGA instead. This switch towards mimicking XC energy density, a local property, has three benefits. Most importantly it reduces the complexity of the training by avoiding summing the derivatives of many training points in a numerical integration batch. Secondly, far more training data is available for a given functional's local energy density than for total XC energies, as every point in the all-space integration of any system can now be considered a training point. Thirdly, this avoids the introduction of a gauge freedom in which many different energy density functions can integrate to the same total energy, which could result in learning a model that gives reasonable total energy, but poor local accuracy to the SCAN energy density. Despite this training against local XC density it will be shown that the models are successful in recovering the total XC energy for the training atom sets, predicting the global property from local training.
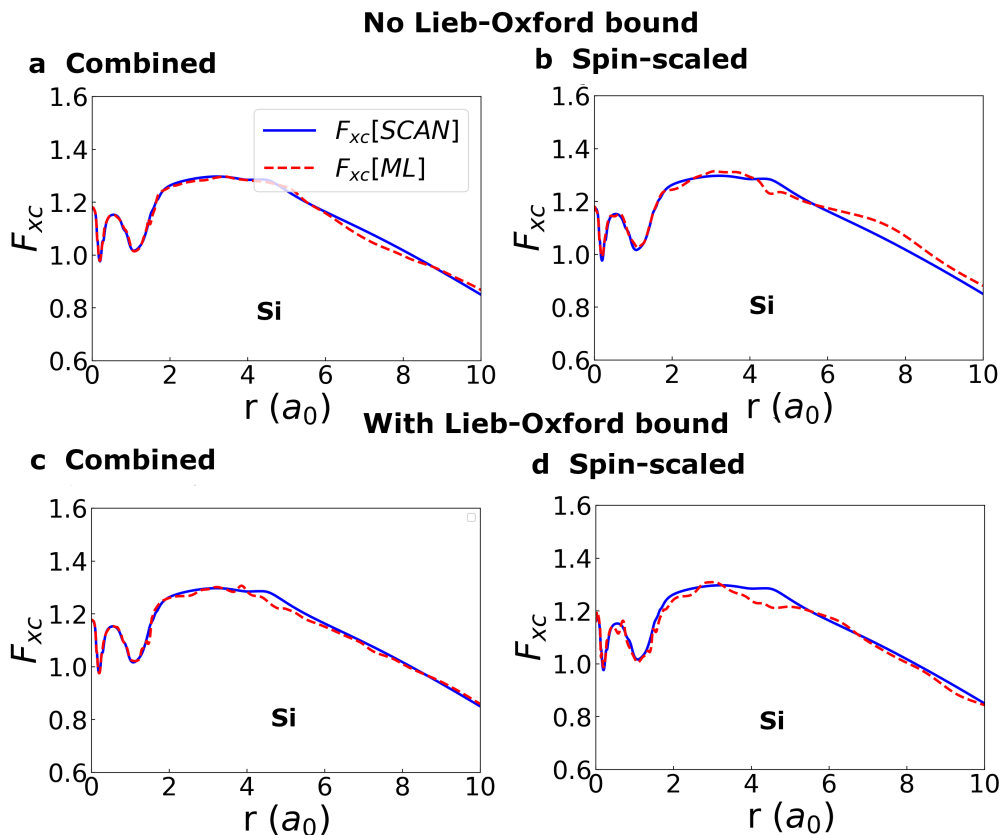
Figure 5.5: XC enhancement plots for the test silicon atom which was not included in the training set for (**a**) combined model and (**b**) spin-scaled model without Lieb–Oxford bound while (**c**) and (**d**) represent same as (**a**) and (**b**) with Lieb-Oxford bound. All models performances are compared against SCAN functional. Density was obtained from accurate spherical HF orbitals [9, 10, 11].

## 5.6.2 Molecular Test Sets

For the models trained against data from atomic systems, a real challenge is to generalize to problems outside the training domain. We examine this by looking at model accuracy for the open- and closed-shell molecules of the G3 test set [15]. The input ingredients (density, gradient and laplacian) and the SCAN $F_{xc}^{\text{SCAN}}$ target for all molecular calculations were generated from self-consistent SCAN orbitals in the 6-311++G(3df,3pd) basis set [16, 17]. All molecular calculations were carried using the QUantum Electronic Structure Techniques (QUEST) program [18].

The mean absolute error in atomization energy for the G3 set are summarized in Tables 5.1 and 5.2 for open-shell, closed-shell, and total collections. Overall all models showed comparable performance giving accuracy close to the SCAN functional (MAE 6.53 kcal mol$^{-1}$ ). In particular, enforcing the correct spin-scaling relation in the ML models improved accuracy for the open-shell systems, though this was accompanied by a smaller reduction in accuracy for the closed shell systems. Introduction of the Lieb–Oxford bound to

Table 5.1: Mean absolute error (MAE) in kcal mol$^{-1}$ for G3 set of 226 molecular atomization energies [15]. All SCAN G3 calculations were performed fully self-consistently with the 6-311++G(3df,3pd) basis set [16, 17] in the QUEST program[18]. The ML calculations were performed non self-consistently from SCAN orbitals. The ML models with Lieb–Oxford bound are denoted by "LO" within table. The model performances are compared against parent SCAN functional.

| | SCAN | | |
| ML models | closed shell (MAE) | open shell (MAE) | (G3) (MAE) |
| --- | --- | --- | --- |
| Combined | 7.49 | 7.89 | 7.69 |
| Combined-LO | 11.88 | 9.26 | 10.58 |
| Spin–scaled | 8.03 | 4.85 | 6.44 |
| Spin-scaled-LO | 7.66 | 5.66 | 6.66 |

Table 5.2: Mean absolute error (MAE) in kcal mol$^{-1}$ for G3 set of 226 molecular atomization energies [15]. All SCAN G3 calculations were performed fully self-consistently with the 6-311++G(3df,3pd) basis set [16, 17] in the QUEST program[18]. The ML calculations were performed non self-consistently from SCAN orbitals. The ML models with Lieb–Oxford bound are denoted by "LO" within table. The model performances are compared against reference values.

| | Reference | | |
| ML models | closed shell (MAE) | open shell (MAE) | (G3) (MAE) |
| --- | --- | --- | --- |
| Combined | 7.80 | 5.17 | 6.48 |
| Combined-LO | 13.24 | 7.26 | 10.25 |
| Spin–scaled | 8.55 | 3.73 | 6.14 |
| Spin-scaled-LO | 11.14 | 6.35 | 8.75 |
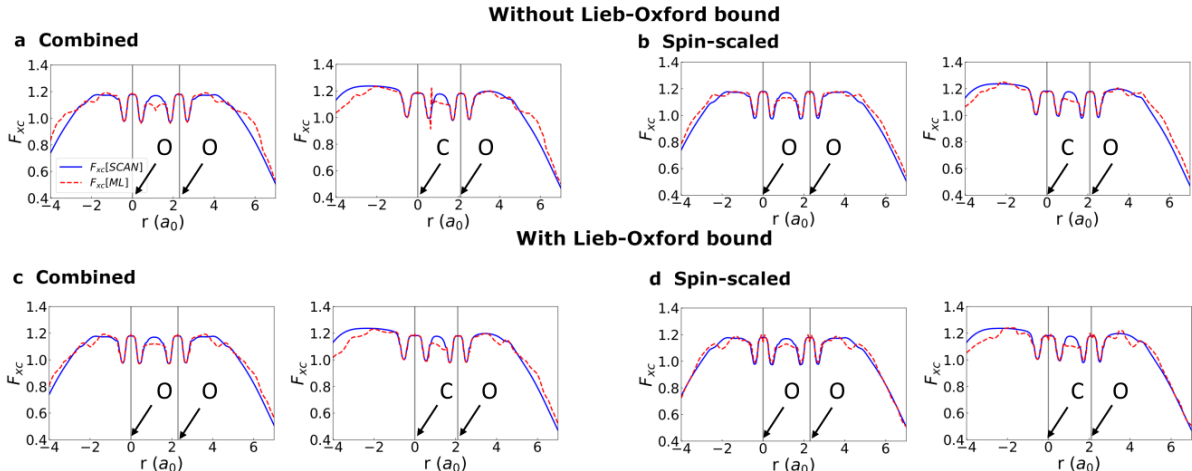


Figure 5.6: Exchange-correlation enhancement plots for $O_2$ (open shell) and CO (closed shell) from (**a**) combined model and (**b**) spin-scaled model without Lieb–Oxford bound. (**c**), (**d**) are same as (**a**) and (**b**) but for models including Lieb–Oxford bound. The gray vertical lines mark atomic positions.

the combined model deteriorated performance for both open and closed shell systems. This unexpected poor performance suggests that enforcing the Lieb–Oxford bound through Eq. 5.20 does not seem to be a successful strategy. While such post-processing seems theoretically convenient, the results from the G3 set

and lattice constant below show that it significantly limited model learning during training. We understand this as an effect of requiring the network to simultaneously return very large numbers when target $F_{\mathrm{xc}}(F_{\mathrm{x}})$ is small, and very small numbers in energetically significant regions where $F_{\mathrm{xc}}(F_{\mathrm{x}})$ approaches $2.215(1.174)$ for combined(spin–scaled) models. The spin–scaled model performs better than combined model because the number to return $(1.174)$ is relatively smaller compared to $2.215$ for combined model and hence error is smaller. An alternative solution for enforcing this constraint could be to simply truncate the range of the network output,

$$F_{\mathrm{xc}}^{\mathrm{ML}} = \max(0, \min(2.215, \mathrm{ANN}(r))), \tag{5.41}$$

and

$$F_{\mathrm{x}}^{\mathrm{ML}} = \max(0, \min(1.174, \mathrm{ANN}(r))), \tag{5.42}$$

however this may introduce undesirable discontinuities in the partial derivatives of the model, transferring into a non-physical XC potential.

In order to better understand how faithfully the ML models are reproducing the SCAN functional, Figure 5.6 compares the XC enhancement factor, $F_{\mathrm{xc}}$, for the open shell $O_2$ and closed shell CO molecules. We see that all the models are accurate in the areas immediately around the nuclei. This is expected from the good atomic performance as these core regions are relatively unchanged by the covalent bonding. The models deviate more severely around the bond center, with all models underestimating $F_{\mathrm{xc}}^{\mathrm{SCAN}}$. In these regions $|\nabla n| \to 0$ and hence $s \to 0$, while the density $n$ remains significant. Such regions are under-represented in the training set, appearing only in small regions at the center of the compressed $Ar_2$ diatomic. This suggests that the spin scaling relation enforced in the spin-scaled model as well as the Lieb–Oxford bound are insufficient to transfer learning from a training set that does not include chemical bonding, onto systems that are chemically bound. Further constraint satisfaction, or inclusion of bonding data into the training set, is likely necessary to improve model accuracy at these important points. We also note that the combined model with no Lieb–Oxford bound exhibits sharp spikes in $F_{\mathrm{xc}}$ in the bonding regions that are not seen for other ML models or the SCAN functional.

### 5.6.3   Lattice Constants of solids

The transferability of the ML functionals was further tested by calculating the lattice constants of 20 solids from the LC20 test set[207]. This tests the model's ability to generalise into further unseen chemical environments in periodic systems, as well as requiring description of the energy as a function of nuclear displacement. The LC20 set is therefore a sensitive test of model transferability. The equilibrium lattice
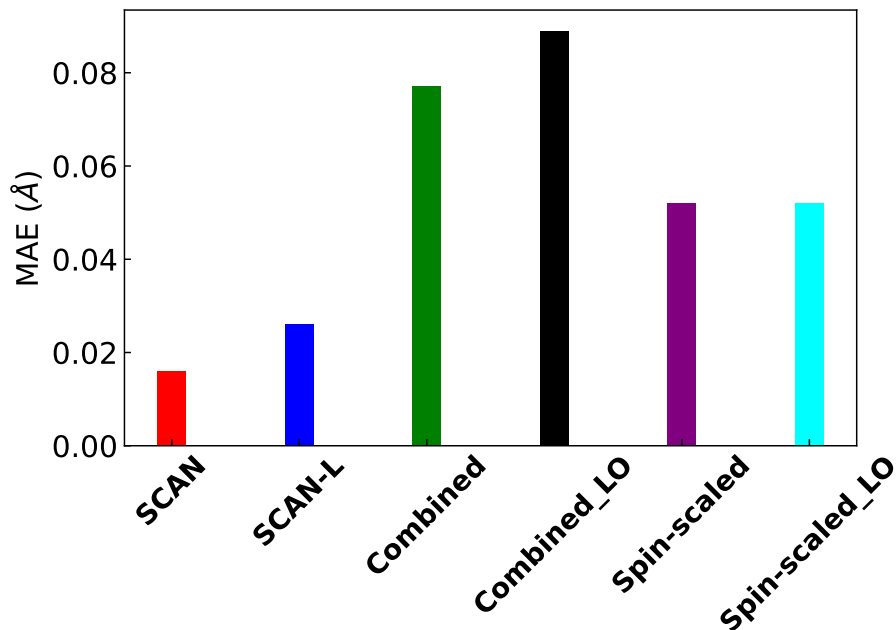
Figure 5.7: Mean Absolute Error (MAE, Å) for SCAN, whose results are obtained from Ref.[12], SCAN-L, whose results are obtained from Ref. [13], combined, combined with Lieb–Oxford bound (denoted "LO" within figure), spin-scaled and spin-scaled with Lieb–Oxford bound for the lattice constant set of 20 solids. The ML calculations were obtained from non self-consistent calculations using PBE densities generated self-consistently, using FHI-aims [14].

constants were determined by nine points fit of total energy per unit cell to the Vinet equation of state around the SCAN equilibrium unit cell volume ($V_0$) in a range of $V_0 \pm 10\%$ [208, 209].

Figure 5.7 compares LC20 results from ML models with the SCAN and SCAN-L functionals. The SCAN results for lattice constants are taken from Ref. [12] and SCAN-L results from Ref. [13]. The results show that the ML models do not perform as well for solids as they do for gas phase atoms and molecules, suggesting difficulty in generalizing knowledge into this untrained domain. The spin-scaled model preformed significantly better than the combined model both with and without enforcing the Lieb–Oxford bound. While the performance of ML models is poor compared to SCAN and SCAN-L, they improve slightly on the PBE GGA [32] (MAE 0.060Å). It has to be noted here that the ML calculations were obtained non self-consistently using PBE densities instead SCAN densities. This is because we found SCAN implementation to be numerically less stable in FHI-aims and showed convergence issues for certain systems. FHI-aims was used because we required all electron code and not pseudopotential to get usable input data for lattice constant calculations. The poor performance for the ML models could well be because we may have introduced density driven errors into the ML calculations as PBE densities are different to SCAN densities. Having said that, it suggests a similar conclusion to the molecular tests: that the spin-scaling and the Lieb–Oxford bound are insufficient to
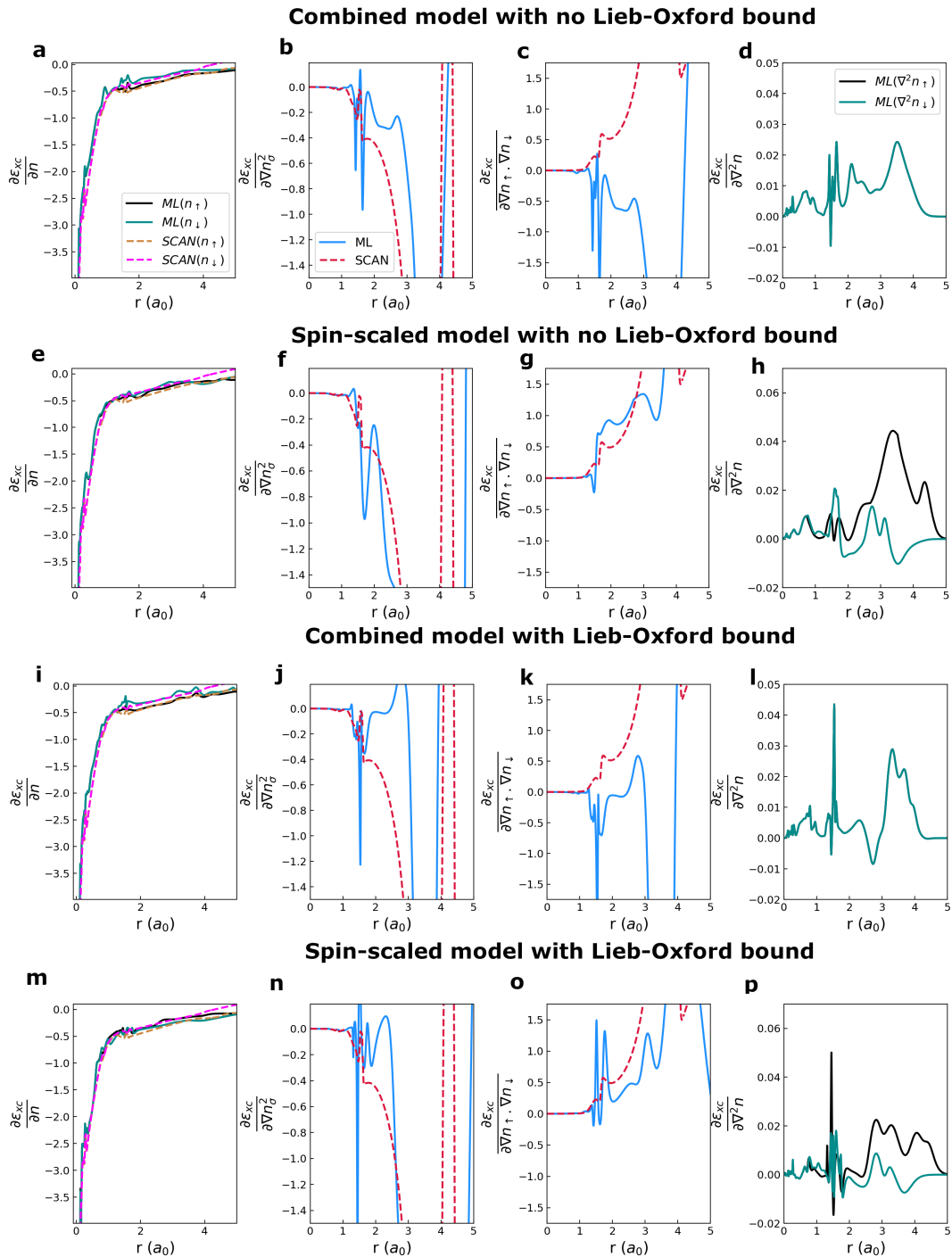
Figure 5.8: Derivatives of SCAN and ML model XC energy density (combined and spin-scaled) with respect to input ingredients for the silicon atom (not in training set). ML derivatives are represented by solid lines while SCAN are dotted.

transfer learning into the periodic systems. Inclusion of such information in the training set is likely necessary to improve model accuracy.

### 5.6.4 Exchange-correlation potential

The XC potential is defined as,

$$v_{\mathrm{xc}}(\mathbf{r}) = \frac{\delta E_{\mathrm{xc}}}{\delta n(\mathbf{r})}. \tag{5.43}$$

This is constructed for the ML models from the partial derivatives of the model with respect to its ingredients,

$$\left\{ \frac{\partial E_{\mathrm{xc}}^{\mathrm{ML}}}{\partial n(\mathbf{r})}, \frac{\partial E_{\mathrm{xc}}^{\mathrm{ML}}}{\partial |\nabla n(\mathbf{r})|}, \frac{\partial E_{\mathrm{xc}}^{\mathrm{ML}}}{\partial \nabla^2 n(\mathbf{r})} \right\}, \tag{5.44}$$

through repeated application of the chain rule. In practice this is achieved using the back-propagation mechanism of the machine learning framework [210]. Here the choice of the activation functions for the neuron layers is critically important for obtaining a smooth XC potential appropriate for SCF applications. When the activation functions are differentiated during back-propagation activation functions with discontinuous derivatives, such as the popular rectified linear unit (ReLu) [211], may introduce discontinuities into the XC potential that can harm SCF convergence and computational efficiency. We therefore used only smooth sigmoid, tanh and elu activation functions within the present models.

Figure 5.8 shows partial derivatives of the combined and spin-scaled models with respect to input ingredients, compared against the equivalent for the SCAN functional where they exist. Note that $\epsilon_{\mathrm{xc}}^{\mathrm{SCAN}}(n, |\nabla n|, \tau)$ and $\epsilon_{\mathrm{xc}}^{\mathrm{ML}}(n, |\nabla n|, \nabla^2 n)$ are necessarily different functions, even though $\epsilon_{\mathrm{xc}}^{\mathrm{ML}}$ has been trained to reproduce $\epsilon_{\mathrm{xc}}^{\mathrm{SCAN}}$. Hence, we should not expect their partial derivatives in $n$ and $|\nabla n|$ to match. Figure 5.8 (**a-d**) shows the combined model partial derivatives for the test silicon atom, while (**e-h**) shows the same for the spin-scaled model.

Figures 5.8 (**a**), (**e**), (**i**) and (**m**) show that the density partial derivative is comparable to SCAN for both models. Both models exhibit oscillations in this derivative, though these are less severe for the spin-scaled models than the combined models. Figures 5.8 (**b-c**) and (**j-k**) for the combined model without and with Lieb–Oxford bound constraint and (**f-g**) and (**n-o**) for spin-scaled model, again with and without Lieb–Oxford bound, show the partial derivatives with respect to the same spin and cross spin gradient components. While the combined model does not distinguish between different spins $\partial \epsilon_{\mathrm{xcML}}/\partial \nabla n_\sigma^2 = \partial \epsilon_{\mathrm{xcML}}/\partial \nabla n_\uparrow \cdot \nabla n_\downarrow$, the spin-scaled model is able to distinguish spin channels so the same-spin and cross-spin partial derivatives are different. Finally, Figures (**d**), (**h**), (**i**) and (**k**)show the Laplacian partial derivatives.

It is not clear to what degree the oscillations of the present partial derivatives may affect the SCF performance of the ML models without performing such calculations, which is beyond the scope of the present study. We can reasonably expect the smoother spin-scaled model to outperform the combined model in this regard however, as a result of the reduced oscillations seen in Figure 5.8. We note that the SCAN functional

is known to have problematic oscillations in its XC potential which reduce its computational efficiency but generally do not prevent SCF convergence [82, 84, 83, 85, 79]. The similarity between the ML and SCAN partial derivatives of Figure 5.8 therefore suggest that self-consistency can likely be reached, though this may be sensitive to the choice of starting guess orbitals if they are different from the converged orbitals used in training.

## 5.7   Conclusion

In summary, we explore how a philosophy of exact constraints and appropriate norms can be combined with ML techniques in functional design. We have shown a simple test of this idea as a de-orbitalization of the SCAN functional, using the density Laplacian, $\nabla^2 n(\mathbf{r})$, in place of kinetic energy density $\tau(\mathbf{r})$. Four ML functionals were developed, enforcing a spin-scaling constraint, the Lieb–Oxford bound, both, and neither. These models were trained using a dataset with no chemical bonding, preferring the "norms" appropriate for semi-local functionals [12]. The model satisfying both the spin-scaling constraint and the Lieb–Oxford bound generally achieved a more balanced performance accross the properties tested, though performance was worse than that achieved by the analytical SCAN-L deorbitalization. Given that model performance was generally improved when both constraints were imposed, it is reasonable to believe that engineering in further constraints can enhance robustness of the ML models out of the training domain.

# Bibliography

[1] S. Raghu, R. Thomale, and T. Geballe, "Optimal t c of cuprates: The role of screening and reservoir layers," *Physical Review B*, vol. 86, no. 9, p. 094506, 2012.

[2] M. Hücker, "Structural aspects of materials with static stripe order," *Physica C: Superconductivity*, vol. 481, pp. 3–14, 2012.

[3] J. W. Furness, Y. Zhang, C. Lane, I. G. Buda, B. Barbiellini, R. S. Markiewicz, A. Bansil, and J. Sun, "An accurate first-principles treatment of doping-dependent electronic structure of high-temperature cuprate superconductors," *Communications Physics*, vol. 1, no. 1, p. 11, 2018.

[4] S. Uchida, T. Ido, H. Takagi, T. Arima, Y. Tokura, and S. Tajima, "Optical spectra of $La_{2-x}Sr_xCuO_4$: Effect of carrier doping on the electronic structure of the $CuO_2$ plane," *Phys. Rev. B*, vol. 43, no. 10, p. 7942, 1991.

[5] Y. Li, J. Huang, L. Cao, J. Wu, and J. Fei, "Optical properties of $La_2CuO_4$ and $La_{2-x}Ca_xCuO_4$ crystallites in UV–vis–NIR region synthesized by sol–gel process," *Mater. Charact.*, vol. 64, pp. 36–42, 2012.

[6] M. Kastner, R. Birgeneau, G. Shirane, and Y. Endoh, "Magnetic, transport, and optical properties of monolayer copper oxides," *Rev. Mod. Phys.*, vol. 70, no. 3, p. 897, 1998.

[7] J. M. Tranquada, "Neutron scattering studies of antiferromagnetic correlations in cuprates," in *Handbook of High-Temperature Superconductivity*, pp. 257–298, Springer, Berlin, 2007.

[8] S. Urban, *Neural network architectures and activation functions: A gaussian process approach*. PhD thesis, Technische Universität München, 2018.

[9] E. Clementi and C. Roetti, "Roothaan-hartree-fock atomic wavefunctions: Basis functions and their coefficients for ground and certain excited states of neutral and ionized atoms, z 54," *Atomic data and nuclear data tables*, vol. 14, no. 3-4, pp. 177–478, 1974.

[10] T. Koga, K. Kanayama, S. Watanabe, and A. J. Thakkar, "Analytical hartree–fock wave functions subject to cusp and asymptotic constraints: He to xe, li+ to cs+, h- to i-," *International journal of quantum chemistry*, vol. 71, no. 6, pp. 491–497, 1999.

[11] J. W. Furness, A. D. Kaplan, J. Ning, J. P. Perdew, and J. Sun, "Construction of meta-gga functionals through restoration of exact constraint adherence to regularized scan functionals," *The Journal of Chemical Physics*, vol. 156, no. 3, p. 034109, 2022.

[12] J. Sun, A. Ruzsinszky, and J. P. Perdew, "Strongly constrained and appropriately normed semilocal density functional," *Physical review letters*, vol. 115, no. 3, p. 036402, 2015.

[13] D. Mejia-Rodriguez and S. Trickey, "Deorbitalized meta-gga exchange-correlation functionals in solids," *Physical Review B*, vol. 98, no. 11, p. 115161, 2018.

[14] V. Blum, R. Gehrke, F. Hanke, P. Havu, V. Havu, X. Ren, K. Reuter, and M. Scheffler, "Ab initio molecular simulations with numeric atom-centered orbitals," *Computer Physics Communications*, vol. 180, no. 11, pp. 2175–2196, 2009.

[15] L. A. Curtiss, K. Raghavachari, P. C. Redfern, and J. A. Pople, "Assessment of gaussian-3 and density functional theories for a larger experimental test set," *The Journal of Chemical Physics*, vol. 112, no. 17, pp. 7374–7383, 2000.

[16] T. Clark, J. Chandrasekhar, G. W. Spitznagel, and P. V. R. Schleyer, "Efficient diffuse function-augmented basis sets for anion calculations. iii. the 3-21+ g basis set for first-row elements, li–f," *Journal of Computational Chemistry*, vol. 4, no. 3, pp. 294–301, 1983.

[17] M. J. Frisch, J. A. Pople, and J. S. Binkley, "Self-consistent molecular orbital methods 25. supplementary functions for gaussian basis sets," *The Journal of chemical physics*, vol. 80, no. 7, pp. 3265–3269, 1984.

[18] A. QUEST, "rapid development platform for quantum electronic structure techniques," 2017.

[19] A. Szabo and N. Ostlund, "Modern quantum chemistry (revised first edition)," 1989.

[20] C. Singh, "Interactive learning tutorials on quantum mechanics," *American Journal of Physics*, vol. 76, no. 4, pp. 400–405, 2008.

[21] P. Hohenberg and W. Kohn, "Inhomogeneous electron gas," *Physical review*, vol. 136, no. 3B, p. B864, 1964.

[22] W. Kohn and L. J. Sham, "Self-consistent equations including exchange and correlation effects," *Physical review*, vol. 140, no. 4A, p. A1133, 1965.

[23] E. Schrödinger, "An undulatory theory of the mechanics of atoms and molecules," *Physical review*, vol. 28, no. 6, p. 1049, 1926.

[24] M. Born and R. Oppenheimer, "Zur quantentheorie der molekeln," *Annalen der physik*, vol. 389, no. 20, pp. 457–484, 1927.

[25] W. Koch and M. C. Holthausen, *A chemist's guide to density functional theory*. John Wiley & Sons, 2015.

[26] A. Szabo and N. S. Ostlund, *Modern quantum chemistry: introduction to advanced electronic structure theory*. Courier Corporation, 2012.

[27] M. Levy, "Electron densities in search of hamiltonians," *Physical Review A*, vol. 26, no. 3, p. 1200, 1982.

[28] E. H. Lieb, "Density functionals for coulomb systems," in *Inequalities*, pp. 269–303, Springer, 2002.

[29] T. L. Gilbert, "Hohenberg-kohn theorem for nonlocal external potentials," *Physical Review B*, vol. 12, no. 6, p. 2111, 1975.

[30] D. M. Ceperley and B. Alder, "Ground state of the electron gas by a stochastic method," *Physical Review Letters*, vol. 45, no. 7, p. 566, 1980.

[31] Y. Wang, J. P. Perdew, J. Chevary, L. Macdonald, and S. Vosko, "Exchange potentials in density-functional theory," *Physical Review A*, vol. 41, no. 1, p. 78, 1990.

[32] J. P. Perdew, K. Burke, and M. Ernzerhof, "Generalized gradient approximation made simple," *Physical review letters*, vol. 77, no. 18, p. 3865, 1996.

[33] J. P. Perdew, J. A. Chevary, S. H. Vosko, K. A. Jackson, M. R. Pederson, D. J. Singh, and C. Fiolhais, "Atoms, molecules, solids, and surfaces: Applications of the generalized gradient approximation for exchange and correlation," *Physical Review B*, vol. 46, no. 11, p. 6671, 1992.

[34] J. Sun, R. C. Remsing, Y. Zhang, Z. Sun, A. Ruzsinszky, H. Peng, Z. Yang, A. Paul, U. Waghmare, X. Wu, *et al.*, "Accurate first-principles structures and energies of diversely bonded systems from an efficient density functional," *Nat. Chem.*, vol. 8, no. 9, p. 831, 2016.

[35] M. G. Medvedev, I. S. Bushmarinov, J. Sun, J. P. Perdew, and K. A. Lyssenko, "Density functional theory is straying from the path toward the exact functional," *Science*, vol. 355, no. 6320, pp. 49–52, 2017.

[36] M. G. Medvedev, I. S. Bushmarinov, J. Sun, J. P. Perdew, and K. A. Lyssenko, "Response to comment on "density functional theory is straying from the path toward the exact functional"," *Science*, vol. 356, no. 6337, pp. 496–496, 2017.

[37] Y. Zhao and D. G. Truhlar, "A new local density functional for main-group thermochemistry, transition metal bonding, thermochemical kinetics, and noncovalent interactions," *The Journal of chemical physics*, vol. 125, no. 19, p. 194101, 2006.

[38] J. C. Snyder, M. Rupp, K. Hansen, K.-R. Müller, and K. Burke, "Finding density functionals with machine learning," *Physical review letters*, vol. 108, no. 25, p. 253002, 2012.

[39] J. C. Snyder, M. Rupp, K. Hansen, L. Blooston, K.-R. Müller, and K. Burke, "Orbital-free bond breaking via machine learning," *The Journal of chemical physics*, vol. 139, no. 22, p. 224104, 2013.

[40] F. Brockherde, L. Vogt, L. Li, M. E. Tuckerman, K. Burke, and K.-R. Müller, "Bypassing the kohn-sham equations with machine learning," *Nature communications*, vol. 8, no. 1, pp. 1–10, 2017.

[41] Q. Liu, J. Wang, P. Du, L. Hu, X. Zheng, and G. Chen, "Improving the performance of long-range-corrected exchange-correlation functional with an embedded neural network," *The Journal of Physical Chemistry A*, vol. 121, no. 38, pp. 7273–7281, 2017.

[42] R. Nagai, R. Akashi, S. Sasaki, and S. Tsuneyuki, "Neural-network kohn-sham exchange-correlation potential and its out-of-training transferability," *The Journal of chemical physics*, vol. 148, no. 24, p. 241737, 2018.

[43] J. Wellendorff, K. T. Lundgaard, A. Møgelhøj, V. Petzold, D. D. Landis, J. K. Nørskov, T. Bligaard, and K. W. Jacobsen, "Density functionals for surface science: Exchange-correlation model development with bayesian error estimation," *Physical Review B*, vol. 85, no. 23, p. 235149, 2012.

[44] L. Li, T. E. Baker, S. R. White, K. Burke, *et al.*, "Pure density functional for strong correlation and the thermodynamic limit from machine learning," *Physical Review B*, vol. 94, no. 24, p. 245129, 2016.

[45] J. Hollingsworth, L. Li, T. E. Baker, and K. Burke, "Can exact conditions improve machine-learned density functionals?," *The Journal of chemical physics*, vol. 148, no. 24, p. 241743, 2018.

[46] S. Dick and M. Fernandez-Serra, "Highly accurate and constrained density functional obtained with differentiable programming," *Physical Review B*, vol. 104, no. 16, p. L161109, 2021.

[47] R. Nagai, R. Akashi, and O. Sugino, "Machine-learning-based exchange correlation functional with physical asymptotic constraints," *Physical Review Research*, vol. 4, no. 1, p. 013106, 2022.

[48] A. Damascelli, Z. Hussain, and Z.-X. Shen, "Angle-resolved photoemission studies of the cuprate superconductors," *Reviews of modern physics*, vol. 75, no. 2, p. 473, 2003.

[49] J. C. Slater, "A simplification of the hartree-fock method," *Physical review*, vol. 81, no. 3, p. 385, 1951.

[50] A. D. Becke, "A new mixing of hartree–fock and local density-functional theories," *The Journal of chemical physics*, vol. 98, no. 2, pp. 1372–1377, 1993.

[51] A. V. Krukau, O. A. Vydrov, A. F. Izmaylov, and G. E. Scuseria, "Influence of the exchange screening parameter on the performance of screened hybrid functionals," *The Journal of chemical physics*, vol. 125, no. 22, p. 224106, 2006.

[52] J. Heyd, G. E. Scuseria, and M. Ernzerhof, "Hybrid functionals based on a screened coulomb potential," *The Journal of chemical physics*, vol. 118, no. 18, pp. 8207–8215, 2003.

[53] P.-S. Svendsen and U. von Barth, "Gradient expansion of the exchange energy from second-order density response theory," *Physical Review B*, vol. 54, no. 24, p. 17402, 1996.

[54] F. Avellaneda, C. Bustacara, J. P. Garzon, and E. Gonzalez, "Implementation of a molecular simulator based on a multiagent system," in *2006 IEEE/WIC/ACM International Conference on Intelligent Agent Technology*, pp. 117–120, IEEE, 2006.

[55] K. A. BRUECKNER *et al.*, "Correlation energy of an electron gas with a slowly varying high density," *Physical Review*, vol. 165, no. 1, p. 18, 1968.

[56] J. Tao, J. P. Perdew, V. N. Staroverov, and G. E. Scuseria, "Climbing the density functional ladder: Nonempirical meta–generalized gradient approximation designed for molecules and solids," *Physical Review Letters*, vol. 91, no. 14, p. 146401, 2003.

[57] J. P. Perdew, A. Ruzsinszky, G. I. Csonka, O. A. Vydrov, G. E. Scuseria, L. A. Constantin, X. Zhou, and K. Burke, "Restoring the density-gradient expansion for exchange in solids and surfaces," *Physical review letters*, vol. 100, no. 13, p. 136406, 2008.

[58] J. P. Perdew, A. Ruzsinszky, G. I. Csonka, L. A. Constantin, and J. Sun, "Workhorse Semilocal Density Functional for Condensed Matter Physics and Quantum Chemistry," *Phys. Rev. Lett.*, vol. 103, no. 2, p. 026403, 2009.

[59] A. Ruzsinszky, J. Sun, B. Xiao, and G. I. Csonka, "A meta-gga made free of the order of limits anomaly," *Journal of Chemical Theory and Computation*, vol. 8, no. 6, pp. 2078–2087, 2012.

[60] J. Sun, B. Xiao, and A. Ruzsinszky, "Communication: Effect of the orbital-overlap dependence in the meta generalized gradient approximation," 2012.

[61] J. Sun, R. Haunschild, B. Xiao, I. W. Bulik, G. E. Scuseria, and J. P. Perdew, "Semilocal and hybrid meta-generalized gradient approximations based on the understanding of the kinetic-energy-density dependence," *The Journal of Chemical Physics*, vol. 138, no. 4, p. 044113, 2013.

[62] J. Sun, J. P. Perdew, and A. Ruzsinszky, "Semilocal density functional obeying a strongly tightened bound for exchange," *Proceedings of the National Academy of Sciences*, vol. 112, no. 3, pp. 685–689, 2015.

[63] J. P. Perdew, A. Ruzsinszky, J. Sun, and K. Burke, "Gedanken densities and exact constraints in density functional theory," *The Journal of chemical physics*, vol. 140, no. 18, p. 18A533, 2014.

[64] A. Becke, "Hartree–fock exchange energy of an inhomogeneous electron gas," *International journal of quantum chemistry*, vol. 23, no. 6, pp. 1915–1922, 1983.

[65] G. Oliver and J. Perdew, "Spin-density gradient expansion for the kinetic energy," *Physical Review A*, vol. 20, no. 2, p. 397, 1979.

[66] M. Levy and J. P. Perdew, "Hellmann-feynman, virial, and scaling requisites for the exact universal density functionals. shape of the correlation potential and diamagnetic susceptibility for atoms," *Physical Review A*, vol. 32, no. 4, p. 2010, 1985.

[67] L. Pollack and J. Perdew, "Evaluating density functional performance for the quasi-two-dimensional electron gas," *Journal of Physics: Condensed Matter*, vol. 12, no. 7, p. 1239, 2000.

[68] J. P. Perdew and Y. Wang, "Accurate and simple analytic representation of the electron-gas correlation energy," *Phys. Rev. B*, vol. 45, no. 23, p. 13244, 1992.

[69] E. H. Lieb and S. Oxford, "Improved lower bound on the indirect coulomb energy," *International Journal of Quantum Chemistry*, vol. 19, no. 3, pp. 427–439, 1981.

[70] M. Seidl, J. P. Perdew, and S. Kurth, "Simulation of all-order density-functional perturbation theory, using the second order and the strong-correlation limit," *Physical review letters*, vol. 84, no. 22, p. 5070, 2000.

[71] J. Tao, J. P. Perdew, L. M. Almeida, C. Fiolhais, and S. Kümmel, "Nonempirical density functionals investigated for jellium: Spin-polarized surfaces, spherical clusters, and bulk linear response," *Physical Review B*, vol. 77, no. 24, p. 245107, 2008.

[72] P. Jurečka, J. Šponer, J. Černỳ, and P. Hobza, "Benchmark database of accurate (mp2 and ccsd (t) complete basis set limit) interaction energies of small model complexes, dna base pairs, and amino acid pairs," *Physical Chemistry Chemical Physics*, vol. 8, no. 17, pp. 1985–1993, 2006.

[73] D. Mejía-Rodríguez and S. Trickey, "Analysis of over-magnetization of elemental transition metal solids from the scan density functional," *Physical Review B*, vol. 100, no. 4, p. 041113, 2019.

[74] J. P. Perdew, K. Burke, and Y. Wang, "Erratum: Generalized gradient approximation for the exchange-correlation hole of a many-electron system [phys. rev. b 54, 16 533 (1996)]," *Physical Review B*, vol. 57, no. 23, p. 14999, 1998.

[75] L. A. Constantin, J. P. Perdew, and J. Tao, "Meta-generalized gradient approximation for the exchange-correlation hole with an application to the jellium surface energy," *Physical Review B*, vol. 73, no. 20, p. 205104, 2006.

[76] J. Tao and Y. Mo, "Accurate semilocal density functional for condensed-matter physics and quantum chemistry," *Physical Review Letters*, vol. 117, no. 7, p. 073001, 2016.

[77] S. Jana, A. Patra, and P. Samal, "Assessing the performance of the tao-mo semilocal density functional in the projector-augmented-wave method," *The Journal of Chemical Physics*, vol. 149, no. 4, p. 044120, 2018.

[78] S. Jana, K. Sharma, and P. Samal, "Improving the performance of tao–mo non-empirical density functional with broader applicability in quantum chemistry and materials science," *The Journal of Physical Chemistry A*, vol. 123, no. 29, pp. 6356–6369, 2019.

[79] J. W. Furness, A. D. Kaplan, J. Ning, J. P. Perdew, and J. Sun, "Accurate and Numerically Efficient r$^2$SCAN Meta-Generalized Gradient Approximation," *J. Phys. Chem. Lett.*, vol. 11, no. 19, pp. 8208–8215, 2020.

[80] A. Patra, S. Jana, and P. Samal, "A way of resolving the order-of-limit problem of tao–mo semilocal functional," *The Journal of Chemical Physics*, vol. 153, no. 18, p. 184112, 2020.

[81] T. Aschebrock and S. Kümmel, "Ultranonlocality and accurate band gaps from a meta-generalized gradient approximation," *Physical Review Research*, vol. 1, no. 3, p. 033082, 2019.

[82] Z.-h. Yang, H. Peng, J. Sun, and J. P. Perdew, "More realistic band gaps from meta-generalized gradient approximations: Only in a generalized Kohn-Sham scheme," *Phys. Rev. B*, vol. 93, no. 20, p. 205205, 2016.

[83] Y. Yamamoto, C. M. Diaz, L. Basurto, K. A. Jackson, T. Baruah, and R. R. Zope, "Fermi-löwdin orbital self-interaction correction using the strongly constrained and appropriately normed meta-gga functional," *The Journal of chemical physics*, vol. 151, no. 15, p. 154105, 2019.

[84] Y. Yao and Y. Kanai, "Plane-wave pseudopotential implementation and performance of scan meta-gga exchange-correlation functional for extended systems," *The Journal of Chemical Physics*, vol. 146, no. 22, p. 224105, 2017.

[85] A. P. Bartók and J. R. Yates, "Response to "Comment on 'Regularized SCAN functional'"[J. Chem. Phys. 151, 207101 (2019)]," *J. Chem. Phys.*, vol. 151, no. 20, p. 207102, 2019.

[86] D. Mejía-Rodríguez and S. Trickey, "Comment on "Regularized SCAN functional"[J. Chem. Phys. 150, 161101 (2019)]," *J. Chem. Phys.*, vol. 151, no. 20, p. 207101, 2019.

[87] D. Mejía-Rodríguez and S. Trickey, "Spin-Crossover from a Well-Behaved, Low-Cost meta-GGA Density Functional," *J. Phys. Chem. A*, vol. 124, no. 47, pp. 9889–9894, 2020.

[88] A. Görling and M. Levy, "Exact kohn-sham scheme based on perturbation theory," *Physical Review A*, vol. 50, no. 1, p. 196, 1994.

[89] Q. Wu and W. Yang, "Algebraic equation and iterative optimization for the optimized effective potential in density functional theory," *Journal of Theoretical and Computational Chemistry*, vol. 2, no. 04, pp. 627–638, 2003.

[90] A. Seidl, A. Görling, P. Vogl, J. A. Majewski, and M. Levy, "Generalized kohn-sham schemes and the band-gap problem," *Physical Review B*, vol. 53, no. 7, p. 3764, 1996.

[91] R. Neumann, R. H. Nobes, and N. C. Handy, "Exchange functionals and potentials," *Molecular Physics*, vol. 87, no. 1, pp. 1–36, 1996.

[92] Q. Wu and W. Yang, "A direct optimization method for calculating density functionals and exchange–correlation potentials from electron densities," *The Journal of chemical physics*, vol. 118, no. 6, pp. 2498–2509, 2003.

[93] D. Mejia-Rodriguez and S. Trickey, "Deorbitalization strategies for meta-generalized-gradient-approximation exchange-correlation functionals," *Physical Review A*, vol. 96, no. 5, p. 052512, 2017.

[94] D. Mejía-Rodríguez and S. Trickey, "Meta-GGA performance in solids at almost GGA cost," *Phys. Rev. B*, vol. 102, no. 12, p. 121109, 2020.

[95] J. P. Perdew and L. A. Constantin, "Laplacian-level density functionals for the kinetic energy density and exchange-correlation energy," *Physical Review B*, vol. 75, no. 15, p. 155109, 2007.

[96] A. D. Kaplan and J. P. Perdew, "Improved laplacian-level meta-gga for the weakly-nonlocal solid metals," *arXiv preprint arXiv:2203.09403*, 2022.

[97] P. H. Meijer, "Kamerlingh onnes and the discovery of superconductivity," *American Journal of Physics*, vol. 62, no. 12, pp. 1105–1108, 1994.

[98] W. Meissner and R. Ochsenfeld, "Ein neuer effekt bei eintritt der supraleitfähigkeit," *Naturwissenschaften*, vol. 21, no. 44, pp. 787–788, 1933.

[99] J. Bardeen, L. N. Cooper, and J. R. Schrieffer, "Microscopic theory of superconductivity," *Physical Review*, vol. 106, no. 1, p. 162, 1957.

[100] J. G. Bednorz and K. A. Müller, "Possible hight c superconductivity in the ba- la- cu- o system," *Zeitschrift für Physik B Condensed Matter*, vol. 64, no. 2, pp. 189–193, 1986.

[101] M.-K. Wu, J. R. Ashburn, C. Torng, P. H. Hor, R. L. Meng, L. Gao, Z. J. Huang, Y. Wang, and a. Chu, "Superconductivity at 93 k in a new mixed-phase y-ba-cu-o compound system at ambient pressure," *Physical review letters*, vol. 58, no. 9, p. 908, 1987.

[102] W. E. Pickett, "Electronic structure of the high-temperature oxide superconductors," *Reviews of Modern Physics*, vol. 61, no. 2, p. 433, 1989.

[103] L. Mattheiss, "Electronic band properties and superconductivity in la 2- y x y cuo 4," *Physical review letters*, vol. 58, no. 10, p. 1028, 1987.

[104] J. P. Perdew and A. Zunger, "Self-interaction correction to density-functional approximations for many-electron systems," *Physical Review B*, vol. 23, no. 10, p. 5048, 1981.

[105] D. Singh and W. Pickett, "Gradient-corrected density-functional studies of cacuo 2," *Physical Review B*, vol. 44, no. 14, p. 7715, 1991.

[106] A. D. Becke, "Density-functional exchange-energy approximation with correct asymptotic behavior," *Physical review A*, vol. 38, no. 6, p. 3098, 1988.

[107] C. Lee, W. Yang, and R. G. Parr, "Development of the colle-salvetti correlation-energy formula into a functional of the electron density," *Physical review B*, vol. 37, no. 2, p. 785, 1988.

[108] P. Stephens, F. Devlin, C. Chabalowski, and M. J. Frisch, "Ab initio calculation of vibrational absorption and circular dichroism spectra using density functional force fields," *The Journal of Physical Chemistry*, vol. 98, no. 45, pp. 11623–11627, 1994.

[109] J. K. Perry, J. Tahir-Kheli, and W. A. Goddard III, "Ab initio evidence for the formation of impurity d 3 z 2- r 2 holes in doped la 2- x sr x cuo 4," *Physical Review B*, vol. 65, no. 14, p. 144501, 2002.

[110] L. K. Wagner and P. Abbamonte, "Effect of electron correlation on the electronic structure and spin-lattice coupling of high-$T_c$ cuprates: Quantum Monte Carlo calculations," *Phys. Rev. B*, vol. 90, no. 12, p. 125129, 2014.

[111] M. Czyżyk and G. Sawatzky, "Local-density functional and on-site correlations: The electronic structure of $La_2CuO_4$ and $LaCuO_3$," *Phys. Rev. B*, vol. 49, no. 20, p. 14211, 1994.

[112] S. Pesant and M. Côté, "DFT+ $U$ study of magnetic order in doped $La_2CuO_4$ crystals," *Phys. Rev. B*, vol. 84, no. 8, p. 085104, 2011.

[113] G. Kotliar, S. Y. Savrasov, K. Haule, V. S. Oudovenko, O. Parcollet, and C. Marianetti, "Electronic structure calculations with dynamical mean-field theory," *Rev. Mod. Phys.*, vol. 78, no. 3, p. 865, 2006.

[114] K. Held, I. Nekrasov, G. Keller, V. Eyert, N. Blümer, A. McMahan, R. Scalettar, T. Pruschke, V. Anisimov, and D. Vollhardt, "Realistic investigations of correlated electron systems with LDA+ DMFT," *Phys. Status Solidi B*, vol. 243, no. 11, pp. 2599–2631, 2006.

[115] H. Park, K. Haule, and G. Kotliar, "Cluster Dynamical Mean Field Theory of the Mott Transition," *Phys. Rev. Lett.*, vol. 101, no. 18, p. 186403, 2008.

[116] C. Lane, J. W. Furness, I. G. Buda, Y. Zhang, R. S. Markiewicz, B. Barbiellini, J. Sun, and A. Bansil, "Antiferromagnetic ground state of la 2 cuo 4: A parameter-free ab initio description," *Physical Review B*, vol. 98, no. 12, p. 125140, 2018.

[117] Y. Zhang, C. Lane, J. W. Furness, B. Barbiellini, J. P. Perdew, R. S. Markiewicz, A. Bansil, and J. Sun, "Competing stripe and magnetic phases in the cuprates from first principles," *Proc. Natl. Acad. Sci. U.S.A.*, vol. 117, no. 1, pp. 68–72, 2020.

[118] C. Lane, Y. Zhang, J. W. Furness, R. S. Markiewicz, B. Barbiellini, J. Sun, and A. Bansil, "First-principles calculation of spin and orbital contributions to magnetically ordered moments in $Sr_2IrO_4$," *Phys. Rev. B*, vol. 101, no. 15, p. 155110, 2020.

[119] E. B. Isaacs and C. Wolverton, "Performance of the strongly constrained and appropriately normed density functional for solid-state materials," *Phys. Rev. Materials*, vol. 2, no. 6, p. 063801, 2018.

[120] M. Ekholm, D. Gambino, H. J. M. Jönsson, F. Tasnádi, B. Alling, and I. A. Abrikosov, "Assessing the SCAN functional for itinerant electron ferromagnets," *Phys. Rev. B*, vol. 98, no. 9, p. 094413, 2018.

[121] Y. Fu and D. J. Singh, "Applicability of the Strongly Constrained and Appropriately Normed Density Functional to Transition-Metal Magnetism," *Phys. Rev. Lett.*, vol. 121, no. 20, p. 207201, 2018.

[122] J. W. Furness and J. Sun, "Enhancing the efficiency of density functionals with an improved iso-orbital indicator," *Phys. Rev. B*, vol. 99, no. 4, p. 041119, 2019.

[123] A. P. Bartók and J. R. Yates, "Regularized SCAN functional," *J. Chem. Phys.*, vol. 150, no. 16, p. 161101, 2019.

[124] R. O. Jones and O. Gunnarsson, "The density functional formalism, its applications and prospects," *Rev. Mod. Phys.*, vol. 61, no. 3, p. 689, 1989.

[125] J. Heyd, "Hybrid functionals based on a screened Coulomb potential," *J. Chem. Phys.*, vol. 124, p. 219906, 2006.

[126] J. Heyd, J. E. Peralta, G. E. Scuseria, and R. L. Martin, "Energy band gaps and lattice parameters evaluated with the Heyd-Scuseria-Ernzerhof screened hybrid functional," *J. Chem. Phys.*, vol. 123, no. 17, p. 174101, 2005.

[127] J. Heyd, "Efficient hybrid density functional calculations in solids: Assessment of the Heyd–Scuseria–Ernzerhof screened Coulomb hybrid functional," *J. Chem. Phys.*, vol. 121, p. 1187, 2004.

[128] J. E. Peralta, J. Heyd, G. E. Scuseria, and R. L. Martin, "Spin-orbit splittings and energy band gaps calculated with the Heyd-Scuseria-Ernzerhof screened hybrid functional," *Phys. Rev. B*, vol. 74, no. 7, p. 073101, 2006.

[129] J. P. Perdew, K. Schmidt, *et al.*, "Density functional theory and its application to materials," pp. 1–20, American Institute of Physics, 2001.

[130] G. Kresse and D. Joubert, "From ultrasoft pseudopotentials to the projector augmented-wave method," *Physical review b*, vol. 59, no. 3, p. 1758, 1999.

[131] G. Kresse and J. Furthmüller, "Efficient iterative schemes for ab initio total-energy calculations using a plane-wave basis set," *Physical review B*, vol. 54, no. 16, p. 11169, 1996.

[132] G. Kresse and J. Hafner, "Ab initio molecular dynamics for open-shell transition metals," *Physical Review B*, vol. 48, no. 17, p. 13115, 1993.

[133] A. Suter, G. Logvenov, A. Boris, F. Baiutti, F. Wrobel, L. Howald, E. Stilp, Z. Salman, T. Prokscha, and B. Keimer, "Superconductivity drives magnetism in $\delta$-doped la 2 cuo 4," *Physical Review B*, vol. 97, no. 13, p. 134522, 2018.

[134] D. Vaknin, S. Sinha, D. Moncton, D. Johnston, J. Newsam, C. Safinya, and H. King Jr, "Antiferromagnetism in la 2 cuo 4- y," *Physical review letters*, vol. 58, no. 26, p. 2802, 1987.

[135] T. Freltoft, G. Shirane, S. Mitsuda, J. Remeika, and A. Cooper, "Magnetic form factor of cu in la 2 cu o 4," *Physical Review B*, vol. 37, no. 1, p. 137, 1988.

[136] I. Askerzade, "Physical properties of unconventional superconductors," in *Unconventional Superconductors*, pp. 1–26, Springer, 2012.

[137] J. Tranquada, B. Sternlieb, J. Axe, Y. Nakamura, and S. Uchida, "Evidence for stripe correlations of spins and holes in copper oxide superconductors," *nature*, vol. 375, no. 6532, p. 561, 1995.

[138] J. Jorgensen, B. Dabrowski, S. Pei, D. Hinks, L. Soderholm, B. Morosin, J. Schirber, E. Venturini, and D. Ginley, "Superconducting phase of la 2 cu o 4+ $\delta$: A superconducting composition resulting from phase separation," *Physical Review B*, vol. 38, no. 16, p. 11337, 1988.

[139] D. Cox, P. Zolliker, J. Axe, A. Moudden, A. Moodenbaugh, and Y. Xu, "Structural studies of la 2- x ba x cuo 4 between 11–293 k," *MRS Online Proceedings Library Archive*, vol. 156, 1989.

[140] S. A. Wolf and V. Z. Kresin, "Novel superconductivity," Springer Science & Business Media, 2012.

[141] Y. Zhang, J. Sun, J. P. Perdew, and X. Wu, "Comparative first-principles studies of prototypical ferroelectric materials by LDA, GGA, and SCAN meta-GGA," *Phys. Rev. B*, vol. 96, no. 3, p. 035143, 2017.

[142] S. Ono, S. Komiya, and Y. Ando, "Strong charge fluctuations manifested in the high-temperature Hall coefficient of high-$T_c$ cuprates," *Phys. Rev. B*, vol. 75, no. 2, p. 024515, 2007.

[143] A. J. Cohen, P. Mori-Sánchez, and W. Yang, "Fractional charge perspective on the band gap in density-functional theory," *Phys. Rev. B*, vol. 77, no. 11, p. 115123, 2008.

[144] P. Mori-Sánchez, A. J. Cohen, and W. Yang, "Localization and Delocalization Errors in Density Functional Theory and Implications for Band-Gap Prediction," *Phys. Rev. Lett.*, vol. 100, no. 14, p. 146401, 2008.

[145] J. P. Perdew, W. Yang, K. Burke, Z. Yang, E. K. Gross, M. Scheffler, G. E. Scuseria, T. M. Henderson, I. Y. Zhang, A. Ruzsinszky, *et al.*, "Understanding band gaps of solids in generalized kohn–sham theory," *Proceedings of the National Academy of Sciences*, vol. 114, no. 11, pp. 2801–2806, 2017.

[146] Y. Zhang, J. Furness, R. Zhang, Z. Wang, A. Zunger, and J. Sun, "Symmetry-breaking polymorphous descriptions for correlated materials without interelectronic U," *Phys. Rev. B*, vol. 102, no. 4, p. 045112, 2020.

[147] A. Auerbach, *Interacting electrons and quantum magnetism.* Springer Science & Business Media, 2012.

[148] J. P. Perdew, A. Ruzsinszky, J. Sun, N. K. Nepal, and A. D. Kaplan, "Interpretations of ground-state symmetry breaking and strong correlation in wavefunction and density functional theories," *Proc. Natl. Acad. Sci. U.S.A.*, vol. 118, no. 4, 2021.

[149] R. Markiewicz, I. Buda, P. Mistark, C. Lane, and A. Bansil, "Entropic Origin of Pseudogap Physics and a Mott-Slater Transition in Cuprates," *Sci. Rep.*, vol. 7, p. 44008, 2017.

[150] A. M. Oleś, "Antiferromagnetism and correlation of electrons in transition metals," *Phys. Rev. B*, vol. 28, no. 1, p. 327, 1983.

[151] S. W. Jang, H. Sakakibara, H. Kino, T. Kotani, K. Kuroki, and M. J. Han, "Direct theoretical evidence for weaker correlations in electron-doped and Hg-based hole-doped cuprates," *Sci. Rep.*, vol. 6, p. 33397, 2016.

[152] Y.-S. Su, T. Kaplan, S. Mahanti, and J. Harrison, "Crystal Haartree-Faock calculations for $La_2NiO_4$ and $La_2CuO_4$," *Phys. Rev. B*, vol. 59, no. 16, p. 10521, 1999.

[153] D. Coffey, K. Bedell, and S. Trugman, "Effective spin Hamiltonian for the CuO planes in $La_2CuO_4$ and metamagnetism," *Phys. Rev. B*, vol. 42, no. 10, p. 6509, 1990.

[154] L. Noodleman, "Valence bond description of antiferromagnetic coupling in transition metal dimers," *J. Chem. Phys.*, vol. 74, no. 10, pp. 5737–5743, 1981.

[155] P. Bourges, H. Casalta, A. Ivanov, and D. Petitgrand, "Superexchange Coupling and Spin Susceptibility Spectral Weight in Undoped Monolayer Cuprates," *Phys. Rev. Lett.*, vol. 79, no. 24, p. 4906, 1997.

[156] S. Hayden, G. Aeppli, R. Osborn, A. Taylor, T. Perring, S. Cheong, and Z. Fisk, "High-energy spin waves in $La_2CuO_4$," *Phys. Rev. Lett.*, vol. 67, no. 25, p. 3622, 1991.

[157] R. Coldea, S. Hayden, G. Aeppli, T. Perring, C. Frost, T. Mason, S.-W. Cheong, and Z. Fisk, "Spin Waves and Electronic Interactions in $La_2CuO_4$," *Phys. Rev. Lett.*, vol. 86, no. 23, p. 5377, 2001.

[158] A. Botana and M. Norman, "Similarities and Differences between $LaNiO_2$ and $CaCuO_2$ and implications for Superconductivity," *Phys. Rev. X*, vol. 10, no. 1, p. 011024, 2020.

[159] S. W. Jang, T. Kotani, H. Kino, K. Kuroki, and M. J. Han, "Quasiparticle self-consistent GW study of cuprates: electronic structure, model parameters and the two-band theory for $T_c$," *Sci. Rep.*, vol. 5, no. 1, pp. 1–10, 2015.

[160] D. Khomskii, *Transition metal compounds.* Cambridge University Press, 2014.

[161] J. H. de Boer and E. J. Verwey, "Semi-conductors with partially and with completely filled 3d-lattice bands," *Proceedings of the Physical Society (1926-1948)*, vol. 49, no. 4S, p. 59, 1937.

[162] K. Pokharel, C. Lane, J. W. Furness, R. Zhang, J. Ning, B. Barbiellini, R. S. Markiewicz, Y. Zhang, A. Bansil, and J. Sun, "Sensitivity of the electronic and magnetic structures of cuprate superconductors to density functional approximations," *npj Computational Materials*, vol. 8, no. 1, pp. 1–11, 2022.

[163] J. W. Furness, A. D. Kaplan, J. Ning, J. P. Perdew, and J. Sun, "Construction of meta-gga functionals through restoration of exact constraint adherence to regularized scan functionals," *arXiv preprint arXiv:2110.00647*, 2021.

[164] S. Lany, "Band-structure calculations for the 3 d transition metal oxides in g w," *Physical Review B*, vol. 87, no. 8, p. 085112, 2013.

[165] A. Schrön, C. Rödl, and F. Bechstedt, "Crystalline and magnetic anisotropy of the 3 d-transition metal monoxides mno, feo, coo, and nio," *Physical Review B*, vol. 86, no. 11, p. 115134, 2012.

[166] J. P. Perdew, R. G. Parr, M. Levy, and J. L. Balduz Jr, "Density-functional theory for fractional particle number: derivative discontinuities of the energy," *Physical Review Letters*, vol. 49, no. 23, p. 1691, 1982.

[167] A. Zunger and A. Freeman, "Ground-and excited-state properties of lif in the local-density formalism," *Physical Review B*, vol. 16, no. 6, p. 2901, 1977.

[168] Y. Zhang, J. W. Furness, B. Xiao, and J. Sun, "Subtlety of tio2 phase stability: Reliability of the density functional theory predictions and persistence of the self-interaction error," *The Journal of chemical physics*, vol. 150, no. 1, p. 014105, 2019.

[169] A. J. Cohen, P. Mori-Sánchez, and W. Yang, "Insights into current limitations of density functional theory," *Science*, vol. 321, no. 5890, pp. 792–794, 2008.

[170] M. R. Pederson, A. Ruzsinszky, and J. P. Perdew, "Communication: Self-interaction correction with unitary invariance in density functional theory," *The Journal of Chemical Physics*, vol. 140, no. 12, p. 121103, 2014.

[171] C. Li, X. Zheng, N. Q. Su, and W. Yang, "Localized orbital scaling correction for systematic elimination of delocalization error in density functional approximations," *National Science Review*, vol. 5, no. 2, pp. 203–215, 2018.

[172] C. Shahi, P. Bhattarai, K. Wagle, B. Santra, S. Schwalbe, T. Hahn, J. Kortus, K. A. Jackson, J. E. Peralta, K. Trepte, *et al.*, "Stretched or noded orbital densities and self-interaction correction in density functional theory," *The Journal of Chemical Physics*, vol. 150, no. 17, p. 174102, 2019.

[173] V. I. Anisimov, F. Aryasetiawan, and A. Lichtenstein, "First-principles calculations of the electronic structure and spectra of strongly correlated systems: the lda+ u method," *Journal of Physics: Condensed Matter*, vol. 9, no. 4, p. 767, 1997.

[174] V. Nair and G. E. Hinton, "Rectified linear units improve restricted boltzmann machines," in *Icml*, 2010.

[175] A. Krizhevsky, I. Sutskever, and G. E. Hinton, "Imagenet classification with deep convolutional neural networks," *Advances in neural information processing systems*, vol. 25, 2012.

[176] A. L. Maas, A. Y. Hannun, A. Y. Ng, *et al.*, "Rectifier nonlinearities improve neural network acoustic models," in *Proc. icml*, vol. 30, p. 3, Citeseer, 2013.

[177] K. He, X. Zhang, S. Ren, and J. Sun, "Delving deep into rectifiers: Surpassing human-level performance on imagenet classification," in *Proceedings of the IEEE international conference on computer vision*, pp. 1026–1034, 2015.

[178] Y. LeCun, D. Touresky, G. Hinton, and T. Sejnowski, "A theoretical framework for back-propagation," in *Proceedings of the 1988 connectionist models summer school*, vol. 1, pp. 21–28, 1988.

[179] J. P. Perdew and K. Schmidt, "Jacob's ladder of density functional approximations for the exchange-correlation energy," in *AIP Conference Proceedings*, vol. 577, pp. 1–20, American Institute of Physics, 2001.

[180] J. Sun, B. Xiao, Y. Fang, R. Haunschild, P. Hao, A. Ruzsinszky, G. I. Csonka, G. E. Scuseria, and J. P. Perdew, "Density functionals that recognize covalent, metallic, and weak bonds," *Physical review letters*, vol. 111, no. 10, p. 106401, 2013.

[181] A. D. Becke, "A new inhomogeneity parameter in density-functional theory," *The Journal of chemical physics*, vol. 109, no. 6, pp. 2092–2098, 1998.

[182] F. Della Sala, E. Fabiano, and L. A. Constantin, "Kinetic-energy-density dependent semilocal exchange-correlation functionals," *International Journal of Quantum Chemistry*, vol. 116, no. 22, pp. 1641–1694, 2016.

[183] M. Dorigo and U. Schnepf, "Genetics-based machine learning and behavior-based robotics: a new synthesis," *IEEE Transactions on Systems, Man, and Cybernetics*, vol. 23, no. 1, pp. 141–154, 1993.

[184] M. A. Salichs, R. Barber, A. M. Khamis, M. Malfaz, J. F. Gorostiza, R. Pacheco, R. Rivas, A. Corrales, E. Delgado, and D. Garcia, "Maggie: A robotic platform for human-robot social interaction," in *2006 IEEE conference on robotics, automation and mechatronics*, pp. 1–7, IEEE, 2006.

[185] N. MacLeod, M. Benfield, and P. Culverhouse, "Time to automate identification," *Nature*, vol. 467, no. 7312, pp. 154–155, 2010.

[186] L. Chittka and A. Dyer, "Your face looks familiar," *Nature*, vol. 481, no. 7380, pp. 154–155, 2012.

[187] E. A. Ashley, "The precision medicine initiative: a new national effort," *Jama*, vol. 313, no. 21, pp. 2119–2120, 2015.

[188] M. C. Schatz and B. Langmead, "The dna data deluge," *Ieee Spectrum*, vol. 50, no. 7, pp. 28–33, 2013.

[189] H. Ding, I. Takigawa, H. Mamitsuka, and S. Zhu, "Similarity-based machine learning methods for predicting drug–target interactions: a brief review," *Briefings in bioinformatics*, vol. 15, no. 5, pp. 734–747, 2014.

[190] D. Silver, A. Huang, C. J. Maddison, A. Guez, L. Sifre, G. Van Den Driessche, J. Schrittwieser, I. Antonoglou, V. Panneershelvam, M. Lanctot, *et al.*, "Mastering the game of go with deep neural networks and tree search," *nature*, vol. 529, no. 7587, pp. 484–489, 2016.

[191] J. Westermayr, M. Gastegger, K. T. Schütt, and R. J. Maurer, "Perspective on integrating machine learning into computational chemistry and materials science," *arXiv preprint arXiv:2102.08435*, 2021.

[192] M. Chen, H.-Y. Ko, R. C. Remsing, M. F. C. Andrade, B. Santra, Z. Sun, A. Selloni, R. Car, M. L. Klein, J. P. Perdew, *et al.*, "Ab initio theory and modeling of water," *Proceedings of the National Academy of Sciences*, vol. 114, no. 41, pp. 10846–10851, 2017.

[193] R. C. Remsing, M. L. Klein, and J. Sun, "Dependence of the structure and dynamics of liquid silicon on the choice of density functional approximation," *Physical Review B*, vol. 96, no. 2, p. 024203, 2017.

[194] G. S. Gautam and E. A. Carter, "Evaluating transition metal oxides within dft-scan and scan+ u frameworks for solar thermochemical applications," *Physical Review Materials*, vol. 2, no. 9, p. 095401, 2018.

[195] K. Pokharel, C. Lane, J. W. Furness, R. Zhang, J. Ning, B. Barbiellini, R. S. Markiewicz, Y. Zhang, A. Bansil, and J. Sun, "Sensitivity of the electronic and magnetic structures of high-temperature cuprate superconductors to exchange-correlation density functionals," *arXiv preprint arXiv:2004.08047*, 2020.

[196] J. Kirkpatrick, B. McMorrow, D. H. Turban, A. L. Gaunt, J. S. Spencer, A. G. Matthews, A. Obika, L. Thiry, M. Fortunato, D. Pfau, *et al.*, "Pushing the frontiers of density functionals by solving the fractional electron problem," *Science*, vol. 374, no. 6573, pp. 1385–1389, 2021.

[197] J. P. Perdew and Y. Wang, "Erratum: Accurate and simple analytic representation of the electron-gas correlation energy [phys. rev. b 45, 13244 (1992)]," *Physical Review B*, vol. 98, no. 7, p. 079904, 2018.

[198] J. P. Perdew, P. Ziesche, and H. Eschrig, "Electronic structure of solids' 91," 1991.

[199] B. L. Kalman and S. C. Kwasny, "Why tanh: choosing a sigmoidal function," in *[Proceedings 1992] IJCNN International Joint Conference on Neural Networks*, vol. 4, pp. 578–581, IEEE, 1992.

[200] L. Almeida, J. P. Perdew, and C. Fiolhais, "Surface and curvature energies from jellium spheres: Density functional hierarchy and quantum monte carlo," *Physical Review B*, vol. 66, no. 7, p. 075115, 2002.

[201] B. Wood, N. Hine, W. Foulkes, and P. García-González, "Quantum monte carlo calculations of the surface energy of an electron gas," *Physical Review B*, vol. 76, no. 3, p. 035403, 2007.

[202] M. Abadi, P. Barham, J. Chen, Z. Chen, A. Davis, J. Dean, M. Devin, S. Ghemawat, G. Irving, M. Isard, *et al.*, "Tensorflow: A system for large-scale machine learning," in *12th {USENIX} symposium on operating systems design and implementation ({OSDI} 16)*, pp. 265–283, 2016.

[203] J. Han and C. Moraga, "The influence of the sigmoid function parameters on the speed of backpropagation learning," in *International Workshop on Artificial Neural Networks*, pp. 195–201, Springer, 1995.

[204] D.-A. Clevert, T. Unterthiner, and S. Hochreiter, "Fast and accurate deep network learning by exponential linear units (elus)," *arXiv preprint arXiv:1511.07289*, 2015.

[205] F. Pedregosa, G. Varoquaux, A. Gramfort, V. Michel, B. Thirion, O. Grisel, M. Blondel, P. Prettenhofer, R. Weiss, V. Dubourg, J. Vanderplas, A. Passos, D. Cournapeau, M. Brucher, M. Perrot, and E. Duchesnay, "Scikit-learn: Machine learning in Python," *Journal of Machine Learning Research*, vol. 12, pp. 2825–2830, 2011.

[206] D. P. Kingma and J. Ba, "Adam: A method for stochastic optimization," *arXiv preprint arXiv:1412.6980*, 2014.

[207] J. Sun, M. Marsman, G. I. Csonka, A. Ruzsinszky, P. Hao, Y.-S. Kim, G. Kresse, and J. P. Perdew, "Self-consistent meta-generalized gradient approximation within the projector-augmented-wave method," *Physical Review B*, vol. 84, no. 3, p. 035117, 2011.

[208] P. Vinet, J. Ferrante, J. Smith, and J. Rose, "A universal equation of state for solids," *Journal of Physics C: Solid State Physics*, vol. 19, no. 20, p. L467, 1986.

[209] P. Vinet, J. H. Rose, J. Ferrante, and J. R. Smith, "Universal features of the equation of state of solids," *Journal of Physics: Condensed Matter*, vol. 1, no. 11, p. 1941, 1989.

[210] H.-J. Liao, J.-G. Liu, L. Wang, and T. Xiang, "Differentiable programming tensor networks," *Physical Review X*, vol. 9, no. 3, p. 031041, 2019.

[211] J. Brownlee, "A gentle introduction to the rectified linear unit (relu)," *Machine learning mastery*, vol. 6, 2019.